
300 ppt Measurement of the Proton g -Factor

Dissertation

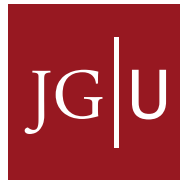
zur Erlangung des Grades

„Doktor der Naturwissenschaften“

am Fachbereich Physik, Mathematik und Informatik

der Johannes Gutenberg-Universität

in Mainz



Georg Schneider

geboren in Trier

Mainz, den 8. Dezember 2017

Datum der mündlichen Prüfung: 12. Juni 2018

Zusammenfassung

300 ppt Messung des g -Faktors des Protons

Im Rahmen dieser Arbeit wurde die Messung des Proton g -Faktors um mehr als eine Größenordnung verbessert, verglichen mit dem vorherigen Experiment. Um das magnetische Moment des Protons zu messen, wird ein isoliertes Proton in einer kryogenen Doppelfalle gespeichert. Die *Präzisionsfalle* dient der Hochpräzisionsmessung der freien Zyklotronfrequenz und der simultanen Anregung mit der Larmorfrequenz. Anschließend wird das Teilchen in die *Analysefalle* transportiert, um den Spinzustand zu bestimmen. Diese Messsequenz wird mehrere hundert Male wiederholt, um die Spin-Flip-Wahrscheinlichkeit als Funktion der eingestrahlteten Larmorfrequenz zu messen. Das magnetische Moment in Einheiten des Kernmagnetons ist dann gegeben durch das Verhältnis aus Larmorfrequenz und freier Zyklotronfrequenz. Um den Spinzustand des Protons zu bestimmen, wird der kontinuierliche Stern-Gerlach-Effekt in der Analysefalle angewandt. Dieser verwendet ein inhomogenes magnetisches Feld, um den Spinzustand nicht-destruktiv auszulesen. Diese Methode wurde zum ersten Mal mit großem Erfolg für Elektron/Positron $g-2$ Experimente von Dehmelt im Jahr 1986/1987 verwendet. Verglichen mit dem Elektron erfordert das Proton ein mehr als 10 000-fach empfindlicheres Experiment aufgrund der intrinsischen Kleinheit des magnetischen Moments.

Um die Limitationen der vorherigen Messung zu beseitigen, wurde die Apparatur und die experimentelle Routine signifikant modifiziert. Dies beinhaltet eine höhere magnetische Homogenität, eine höhere Magnetfeldstabilität mittels einer quasi-aktiven Magnetfeldabschirmung, eine optimierte Anregungsamplitude und neue supraleitende Nachweissysteme mit verbesserten kryogenen rauscharmen Verstärkern. All diese Verbesserungen führten zu einer 12 mal schmäleren Linienbreite und zu einer doppelt so hohen Datensammelrate.

Das endgültige Ergebnis mit einer Genauigkeit von 3×10^{-10} stellt die präziseste Messung eines Kernmoments dar. Ein direkter Vergleich mit dem magnetischen Moment des Antiprotons erlaubt einen verbesserten Test einer fundamentalen Symmetrie zwischen Materie und Antimaterie, der kombinierten CPT (Ladung, Parität, Zeit) Invarianz.

Ein weiterer Test der CPT-Symmetrie wurde durch die Messung des Ladungs-zu-Masse-Verhältnisses zwischen Proton und Antiproton mit einer Genauigkeit von 69×10^{-12} im Rahmen der BASE-Kollaboration am CERN mitentwickelt.

Summary

300 ppt Measurement of the Proton g -Factor

As a part of this work the measurement of the proton g factor was improved by more than one order of magnitude compared to the previous experiment. To measure the proton magnetic moment, a single isolated particle is stored in a cryogenic double Penning-trap system. The *precision trap* is used for the high-precision measurement of the particle's free cyclotron frequency and the simultaneous excitation with a Larmor drive. Subsequently, the particle is transported to the *analysis trap* where spin-transition spectroscopy is performed. This sequence is repeated several hundred times to measure the spin-flip probability as a function of the Larmor drive. The magnetic moment in units of the nuclear magneton is then obtained by the ratio of the Larmor frequency and the free cyclotron frequency. To detect the proton spin state the continuous Stern-Gerlach effect is applied in the analysis trap. Here, an inhomogeneous magnetic field to detect the spin state in a nondestructive way is used. The method was first introduced and applied with great success in electron/positron $g-2$ experiments by Dehmelt in 1986/1987. In comparison, its application to the proton system requires a more than 10 000-fold as sensitive apparatus due to the intrinsic weakness of the proton magnetic moment

To overcome the limitations of the previous measurement the apparatus and the experimental routines were significantly improved. This includes a higher magnetic homogeneity, a more stable magnetic field by means of quasi-active magnetic shielding, an optimized drive strength and new highly sensitive superconducting detection circuits with improved cryogenic ultra-low-noise amplifiers. These modifications led to a 12 times narrower linewidth and a two times higher data collection rate.

The final result with a fractional precision of 3×10^{-10} is the most precise measurement of any nuclear magnetic moment to date. A direct comparison to the antiproton magnetic moment allows for an improved direct test of a fundamental symmetry between ordinary matter and antimatter, the combined CPT (Charge, Parity, Time) invariance.

An additional CPT test was achieved by comparing the charge-to-mass ratio of proton and antiproton with a fractional precision of 69×10^{-12} as part of the BASE collaboration at CERN.

Contents

1	Introduction	1
2	Theoretical Basics	7
2.1	Ideal Penning trap	7
2.2	Cylindrical Penning trap	10
2.3	Determination of the spin magnetic moment	12
2.4	Electric and magnetic field imperfections	13
2.5	Detection principle	14
2.6	Sideband coupling	18
2.7	Electronic feedback control	20
2.8	Continuous Stern-Gerlach effect	20
2.9	Double trap scheme	22
2.10	Experimental setup	23
3	The Analysis Trap (AT)	27
3.1	Stability of the axial frequency	27
3.1.1	Theoretical description	27
3.1.2	Experimental optimization and characterization	30
3.2	Detection system temperature	33
3.3	Tuning ratio optimization	34
3.4	Spin-flip probability	36
4	The Precision Trap (PT)	39
4.1	Improved cyclotron detector	39
4.2	TR optimization	43
4.3	Temperature of the axial detection system	44
4.4	D4Tz characterization	45
4.5	Magnetic field contributions	46
4.6	Frequency fitting	50
4.6.1	Analytic model	50
4.6.2	Fit algorithm	51

4.6.3	Determination of the resonator frequency	53
4.7	Line shape of the g-factor resonance	54
5	First Steps in phase space	57
5.1	Phase method	57
5.1.1	Phase stability as function of S/N	58
5.1.2	Optimization of the averaging time	60
5.1.3	Fourier vs Laplace transform	62
5.1.4	Bleeding and zero padding	64
5.2	Experimental results	66
5.2.1	Setup	66
5.2.2	Excitation pulse optimization	67
5.2.3	Temperature and TR optimization	68
5.2.4	Application to a Larmor resonance	69
5.2.5	Single spin-flip resolution	70
6	Spin analysis	73
6.1	Spin analysis in the precision trap	73
6.2	Spin analysis in the analysis trap	76
6.2.1	Measurement principle	76
6.2.2	Threshold method	77
6.2.3	Bayesian method with random walk	79
7	The g-factor measurement	83
7.1	Measurement scheme	83
7.2	Data analysis	86
7.2.1	Statistical g-factor	86
7.2.2	Statistical crosschecks	90
7.3	Systematics	92
7.3.1	Systematic errors	92
7.3.2	Systematic crosschecks	96
7.3.3	Final result	100
7.4	Improved CPT Test in the baryonic sector	100
8	Antiproton-to-proton charge-to-mass ratio	103
8.1	Experimental setup	103
8.2	Results	105
9	Outlook	109
9.1	Laser cooling	109
9.1.1	Motivation	109

9.1.2	Working principle	110
9.1.3	Coupling trap design	111
9.1.4	Experimental setup	113
9.2	Additional improvements towards $< 300\text{ppt}$	114
10	Summary and conclusion	117
	Literature	125
A	Experimental values	127
A.1	Analysis trap	127
A.1.1	Overview	127
A.1.2	Axial resonator	127
A.2	Precision trap	128
A.2.1	Overview	128
A.2.2	Axial resonator	128
A.2.3	Cyclotron resonator	129
A.3	g-factor related measurement parameters	129
A.3.1	Precision trap	129
A.3.2	Analysis trap	129
A.3.3	Miscellaneous	130
B	Connection diagram	131

List of Figures

1.1	Various CPT Tests	2
1.2	History of proton/antiproton g-factor measurements	3
2.1	Ideal Penning trap and five electrode design	8
2.2	Particle eigenmotions and energy levels	9
2.3	Lumped circuit model of the detection system	15
2.4	Single and double dip spectrum	16
2.5	Cyclotron double dip detuning	19
2.6	Feedback scheme	20
2.7	Continuous Stern-Gerlach effect	21
2.8	Double trap scheme	22
2.9	Pressure and temperature stabilization	23
2.10	Experimental setup	24
2.11	Precision trap connection diagram	26
3.1	Spin-flip signal in the analysis trap and fidelity as function of energy	28
3.2	Allan deviation and stability of the axial frequency	29
3.3	Asymmetry compensation	30
3.4	Temperature determination of the detection system	34
3.5	TR optimization with tuning ratio	35
3.6	TR optimization with feedback	36
3.7	Spin-flip probability measurement	37
4.1	Cyclotron resonator setup	40
4.2	S/N and Q-value as function of coupling factor, cyclotron resonator spectra	41
4.3	Cyclotron detector temperature measurement	42
4.4	TR optimization with magnetron bursts	43
4.5	Axial temperature measurement	44
4.6	D4Tz measurement	45
4.7	B2 Optimization and B1 measurement	47
4.8	B2Tz measurement	48

4.9	Self-shielding coil tests	49
4.10	Cyclotron frequency stability between 2014 and 2017 experiment	50
4.11	Comparison between theoretical fit model and measurement spectra	51
4.12	Systematic shifts with fit algorithm and parameters	52
4.13	FFT background and resonator frequency precision	53
4.14	g -factor lineshape	54
5.1	Phase method principle	58
5.2	Phasespace and S/N calculation	59
5.3	Phase stability as function of S/N	60
5.4	S/N and phase stability dependence on averaging time	62
5.5	Phase stability with Fourier and Laplace analysis	63
5.6	S/N for Fourier and Laplace analysis	64
5.7	Phase optimization with zero padding	65
5.8	Experimental setup for the phase method	66
5.9	Excitation parameter space measured and simulated	67
5.10	Energy dependence of phase stability	68
5.11	Larmor resonance measurement with phase method	70
5.12	Single spin flips with phase method	71
6.1	Introduction to all symbolic expressions	74
6.2	Axial frequency distribution with spin flips	77
6.3	Axial series with spin states	78
6.4	Fidelity with threshold method for various parameters	79
6.5	Fidelity comparison of threshold and Bayes method	81
7.1	g -factor measurement scheme	84
7.2	Characterization of axial frequency fluctuations	86
7.3	Larmor drive heating effect	88
7.4	Frequency drifts in PT	89
7.5	g -factor resonance	90
7.6	Crosschecks for statistical result	91
7.7	Resonator frequency behavior	95
7.8	Resonator temperature during single and double dip and power splitting	97
7.9	External reference scheme of the experiment	98
7.10	Historic g -factor measurements	100
8.1	Experimental trap setup for the charge-to-mass ratio comparison	104
8.2	Experimental measurement scheme	105
8.3	Dominating shift by trap asymmetry	106

9.1	Concept of laser cooling	110
9.2	Coupling trap design	112
9.3	New trap layout for laser cooling. The electrical pinbase on the left contains electrical feedthroughs for DC, detection and excitation lines. The five traps are mounted in the center of the trap chamber. The new optical pinbase on the right guides two lasers into the chamber through sapphire windows.	114
B.1	Schematic connection diagram of the whole experiment	131

List of Tables

2.1	Theoretical trap parameters	12
7.1	g-factor parameter estimates based on likelihood analysis	90
7.2	Summary of systematic corrections	96
7.3	New constraints on SME coefficients	102
9.1	Trap parameters for laser setup	111

Chapter 1

Introduction

It is an old ideal to build a theoretical framework for the description of the world based on a fundamental underlying principle. Democritus, for example, around 400 B.C. introduced such a concept with an atomic theory in which all matter was composed of “uncuttable” objects – atoms. While this was a rather philosophical approach, modern physics has made tremendous advances in the development of a “theory of everything”. However, such a theory that provides a full explanation of all known physical phenomena in the universe has not yet been achieved.

Currently, the most complete model of modern physics is the Standard Model (SM) of particle physics, based on 12 fermions and their unified fundamental interactions. The first unification of fundamental forces was achieved in 1865 by Maxwell [1] when he united electricity and magnetism in a set of coupled equations. This enabled a new perspective of electromagnetic phenomena such as light. Later, in 1934, Fermi published his ideas [2] describing the theory of beta decay, and the concept of the weak interaction was born. It was not until the 1960s that Glashow, Salam and Weinberg unified the weak interaction with the electromagnetic force [3, 4, 5]. For the development of the electroweak unification they received the Noble Prize in 1979. The Standard Model of particle physics incorporates both the electroweak interaction and the strong interaction, the third fundamental force which is responsible for holding nuclei together.

The SM is capable of explaining a tremendous amount of experimental results and predicted many new phenomena, such as the top quark [6, 7] and the Higgs Boson [8, 9]. Another impressive example is the Z-Boson, predicted by the electroweak theory in the 1960s with first experimental indications in 1973 [10, 11], and finally discovered in 1983 [12]. However, even with these remarkable successes, the SM is known to be incomplete. For example, gravity, despite being one of the four fundamental forces, is not included in the SM. Another example is the yet to be understood composition of the universe. According to the analysis of data from the PLANCK space telescope, which provided high resolution scans of the cosmic microwave background, about 95% of the universe is made of dark matter and dark energy and only 5% of its energy content is described by the SM [13].

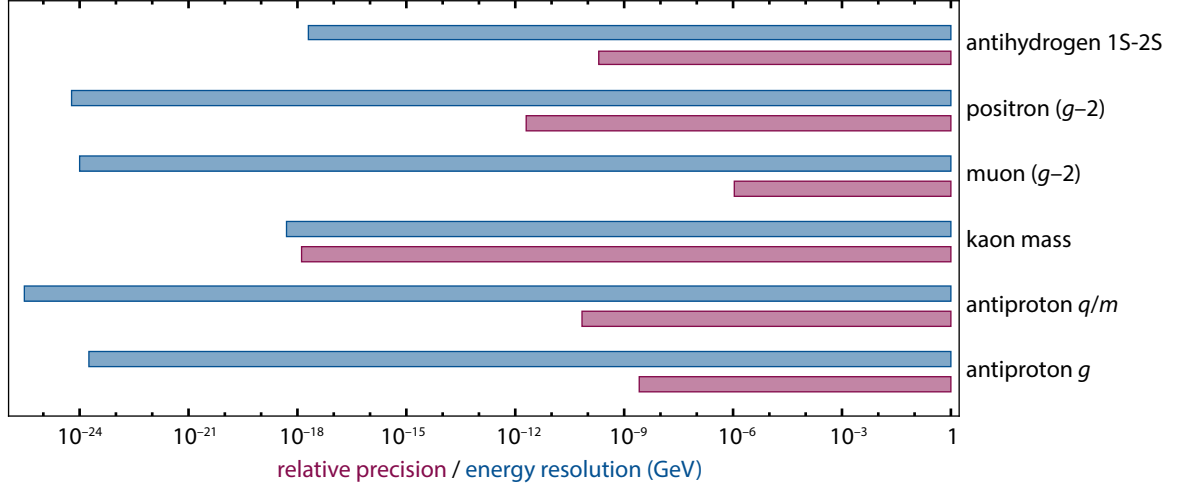


Fig. 1.1: Selection of several CPT tests in matter-antimatter systems. The red bars show the relative precision of the experiments, while the blue bars shows the energy resolution $\Delta E = h\Delta\nu$ which is typically used in the Standard Model Extension.

Yet even these 5% are not fully understood. One of the prominent questions of modern physics is the striking imbalance between matter and antimatter. In the Standard Model, particles and their antimatter counterparts, apart from signs, have identical properties and should have been created in equal amounts during the Big Bang. This is a consequence of a fundamental symmetry of the Standard Model – CPT invariance [14, 15]. It implies that the relativistic quantum field theories of the SM are invariant under the combined transformation of charge (C), parity (P) and time (T). This is in strong contradiction to the matter dominated universe. If matter and antimatter should behave symmetrically, what caused the apparent matter abundance?

Sakharov, in 1967, introduced three necessary conditions [16] that could cause an imbalance between matter and antimatter: (1) a violation of the baryon number, (2) C and CP violation, and (3) a deviation from thermal equilibrium. All of these conditions are compatible with the current SM. However, the experimentally observed asymmetry [17]

$$\eta_{\text{exp}} = \frac{N_{\text{B}} - N_{\bar{\text{B}}}}{N_{\gamma}} \sim 10^{-10} , \quad (1.1)$$

with today's baryon number N_{B} and antibaryon number $N_{\bar{\text{B}}}$, cannot solely be explained by the SM since the asymmetry produced by known SM-CP violation is far too weak $\eta_{\text{SM}} \sim 10^{-20} \ll \eta_{\text{exp}}$ [18]. Nowadays, many experiments have been inspired by this mystery and are trying to pin down the source of the asymmetry, for example, by testing CPT symmetry. Any discovered violation of CPT would indicate physics beyond the SM and could provide mechanisms which contribute to our symmetry understanding of the imbalance between matter and antimatter [19].

A variety of experiments have tested CPT symmetry [20] in different sectors, because neither the physical system nor the level of precision is known where CPT might be broken. The Standard Model Extension (SME) [21], a framework that compares different CPT tests, provides a quantita-

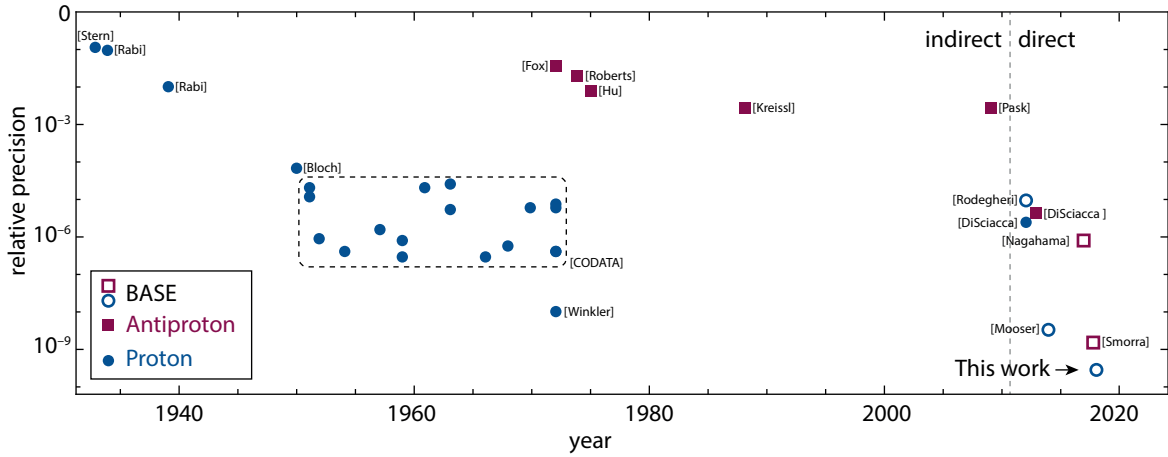


Fig. 1.2: History of several g -factor measurements of proton (blue dots) and antiproton (red squares). The measurements in the box are listed in the CODATA reports 1969 [22] and 1973 [23]. The results made by the BASE collaboration are marked with a blue circle or red rectangle. All recent measurements after the vertical dashed line are direct measurements in Penning traps.

tive measure that defines the sensitivity of an experiment on an absolute energy scale. It couples the Standard Model with General Relativity and incorporates all possible operators for Lorentz and CPT violation [20] in an effective field theory. The Lorentz and CPT violating operators scale with coefficients which are constrained by experimental results.

The results of several matter-antimatter comparisons are shown in figure 1.1 together with the energy resolution in GeV, the conventional unit in the SME that characterizes the sensitivity. For example, a recent study with antihydrogen by the ALPHA collaboration had a sensitivity of 2×10^{-18} GeV [24] while another measurement in the neutral kaon system yielded a sensitivity of 5×10^{-19} GeV [25, 18] by comparing the decay channels of K^0 and \bar{K}^0 . Other measurements in the leptonic sector have set bounds through a comparison of the electron/positron g factors [26, 27] and the muon g factors [28]. This work, produced in the framework of the BASE collaboration [29], contributes to these CPT symmetry tests by comparing the fundamental properties of the proton and the antiproton at low energies and with high precision. The BASE collaboration operates two dedicated experiments, one in Mainz, Germany and the other at CERN, Geneva, Switzerland to determine the charge-to-mass ratios $(q/m)_p/(q/m)_{\bar{p}}$ and the magnetic moment

$$\boldsymbol{\mu} = g \frac{q}{2m_p} \mathbf{S} , \quad (1.2)$$

which is connected to the spin \mathbf{S} of the proton/antiproton by the dimensionless g factor.

The history of proton magnetic moment measurements includes several groundbreaking discoveries and developments of new techniques that had great influence on modern physics. The first pioneering measurement of the proton magnetic moment was conducted by O. Stern in 1933 [30] with a value of $\mu_p = 2.5(3) \mu_N$, in units of the nuclear magneton $\mu_N = q\hbar/(2m_p)$. The magnetic moment was determined by measuring the splitting of a molecular hydrogen beam in an inhomogeneous magnetic field.

geneous magnetic field. In 1943 Stern was rewarded the Noble Prize for the historic discovery that the experimental value μ_p/μ_N differed from the expected value of 1 predicted by the Dirac theory [31]. This was the first indication that the proton is not an elementary particle and has some sort of sub-structure. Another measurement was conducted by Rabi [32] with a value of 3.25(33) that, while inconsistent with the measurement of Stern, confirmed the approximately three times larger than expected magnetic moment. After laying the ground for the nuclear magnetic resonance (NMR) method in 1938 [33] Rabi's group used this famous scheme for an improved measurement of $\mu_p = 2.785(30)\mu_N$ [34]. Bloch, the winner of the Noble Prize in 1952, further developed on these ideas [35] and achieved a precision of 70 ppm by measuring the ratio between the nuclear resonance frequency and the orbital rotation frequency [36] in a proton beam. Since then, many measurements have been conducted [22, 23] culminating in the measurement of Winkler [37] at a precision of 10 ppb by measuring the ground-state hyperfine splitting of atomic hydrogen with a MASER. In the same year, the magnetic moment of the antiproton was measured for the first time by Fox [38], and later improved by Roberts [39], Hu [40] and Kreissl [41] with measurements of the fine-structure splitting in antiprotonic atoms with the antiproton acting as a "heavy electron". The most recent indirect measurement of the magnetic moment was performed by Pask [42] who studied the hyperfine splitting in antiprotonic helium, however, still with a precision of 10^{-3} .

Dramatic advances were achieved in 2013 when for the first time a direct measurement of $\mu_{\bar{p}}$ in a Penning trap at the level of 10^{-6} was achieved [43], based on the methods demonstrated in the proton case [44, 45]. These experiments perform a simultaneous measurement of the free cyclotron frequency ω_c and the Larmor frequency ω_L , which yield the magnetic moment in units of the nuclear magneton

$$\left| \frac{\mu_{p,\bar{p}}}{\mu_N} \right| \equiv \frac{g_{p,\bar{p}}}{2} = \frac{\omega_L}{\omega_c} . \quad (1.3)$$

An improved measurement of the antiproton g factor was achieved in 2017 by Nagahama [46]. However, this measurement, as well as the previous direct measurements, were limited to the 10^{-6} level due to linewidth broadening in the inhomogeneous magnetic field used for the detection of the spin state. This fundamental limit was overcome in case of the proton by employing the double-trap method [47] in 2014 [48] which enabled a factor of 3 more precise measurement of μ_p than the MASER measurement. The double-trap method separates the traps for the spin-flip detection and for the high frequency determination, which allows a much higher frequency resolution. This paved the way for a drastically improved measurement, by a factor of 350, of the antiproton g factor [49] which used a novel two particle three-trap scheme.

This thesis discusses the 11-fold improved measurement, recently published in *Science* [50], of the proton magnetic moment with a precision of 0.3 parts per billion which constitutes the most precise measurement of any nuclear moment to date. The techniques developed can be directly applied to the antiproton and other nuclear moments. Moreover, a direct comparison between proton and antiproton magnetic moments provides a stringent test of the CPT invariance in the baryonic sector.

The thesis is organized as follows: Chapter 2 introduces the theoretical concepts required for the final g -factor measurement, such as the measurement principle and the detection techniques. Chap-

ters 3 and 4 discuss properties and characterizations of the two Penning traps used in the experiment. Chapter 5 introduces the phase method used for the frequency determination and experimental results as well as experimental implications are discussed thoroughly. Chapter 6 introduces different algorithms which are used to determine the spin state of the proton with the focus on a Bayesian approach. Chapter 7 discusses the g factor measurement of the proton and the statistical analysis along with the systematic corrections. Chapter 8 covers the charge-to-mass ratio measurement for proton/antiproton which was conducted by the BASE collaboration at CERN. Chapter 9 discusses an upgrade of the current experiment and future techniques to improve the precision even further.

Chapter 2

Theoretical Basics

2.1 Ideal Penning trap

The longtime storage of a single particle under stable conditions is an ideal environment to perform high-precision measurements and can be achieved by the combination of a static magnetic field and an electrostatic quadrupole potential. The magnetic field along the *axial* direction z forces the particle on an orbit in the xy -plane due to the Lorentz force. To prevent the particle from moving along the z -axis the superimposed quadrupole with a repulsive force in z and an attractive force in the xy -plane is used, compare figure 2.1 A. Such a configuration is called a *Penning trap* [51] and was first used in its present form by H. G. Dehmelt who named it after F. M. Penning.

Starting with the classical view a particle with charge q and mass m in a magnetic field moves on a circular orbit where the Lorentz force and the centrifugal force equal each other. The associated *cyclotron frequency*¹

$$\omega_c = \frac{q}{m} B \quad (2.1)$$

scales with the strength of the magnetic field $B = |\mathbf{B}| = |B_z \hat{e}_z|$. For the complete description of the particle motion the quadrupole potential

$$\phi = V_r C_2 \left(z^2 - \frac{\rho^2}{2} \right) \quad \text{with} \quad \rho = \sqrt{x^2 + y^2} \quad (2.2)$$

must be taken into account as well, which is proportional to the ring voltage V_r as defined in figure 2.1 B and a trap specific parameter $\sqrt{C_2}$ with the dimension of an inverse length. Based on the Lorentz force $\mathbf{F} = m \ddot{\mathbf{r}} = q(\mathbf{E} + \mathbf{v} \times \mathbf{B})$ with the electric field $\mathbf{E} = -\text{grad } \phi$ this leads to the equations

¹Throughout this thesis v and $\omega = 2\pi v$ will both be referred to as frequency

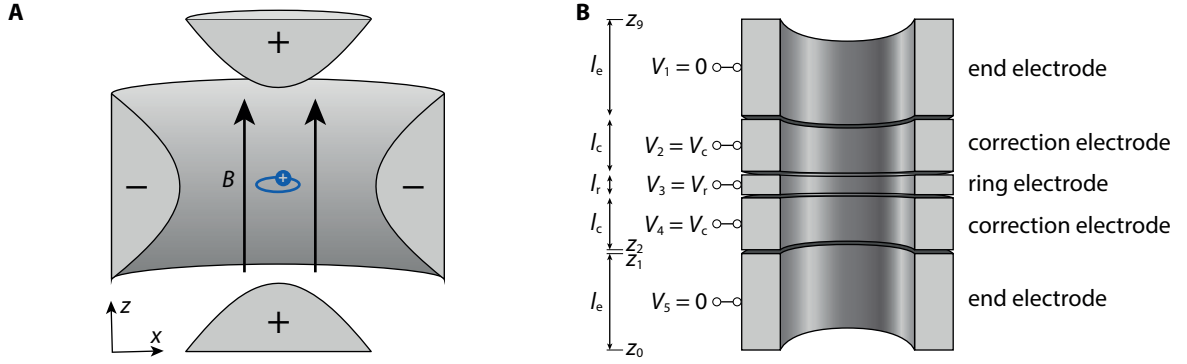


Fig. 2.1: (A) The superposition of a magnetic field in axial direction z and an electrostatic quadrupole potential allows stable storage of particles and is called a Penning trap. (B) Experimental realization of a cylindrical Penning trap. By choosing appropriate voltages V_i and electrode lengths l_i a quadrupole potential can be approximated in the center of the trap.

of motion [51]

$$\begin{pmatrix} \ddot{x} - \omega_c \dot{y} - \frac{\omega_z^2}{2} x \\ \ddot{y} + \omega_c \dot{x} - \frac{\omega_z^2}{2} y \\ \ddot{z} + \omega_z^2 z \end{pmatrix} = 0 . \quad (2.3)$$

The axial motion, along the magnetic field lines, is a simple harmonic oscillator with the *axial frequency*

$$\nu_z = \frac{1}{2\pi} \sqrt{\frac{2qC_2V_r}{m}} , \quad (2.4)$$

and is typically tuned by adjusting the ring voltage V_r . The eigenmodes in the radial plane form a coupled set of harmonic oscillators with frequencies

$$\nu_{\pm} = \frac{1}{2} \left(\nu_c \pm \sqrt{\nu_c^2 - 2\nu_z^2} \right) , \quad (2.5)$$

the *modified cyclotron frequency* ω_+ and the *magnetron frequency* ω_- . Stable particle storage requires $\nu_c^2 - 2\nu_z^2 > 0 \Leftrightarrow V_r < \frac{q}{4mC_2} B^2$ which can be used to deliberately remove a particle species by increasing V_r beyond the critical level. This is especially useful since protons have the lowest q/m and are the last species to become unstable.

The combined particle motion with all three eigenmotions is shown in figure 2.2 A. Typical numbers for a Penning trap as operated by the proton experiment in Mainz are $\nu_+ \approx 28.96$ MHz, $\nu_z \approx 640$ kHz and $\nu_- \approx 6930$ Hz with the distinct hierarchy $\nu_+ \gg \nu_z \gg \nu_-$. For further experimental numbers refer to appendix A.3.1. The frequencies are related to each other by the important invariance theorem [51]

$$\omega_c^2 = \omega_+^2 + \omega_z^2 + \omega_-^2 \quad (2.6)$$

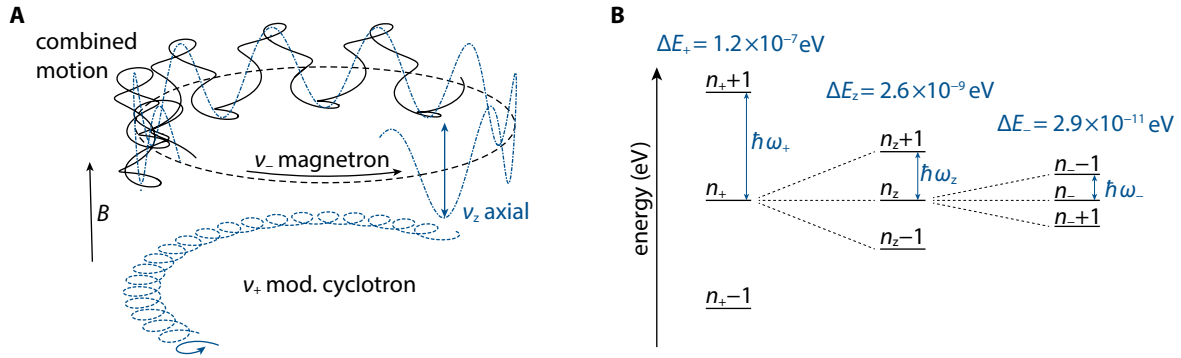


Fig. 2.2: (A) The combined particle motion is composed of the individual eigenmotions. The axial oscillation is along the magnetic field lines and the magnetron and modified cyclotron motion in the radial plane. (B) Each of the eigenmotions is associated with a principal quantum number n_z and n_{\pm} . The degenerate energy levels are not shown to scale and sorted by the frequency hierarchy $\nu_+ \gg \nu_z \gg \nu_-$. The metastable magnetron motion lowers the total energy with increasing principal quantum number.

that links the three physical eigenmotions of the particle in the trap to the free cyclotron frequency. This equation holds in the presence of trap imperfections or misalignment [52]. For example, a tilted trap with respect to the magnetic field lines leads to a lower axial frequency and a higher magnetron frequency. However, these effects cancel in the invariance theorem leaving the free cyclotron frequency invariant. Additional relations are

$$\omega_- = \frac{\omega_z^2}{2\omega_+} \quad \text{and} \quad \omega_c = \omega_+ + \omega_- \quad (2.7)$$

which are, however, only valid for an ideal trap. The first equation for the magnetron frequency, for example, can be a well suited estimate depending on the desired level of precision. The whole system of three harmonic oscillators can be expressed by the Hamiltonian

$$H = \hbar\omega_+ \left(n_+ + \frac{1}{2} \right) + \hbar\omega_z \left(n_z + \frac{1}{2} \right) - \hbar\omega_- \left(n_- + \frac{1}{2} \right) \quad (2.8)$$

and is illustrated in figure 2.2 B. The magnetron mode has the unique property that an increase in the principal quantum number n_- leads to a decrease of the total energy. The magnetron motion is metastable since removing energy

$$E_- = \frac{1}{2}m\omega_-^2 r_-^2 - \frac{1}{4}m\omega_z^2 r_-^2 \approx -\frac{1}{4}m\omega_z^2 r_-^2 \quad (2.9)$$

increases the magnetron radius r_- , which eventually leads to particle loss when the particle hits the trap surface. Assuming that the only loss mechanism is radiation damping a decay time can be calculated to [51]

$$\tau_- = \frac{1}{\gamma_-} = \left(\frac{1}{4\pi\epsilon_0} \frac{4q^2}{3mc^3} \frac{\omega_-^3}{\omega_+ - \omega_-} \right)^{-1} \approx 3 \times 10^{20} \text{ s} = 2 \times 10^{15} \text{ y} \quad (2.10)$$

and has no experimental relevance. The relationship (2.9) shows that the total magnetron energy E_- is almost completely potential energy. In contrast, the total modified cyclotron energy is mainly kinetic

$$E_+ = \frac{1}{2}m\omega_+^2 r_+^2 - \frac{1}{4}m\omega_z^2 r_+^2 \approx \frac{1}{2}m\omega_+^2 r_+^2 . \quad (2.11)$$

Finally, the axial kinetic and potential energy can be expressed by the total energy

$$E_z = \frac{1}{2}\omega_z^2 r_z^2 \quad (2.12)$$

with r_z the peak value of the axial coordinate. The average total mode energies of the particle can be related to effective temperatures by

$$\langle E_+ \rangle = k_B T_+ \quad \langle E_z \rangle = k_B T_z \quad \langle E_- \rangle = k_B T_- < 0 \quad (2.13)$$

with the magnetron energy being negative with respect to the perfectly centered particle. While the temperature is only defined for an ensemble or a distribution of energies the term *cooling* will be used in this thesis to indicate a reduction of the radius of a single particle.

2.2 Cylindrical Penning trap

A cylindrical five-pole Penning trap [53] as shown in figure 2.1 B has the advantage that systems of several traps can be easily connected with additional cylindrical transport electrodes. Furthermore, the cylindrical design allows a very precise manufacturing with tolerances below 10 μm . A quadrupole potential in the trap is realized by an appropriate choice of the trap lengths l_i and the electrode voltages V_i . For a given radius a the central *ring electrode* voltage V_r , the voltage on the adjacent *correction electrodes* V_c and their respective lengths l_r and l_c are considered as free parameters. The length of the outermost electrodes, the *end electrode* or *endcaps*, are set to $l_e \gg a$ and the potentials are assumed to be grounded. The electrodes are separated by a small gap with length d .

The solution for a potential inside a cylinder is a well known theoretical problem [54] described by the Laplace equation in free space

$$\Delta\Phi = 0 \quad \Rightarrow \quad \frac{1}{\rho} \frac{\partial}{\partial \rho} \left(\rho \frac{\partial \Phi}{\partial \rho} \right) + \frac{1}{\rho^2} \frac{\partial^2 \Phi}{\partial \varphi^2} + \frac{\partial^2 \Phi}{\partial z^2} = 0 , \quad (2.14)$$

where cylindrical coordinates were chosen due to the symmetry of the trap. This second-order partial differential equation can be solved with the separation ansatz

$$\Phi(\rho, z) = \sum_{n=1}^{\infty} I_0(k_n \rho) A_n \sin(k_n z), \quad k_n = \frac{n\pi}{\Lambda}, \quad n \in \mathbb{N}, \quad (2.15)$$

with the Bessel-functions of the first kind I_0 . $\Lambda = z_9 - z_0$ denotes the total length of all five electrodes where the z_i are axial coordinates as defined in 2.1 B. After integrating $\int_0^\Lambda \Phi(a, z) dz$ and solving for

the coefficients A_n the solution reads

$$\Phi = \sum_{n=1}^{\infty} \left(\frac{V_1 \cos(k_n z_0) - V_5 \cos(k_n \Lambda)}{k_n} + \sum_{i=1}^4 \frac{V_{i+1} - V_i}{k_n^2 d} (\sin(k_n z_{2i}) - \sin(k_n z_{2i-1})) \right) \times \frac{2}{\Lambda} \frac{I_0(k_n \rho)}{I_0(k_n a)} \sin \left(k_n \left(z + \frac{\Lambda}{2} \right) \right) . \quad (2.16)$$

It is important to note that for the integration on the boundaries at $r = a$ the potential between two neighboring electrodes is linearly interpolated. In addition, the solution was shifted by half the trap length, $\Lambda/2$, to set the origin $z = 0$ to the center of the ring electrode.

Next, the potential on the z -axis for $\rho = 0$ is expanded in a Taylor series based at the origin

$$\Phi(0, z) = V_3 \sum_{j=0}^n C_j z^j \quad (2.17)$$

with the coefficients

$$C_j = \sum_{n=1}^{\infty} \left[\frac{V_1 \cos(k_n z_0) - V_5 \cos(k_n \Lambda)}{k_n} + \sum_{i=1}^4 \frac{V_{i+1} - V_i}{k_n^2 d} (\sin(k_n z_{2i}) - \sin(k_n z_{2i-1})) \right] \times \frac{2}{j! \Lambda V_3} \left(\frac{n\pi}{\Lambda} \right)^j \frac{1}{I_0(k_n a)} \sin \left(\frac{\pi}{2} (n + j) \right) . \quad (2.18)$$

These coefficients with the assignment $V_1 = V_5 = 0$, $V_2 = V_4 = V_c$, $V_3 = V_r$ and $l_2 = l_4 = l_c$, $l_3 = l_r$ fully describe the on-axis potential of a five pole trap. Odd coefficients in an ideal trap are equal to zero due to the mirror symmetry with respect to the ring electrode. Furthermore, a comparison with equation (2.2) shows that in an ideal Penning trap all coefficients $j > 2$ vanish with $C_2 \neq 0$.

During the experiment the axial frequency $\omega_z \sim \sqrt{V_r}$ of the particle is kept constant usually determined by the resonance frequency of the detection system. Thus, the ring voltage V_r is set and the correction voltage V_c can be expressed by the *tuning ratio*

$$TR = \frac{V_c}{V_r} . \quad (2.19)$$

Since the ring voltage is fixed the tuning ratio is adjusted by changing the correction voltages. The trap radius is typically constrained by the detection system performance. A better detection system allows for a larger radius which is preferred because larger radii lead to smaller systematic frequency shifts in the presence of machining errors. The discussion leaves only three free parameters, l_r , l_c and TR , to optimize the two important trap properties *compensation* and *orthogonality*.

A well compensated trap is designed such that the coefficients $C_4 = 0$ and $C_6 = 0$ vanish simultaneously for a specific ideal TR and a quasi-ideal quadrupole potential is realized. If higher orders, such as C_8 or C_{10} , should also vanish a seven pole trap with two additional free parameters is required.

In an orthogonal trap the axial frequency is not a function of TR which makes a systematic TR scan in practice much more convenient. Each C_j coefficient can be expanded by $C_j = E_j + D_j TR$ with a constant term and one that is proportional to the tuning ratio. An orthogonal trap is designed such

(mm)	PT	AT		PT	AT
a	3.5	1.8	TR_{id}	0.8809	0.8804
l_r	0.9877	0.4402	C_2 (m ⁻²)	30 580	115 360
l_c	2.7152	1.3309	D_4 (m ⁻⁴)	3.5×10^9	4.98×10^{10}
l_e	7.0000	4.4780	ν_c (Hz)	28.97×10^6	17.98×10^6
D_c	7.9	4.2	ν_+ (Hz)	28.96×10^6	17.97×10^6
D_e	19.7	9.7	ν_z (Hz)	633 640	740 240
D_{c+e}	5.6	2.9	ν_- (Hz)	6 933	15 279

Table 2.1: Theoretical parameters of the precision and the analysis trap. D_c is the axial effective electrode distance for the correction electrode, 'e' for the endcap and 'c+e' for a combined pick-up.

that $D_2 = 0$

$$\omega_z \sim \sqrt{C_2} = \sqrt{E_2 + D_2 TR} \Big|_{D_2=0} = \sqrt{E_2} = \text{const} , \quad (2.20)$$

and the axial frequency is not a function of TR .

Five pole traps are used in a large variety of experiments [55, 56]. The demand for higher precisions over the years has drawn the attention to seven pole traps due to their superior compensation. Recently, the first seven pole trap has been successfully commissioned [57].

An important property related to the cylindrical trap design is the *effective electrode distance* [58] which describes how well a particle signal can be "picked up" by e.g. a single correction electrode or an endcap. For the detection of the axial signal on a correction electrode the effective electrode distance is given by

$$D_z = \frac{2\Lambda}{8} \left(\sum_{n=1}^{\infty} \frac{\sin(k_n l_c) \cdot \sin(k_n (l_c + l_r + 2d))}{I_0(2k_n a)} \right)^{-1} \quad \text{with} \quad k_n = \frac{n\pi}{\Lambda} . \quad (2.21)$$

The factor 2 in the front is due to the pick-up on only one correction electrode. If both correction electrodes are used for pick-up D_z reduces by a factor of 2. This expression can of course also be used to calculate D_z for an endcap by setting the length of the ring electrode to $l_r \rightarrow 2l_c + l_r + 2d$ and $l_c \rightarrow l_e$. In the case of the detection of a radial signal the pick-up is achieved by a segmented electrode. The effective electrode distance for a segmented correction electrode [58] is

$$D_+ = \frac{\pi\Lambda}{8} \left(\sum_{n=1}^{\infty} \frac{\cos\left(\frac{k_{2n-1}}{2}(l_c + l_r)\right) \cdot \sin\left(\frac{k_{2n-1}}{2}l_c\right)}{I_1(k_{2n-1} a)} \right)^{-1} \quad \text{with} \quad k_{2n-1} = \frac{(2n-1)\pi}{\Lambda} . \quad (2.22)$$

A summary of theoretical trap values for the Mainz trap setup is found in table 2.1.

2.3 Determination of the spin magnetic moment

The previous sections introduced the particle dynamics of a spinless particle in a Penning trap. In case of the proton the spin and the associated magnetic moment must be considered. The spin and

magnetic moment are related by the dimensionless g -factor

$$\boldsymbol{\mu} = g \frac{q}{2m} \mathbf{S} \quad \Rightarrow \quad \mu = \frac{g}{2} \mu_{\text{N}} \quad (2.23)$$

with the nuclear magneton $\mu_{\text{N}} = \frac{q}{2m} \hbar$ and m the proton mass. In a Penning trap the magnetic moment couples to the external magnetic field and spin up and spin down give rise to an energy level splitting

$$\Delta E = g \frac{q \hbar}{2m} B = \hbar \omega_{\text{L}} \quad , \quad (2.24)$$

where ω_{L} is the *Larmor frequency*, the spin precession frequency in a given magnetic field. In order to determine g a measurement of the Larmor frequency ω_{L} and the magnetic field B suffices. For a known charge-to-mass ratio the measurement of the free cyclotron frequency ω_{c} is equivalent to a measurement of B and the g factor can be expressed as

$$g = 2 \frac{\omega_{\text{L}}}{\omega_{\text{c}}} \quad . \quad (2.25)$$

Frequencies can be measured very precisely and are thus an elegant tool to determine the magnetic moment. The free cyclotron frequency is obtained from the three eigenfrequencies and the invariance theorem while the Larmor frequency poses a much larger challenge and requires the implementation of the continuous Stern-Gerlach effect discussed in section 2.8.

2.4 Electric and magnetic field imperfections

The on-axis electric potential of a cylindrical Penning trap is described by the coefficients C_j and non-vanishing higher order terms characterize trap imperfections. Odd terms C_{2j+1} are suppressed due to the symmetry of the trap but can arise in the presence of small offset potentials on individual electrodes which break the symmetry. In practice, once identified, small offset potentials can be easily compensated by applying offset voltages to the correct electrodes.

Even terms C_{2j+1} for $j \geq 4$ lead to systematic frequency shifts on all particle eigenmotions as a function of particle energy. The equation of motion of the axial eigenmotion becomes a Duffing equation [59]

$$\ddot{z} = -\frac{q}{m} \partial_z \left(V_{\text{r}} \sum_{j=1}^{\infty} C_{2j} z^{2j} \right) = -\frac{2qC_2 V_{\text{r}}}{m} \left(z + \frac{2C_4}{C_2} z^3 + \frac{3C_6}{C_2} z^5 + \mathcal{O}(C_8) \right) \quad (2.26)$$

in the presence of anharmonicities, which become more pronounced for larger oscillation amplitudes. Besides the electrostatic field properties also magnetic field imperfections lead to shifts on the frequencies. The field is expanded similarly to the electrostatic case along the z -axis $B(z) = B_0 + B_1 z + B_2 z^2 + \mathcal{O}(z^3)$

The derivation of frequency shifts in the presence of magnetic and electric imperfections is technical and can, for example, be found in [51, 60], which use, however, a slightly different definition of

the potential. The conversion is given by

$$C_j = \frac{C_j}{2d^j} \quad (2.27)$$

with $C_2 \equiv 1$. This defines the geometrical parameter d often used in literature for hyperbolic traps. The relative frequency shifts under the typical experimental condition $\omega_- \ll \omega_z \ll \omega_+$ are then

$$\begin{pmatrix} \Delta\omega_+/\omega_+ \\ \Delta\omega_z/\omega_z \\ \Delta\omega_-/\omega_- \\ \Delta\omega_L/\omega_L \end{pmatrix} = (\mathcal{M}_{C4} + \mathcal{M}_{B2}) \begin{pmatrix} E_+ \\ E_z \\ E_- \end{pmatrix} + \mathcal{M}_{C6} \begin{pmatrix} E_+^2 \\ E_z^2 \\ E_-^2 \\ E_+E_z \\ E_+E_- \\ E_zE_- \end{pmatrix} + \mathcal{O}(C_8, B_4) \quad (2.28)$$

with the corresponding matrices

$$\mathcal{M}_{C4} = \frac{1}{qV_0} \frac{C_4}{C_2^2} \begin{pmatrix} \frac{3}{4}\Omega^4 & -\frac{3}{2}\Omega^2 & -3\Omega^2 \\ -\frac{3}{2}\Omega^2 & \frac{3}{4} & 3 \\ -3\Omega^2 & 3 & 3 \\ 0 & 0 & 0 \end{pmatrix} \quad \mathcal{M}_{B2} = \frac{1}{m\omega_z^2} \frac{B_2}{B_0} \begin{pmatrix} -\Omega^2 & 1 & 2 \\ 1 & 0 & -1 \\ 2 & -1 & -2 \\ -\Omega^2 & 1 & 2 \end{pmatrix} \quad (2.29)$$

$$\mathcal{M}_{C6} = \frac{1}{q^2V_0^2} \frac{C_6}{C_2^3} \begin{pmatrix} -\frac{15}{16}\Omega^6 & -\frac{45}{16}\Omega^2 & -\frac{45}{4}\Omega^2 & \frac{45}{8}\Omega^4 & \frac{45}{4}\Omega^4 & -\frac{45}{2}\Omega^2 \\ \frac{45}{16}\Omega^4 & \frac{15}{16} & \frac{45}{4} & -\frac{45}{8}\Omega^2 & -\frac{45}{2}\Omega^2 & \frac{45}{4} \\ \frac{45}{8}\Omega^4 & \frac{45}{8} & \frac{15}{2} & -\frac{45}{2}\Omega^2 & -\frac{45}{2}\Omega^2 & \frac{45}{2} \\ 0 & 0 & 0 & 0 & 0 & 0 \end{pmatrix}, \quad (2.30)$$

where $\Omega = \omega_z/\omega_+$ is introduced for simplicity and the magneton energy is assumed to be negative $E_- < 0$.

It is worth highlighting that electrostatic imperfections only affect the three frequencies ω_+ , ω_z and ω_- of the particle and not the Larmor frequency. This is particularly important for a g -factor measurement as the effect does not cancel in the ratio between cyclotron and Larmor frequency and leads to a systematic shift on g . \mathcal{M}_{B2} shows, that the modified cyclotron frequency ω_+ , which dominates the determination of ω_c , and the Larmor frequency ω_L have the same relative shifts. Therefore, the shift due to B_2 is strongly suppressed for the g -factor determination, discussed in more detail in chapter 7.

2.5 Detection principle

To determine the free cyclotron frequency ν_c via the invariance theorem the precise measurement of the proton's three eigenfrequencies is required. A technique to non-destructively detect the particle's eigenfrequencies was first introduced in 1975 by Wineland and Dehmelt [61]. Any particle stored in Penning trap induces tiny image currents on the trap electrodes due to their motion. The induced current for the axial motion

$$I = \frac{q}{D_z} \dot{z} \quad (2.31)$$

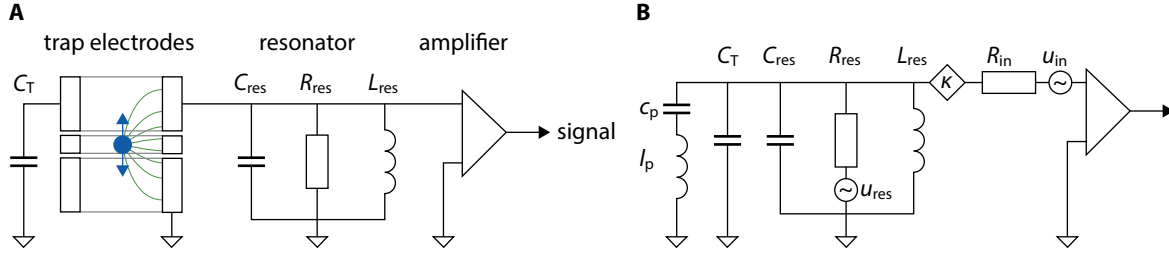


Fig. 2.3: (A) The particle in a Penning trap induces small image currents on the trap electrodes which are detected by connecting a tuned resonant circuit. The voltage signal is then amplified. A Fast Fourier Transformation of the signal allows the measurement of the proton's eigenmotions. (B) The particle is represented with its equivalent circuit diagram – a series resonance circuit. Two noise sources are added to account for the Johnson-Nyquist noise of the resonator and the input noise of the amplifier due to the input resistance R_{in} . κ describes the decoupling of the amplifier to the resonator as it is typically used in the experiment.

depends on the charge q , and the velocity \dot{z} in axial direction. D_z is the axial effective electrode distance, a geometrical measure to describe the strength of the particle coupling to an electrode, compare equation (2.21). For typical experimental parameters the current is in the order of 10^{-15} A and a large impedance is required to obtain a measurable voltage signal. However, even measuring the voltage drop across an infinitely large resistor would not be sufficient to get a sufficient signal

$$U_{\text{meas}} = \lim_{R \rightarrow \infty} \left| I \left(\frac{1}{R} + i\omega_z C_T \right)^{-1} \right| \approx 10 \text{ pV} \quad (2.32)$$

due to the parasitic trap capacitance C_T in parallel which usually is in the order of 10 pF. Instead of a large resistor an inductor L_{res} is connected to the trap as shown in figure 2.3 A. Inductor and trap capacitance form a resonant tuned circuit with resonance frequency

$$\omega_{\text{res}} = \frac{1}{\sqrt{L_{\text{res}}(C_T + C_{\text{res}})}} \quad (2.33)$$

C_{res} describes the self capacitance of the connected inductor, which cannot be neglected in a real setup. The total impedance of this parallel resonance circuit, referred to as *detector* or *resonator*, is

$$Z_{\text{res}}(\omega) = \frac{1}{R_{\text{res}}} + \frac{1}{i\omega L_{\text{res}}} + i\omega(C_{\text{res}} + C_T) \quad (2.34)$$

where R_{res} is a dissipative component that accounts for losses in the circuit. At its resonance frequency ω_{res} the capacitive component is compensated by the inductance and the total impedance yields $\lim_{\omega \rightarrow \omega_{\text{res}}} Z_{\text{res}}(\omega) = R_{\text{res}}$. Thus, a resonator with sufficiently high parallel resistance R_{res} , equivalent to small losses in the circuit, is suitable to achieve a measurable voltage drop and detect the tiny image currents. To describe the interaction of the particle with the previously introduced parallel resonance circuit the particle's equation of motion as a damped harmonic oscillator must be considered, following the arguments in [61, 62]

$$\ddot{z}(t) + \gamma \dot{z}(t) + \omega_z^2 z(t) = \frac{F_e}{m} \quad (2.35)$$

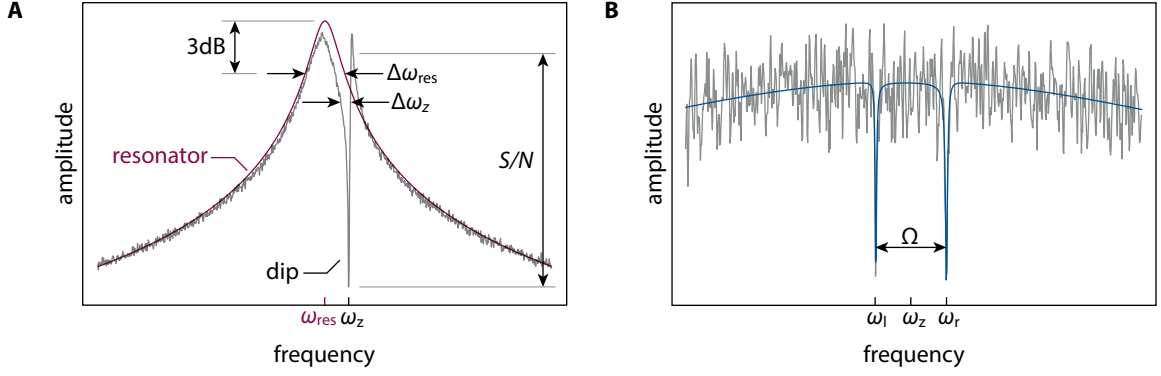


Fig. 2.4: (A) The red line shows the theoretical resonance curve of a parallel resonant circuit with 3 dB width $\Delta\omega_{res}$ and resonance frequency ω_{res} . The gray line represents a simulated dip spectrum of a particle with axial frequency ω_z . The slightly detuned particle $\omega_{res} - \omega_z > 0$ leads to a dispersive spectrum. The signal-to-noise ratio S/N defines the difference between signal level and noise background. (B) Double dip spectrum with the characteristic two dips ω_1 and ω_r separated by Ω . Together with the excitation frequency ω_{rf} such a spectrum allows the determination of ω_+ or ω_- .

The external force F_e originates by two effects and can be expressed as

$$F_e = \frac{q}{D_z} U_{ind} + F_C . \quad (2.36)$$

The force F_C is a result of the Coulomb interaction between induced image charge and ion. For a single particle this force is small and is neglected for now. The first term originates from the induced image current I which leads to a voltage drop $U_{ind} = Z_{res} I$ on the electrode with the connected resonator. The result is an electric force due to the potential difference with respect to the electrode on the opposite side which has no resonator connected. Together with equation (2.31) the equation of motion can be rewritten to

$$\begin{aligned} U_{ind} &= m \frac{D_z^2}{q^2} \frac{dI}{dt} + m \frac{D_z^2}{q^2} I \gamma + m \omega_z^2 \frac{D_z^2}{q^2} \int I dt \\ &= l_p \frac{dI}{dt} + R_{eff} I + \frac{1}{c_p} \int I dt \end{aligned} \quad (2.37)$$

with the definitions $l_p = m \frac{D_z^2}{q^2}$ and $c_p = \frac{1}{m \omega_z^2} \frac{q^2}{D_z^2}$. The damping is related to the effective resistance of the resonator $R_{eff} = m \frac{D_z^2}{q^2} \gamma = \text{Re}(Z_{res}(\omega))$ with the real part as the dissipative component. The equation of motion is the same as for an $l_p c_p$ series circuit with applied voltage U_{ind} across it which motivates the description of the particle by the equivalent circuit diagram shown in figure 2.3 B.

To describe the measured signal in the frequency domain, which characterizes the lineshape, the total impedance Z_{tot} of the particle $Z_p = i\omega l_p + (i\omega c_p)^{-1}$ and effective resonator resistance $R_{eff}(\omega)$ is considered

$$\text{Re}(Z_{tot}(\omega)) = \text{Re} \left(\frac{1}{Z_p} + \frac{1}{R_{eff}} \right)^{-1} = R_{eff}(\omega) \frac{(\omega^2 - \omega_z^2)^2}{(\omega^2 - \omega_z^2)^2 + \left(\frac{\omega R_{eff}(\omega)}{l_p} \right)^2} , \quad (2.38)$$

where the relation $\omega_z^2 = \frac{1}{c_p^2 l^3}$ was used. Figure 2.4 shows the lineshape with a resonance curve in red due to $R_{\text{eff}}(\omega)$ and a *dip* due to the particle interaction. A series circuit acts as a short on its resonance frequency, therefore the particle “shorts” the resonator spectrum.

The parallel resistance R_{res} which characterizes the losses in the system can also be described by the dimensionless quality factor Q

$$R_{\text{res}} = Q \omega_{\text{res}} L_{\text{res}} . \quad (2.39)$$

This quantity is easily found by measuring the 3 dB width of the resonance curve on a logarithmic scale

$$Q = \frac{\omega_{\text{res}}}{\Delta\omega_{\text{res}}} . \quad (2.40)$$

A high Q -value, or a sharp resonance, corresponds to a system with small losses. The width of the dip $\Delta\omega_z$ is related to the damping constant in equation (2.37)

$$\Delta\omega_z \equiv \frac{1}{\tau_z} \equiv \gamma = \frac{R_{\text{eff}}}{m} \frac{q^2}{D_z^2} . \quad (2.41)$$

The parameter τ_z denotes the associated cooling time constant of the detection system.

In case of more than one particle similar arguments can be made starting with an induced image charge of $I = N \frac{q}{D_z} \dot{Z}$ with the particle number N and the center of mass motion Z . The dip width $\Delta\omega_z$ becomes, to first order, a linear function in N which is a very helpful relation to characterize the amount of particles stored in the trap.

To actually detect a spectrum as shown in figure 2.4 A the Johnson-Nyquist noise [63] must be considered. Any resistor at given temperature T has intrinsic electronic noise and can be modeled as an ideal resistor with a noise voltage source in series. The associated noise amplitude at a spectral width $\Delta\nu$ is $u_n = \sqrt{4k_B T R \Delta\nu}$. The resonator noise source u_{res} is included in figure 2.3 B and adds to the intrinsic input noise u_{in} of the cryogenic low-noise amplifier which defines the signal-to-noise ratio

$$S/N = \frac{\sqrt{(u_{\text{res}} \kappa)^2 + u_{\text{in}}^2}}{u_{\text{in}}} . \quad (2.42)$$

The dimensionless factor κ accounts for the coupling of the resonator to the amplifier, for example by an inductive or capacitive voltage divider with 1:10 decoupling. The noise sources are uncorrelated and thus added quadratically. To extract the axial frequency from such a noise spectrum the line model is fit to the *Fast Fourier Transformed* (FFT) time signal. The precision of such a fit depends on the signal-to-noise ratio S/N , the linewidth $\Delta\omega_z$, the measuring time t_{avg} and the resolution. The fit routine is discussed in more detail in section 4.6.

So far the detection principle has been discussed for the axial detection system. A typical dip width for axial detection lies in the range of 1 Hz, which can be measured easily with an FFT spectrum analyzer in about one minute [64]. In order to determine the free cyclotron frequency two more frequencies ω_{\pm} are required. However, using the typical numbers of a cyclotron resonator one ends

up with a dip with of about 4 mHz. The width is limited by the three order of magnitude smaller inductance and the lower Q -value of the detector. A direct detection of the cyclotron frequency via a dip detection is possible but technically challenging and fortunately, a far better tool to measure magnetron and free cyclotron frequency exists - the technique of sideband coupling.

2.6 Sideband coupling

The technique of *sideband coupling* is used to measure ω_{\pm} by coupling the radial modes to the axial mode which leads to a unique signature in the dip spectrum, a *double dip*. Starting with the equation of motion (2.3) an additional driving force is introduced by applying an external radiofrequency drive with frequency ω_{rf}

$$F_{\text{rf}} = q E_0 \operatorname{Re} \left(e^{i\omega_{\text{rf}} t} \right) \begin{pmatrix} z \\ 0 \\ x \end{pmatrix} \quad (2.43)$$

which couples the x to the z component and vice versa. E_0 is the amplitude of the coupling-field gradients. It can be shown [51, 65] that for an excitation frequency of $\omega_{\text{rf}} = \omega_{\pm} \mp \omega_z$ the axial mode exchanges energy with the modified cyclotron frequency or magnetron mode, respectively². The corresponding energy exchange rate between two modes is defined by the Rabi-frequency

$$\Omega = \frac{qE_0}{2m\sqrt{\omega_z\omega_{\pm}}} . \quad (2.44)$$

As a consequence sidebands occur in the single dip spectrum at $\omega_{1/r}$ as illustrated in figure 2.4 B. For experimental conditions an unknown detuning δ must be taken into account since the real sideband excitation frequency ω_{rf} is not known ab initio. Assuming a detuned excitation frequency

$$\omega_{\text{rf}} = \omega_{\pm} \mp \omega_z + \delta \quad (2.45)$$

the sidebands have the frequencies

$$\omega_l = \omega_z \mp \frac{\delta}{2} - \frac{\Omega_{\delta}}{2} \quad \text{and} \quad \omega_r = \omega_z \mp \frac{\delta}{2} + \frac{\Omega_{\delta}}{2} , \quad (2.46)$$

where the Rabi frequency with detuning

$$\Omega_{\delta} = \sqrt{\Omega^2 + \delta^2} \quad (2.47)$$

was used. Thus, for a detuning $\delta > 0$ the magnetron sidebands are shifted toward higher frequency whereas in the case of the modified cyclotron frequency the sidebands are shifted towards lower frequencies.

²Notation: Throughout this section the upper signs in all equations describe the case of the modified cyclotron frequency ω_+ , whereas the lower signs belong to the case with the magnetron frequency ω_- .

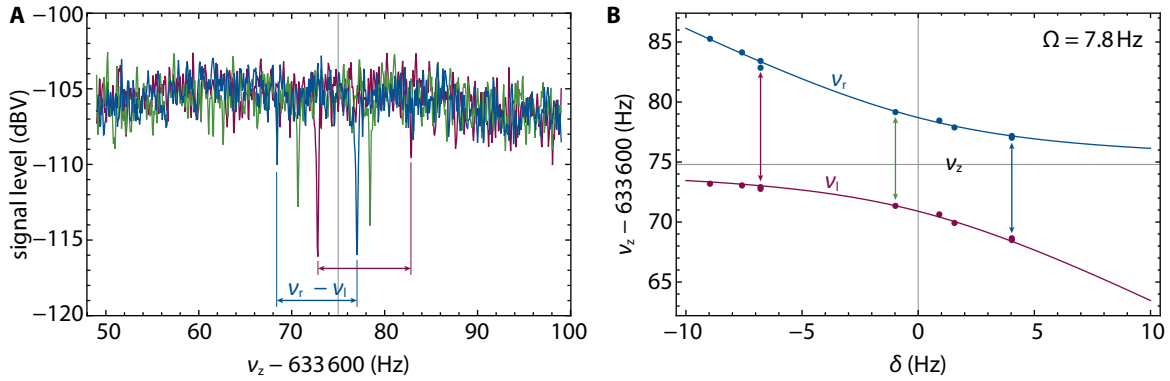


Fig. 2.5: **(A)** Axial noise spectrum of three cyclotron double dips for different radiofrequency excitations with detuning. The vertical gray line shows the position of the axial frequency. The double dip position shifts as a function of the applied detuning. **(B)** Position of the two sideband $\nu_{r,l}$ in blue and red based on several cyclotron double dip measurements as a function of the detuning. The arrows correspond to the three double dips in (A). For a detuning of $\delta = 0$ the double dip is symmetric around the axial position (horizontal gray line).

Based on an independent measurement of ω_z and a successive measurement of ω_l and ω_r the frequencies ω_{\pm} can be calculated from these measurements by

$$\begin{aligned}
 (\omega_{\pm})_{\text{meas}} &= \pm\omega_l \pm \omega_r \mp \omega_z + \omega_{\text{rf}} \\
 &= \pm \underbrace{\left(\omega_z \mp \frac{\delta}{2} - \frac{\Omega_{\delta}}{2}\right)}_{\omega_l} \pm \underbrace{\left(\omega_z \mp \frac{\delta}{2} + \frac{\Omega_{\delta}}{2}\right)}_{\omega_r} \mp \omega_z + \underbrace{(\omega_{\pm} \mp \omega_z + \delta)}_{\omega_{\text{rf}}} \\
 &= \omega_{\pm} .
 \end{aligned} \tag{2.48}$$

The unknown detuning cancels and the measured frequencies $(\omega_{\pm})_{\text{meas}}$ are independent of δ and yield the true frequencies ω_{\pm} .

Apart from its importance for the measurement of the radial mode frequencies sideband coupling is also used to control the mode energies. Based on the relation between radii and mode energies, section 2.1, sideband coupling is used to achieve a smaller particle radius which leads to smaller frequency shifts in the presence of trap imperfections. During the excitation with the sideband frequency ω_{rf} the two respective modes reach a thermal equilibrium with $\langle n_{\pm} \rangle = \langle n_z \rangle$ [51]. Since the axial detection system has a temperature of T_z the energies of the coupled modes can be expressed by

$$\langle E_{\pm} \rangle = \pm \frac{\omega_{\pm}}{\omega_z} k_B T_z \tag{2.49}$$

weighted by the frequency ratio. Each time the coupling occurs the modified cyclotron mode or the magnetron mode will acquire a fixed energy. The probability for a certain energy is Boltzmann distributed with an expectation value of $\langle E_{\pm} \rangle$, thus characterized by the detector temperature. Due to the probabilistic nature several cooling attempts might be required to reduce the radius below a desired threshold. The shape of this Boltzmann distribution can be manipulated by changing the temperature of the axial detector T_z with the technique of active electronic feedback.

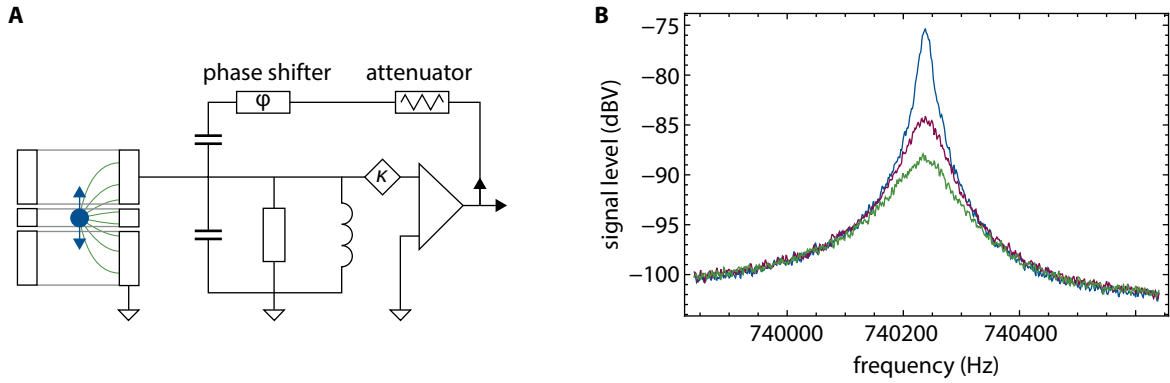


Fig. 2.6: (A) Schematic scheme for feedback control. The signal is fed back, attenuated and phase shifted to damp or excite the particle's motion. (B) Result of the feedback control on a resonator. The Q-value can be changed by properly adjusting phase and attenuation.

2.7 Electronic feedback control

The application of electronic feedback [66] is used to manipulate the temperature of detection systems by feeding the signal back on the detection system. A voltage controlled attenuator, as shown in figure 2.6 A, is made use of to control the signal's strength. The phase shifter is used to apply positive ($\varphi = 0$), negative feedback ($\varphi = \pi$), or any desired phase in between.

Reference [67, 68] describes in detail how the effective feedback temperature T_{FB} is related to the original Q-value of the detection system

$$\frac{T_{\text{FB}}}{T_z} \geq \frac{Q_{\text{FB}}}{Q} \quad (2.50)$$

with Q_{FB} the quality factor during feedback application. This is shown in figure 2.6 where the Q-value is varied with negative feedback and the blue curve is the original resonance spectrum. The inequality is a result of the not neglectable amplifier input noise which prevents the temperature to be lowered to arbitrarily small values. For very high feedback strengths more and more noise is coupled back on the particle and effectively increases the temperature. Thus, the minimum achievable temperature is limited by the input noise of the amplifier. This becomes important in case of the cyclotron detector which must be preperated as cold as possible, see section 4.1.

2.8 Continuous Stern-Gerlach effect

The spin precession frequency ω_L is not accompanied by an image current induced in the trap electrodes and can thus not be measured by the method of image current detection. Instead, the spin-flip probability $p_{\text{SF}}(\omega_{\text{rf}})$, which is the probability to change the spin state from up to down or vice versa, is probed as a function of an applied excitation frequency ω_{rf} . The result is the Larmor resonance with characteristic lineshape which can be fit to extract ω_L . To measure p_{SF} experimentally the spin

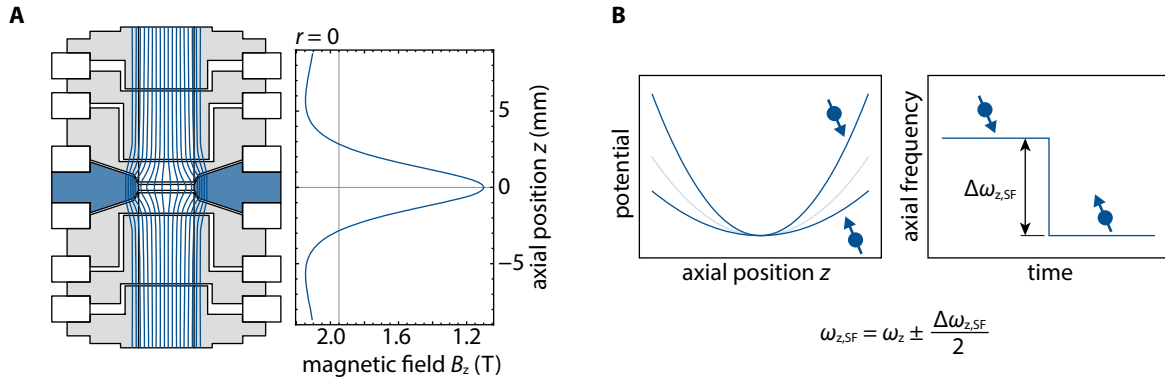


Fig. 2.7: (A) The figure shows the electrode setup of the analysis trap. The ring electrode in the center (blue) is made of ferromagnetic material. The vertical magnetic field lines pass through the standard copper electrodes but are distorted by the ring electrode. This leads to the characteristic shape of the magnetic bottle. (B) The potential $V_m = -\boldsymbol{\mu} \cdot \mathbf{B}$ modifies the axial potential. As a consequence the particle has a different axial frequency as a function of the spin state.

state before and after an excitation must be known and this demands a spin state sensitive detection scheme.

The spin state is measured by employing the *continuous Stern-Gerlach effect* [69] which leads to a coupling between the spin magnetic moment $\boldsymbol{\mu}$ in equation 2.23 and the axial motion via a strong inhomogeneous magnetic field, called *magnetic bottle*

$$\mathbf{B}(z, \rho) = B_0 \mathbf{e}_z + B_2 \left(\left(z^2 - \frac{\rho^2}{2} \right) \mathbf{e}_z - \rho z \mathbf{e}_\rho \right) \quad (2.51)$$

with quadratic component B_2 in superposition on the homogeneous field B_0 . In contrast to the famous experiment by Stern and Gerlach [70] the spin state is read out continuously and without particle loss. The coupling between magnetic moment and magnetic field with potential energy $V_m = -\boldsymbol{\mu} \cdot \mathbf{B}$ leads to an additional force $-\partial_z V_m$ and adds to the equation of motion of the axial frequency. As a result of this coupling the absolute axial frequency

$$\omega_{z,\text{SF}} = \sqrt{\frac{2qC_2V_r}{m} \pm \frac{2\mu B_2 e_z}{m}} \approx \omega_z \pm \frac{\Delta\omega_{z,\text{SF}}}{2} \quad \text{with} \quad \Delta\omega_{z,\text{SF}} = \frac{2\mu_z B_2}{m\omega_z} = \frac{g}{2} \frac{q\hbar B_2}{m^2\omega_z} \quad (2.52)$$

becomes a function of the spin state with a frequency difference between up and down of $\Delta\omega_{z,\text{SF}}$. This allows the direct non-destructive readout of a change in the spin state by measuring the axial frequency. This elegant scheme was introduced by Dehmelt and was first applied with great success to electrons [26] and later also on hydrogen-like ions [71, 72]. A comparison between the proton and the electron shows that the frequency difference $\Delta\omega_{z,\text{SF}}$ is much smaller due to the ratio

$$\Delta\omega_{z,\text{SF}} \sim \left(\frac{\mu_z}{m_p \omega_z} \right)_{\text{proton}} \ll \left(\frac{\mu_z}{m_e \omega_z} \right)_{\text{electron}} \quad (2.53)$$

Assuming the same magnetic bottle B_2 the frequency change due to a proton spin flip is more than 10 000 times smaller at $\nu_{z,p} = 0.6 \text{ MHz}$ and $\nu_{z,e} = 60 \text{ MHz}$. It was not until 2011 that such proton

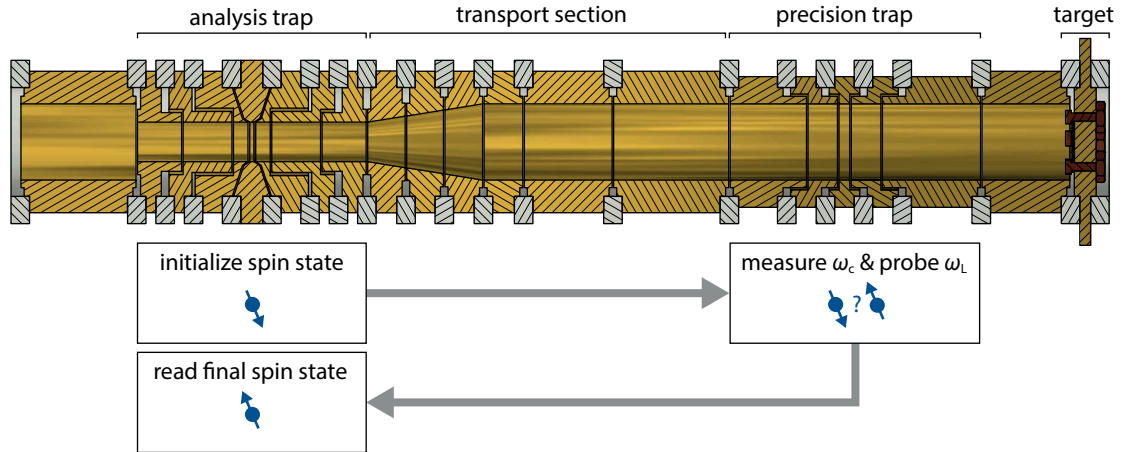


Fig. 2.8: The method starts in the AT where the spin state is determined, e.g. spin down. The particle is then transported to the PT where ω_c is measured in the homogeneous magnetic field. Simultaneously the Larmor frequency is probed with an excitation. Depending on the excitation frequency the proton spin state has changed with probability p_{SF} . To determine the spin state after the excitation the particle is again transported to the AT and the final spin state is read out.

spin flips were statistically detected for the first time [73]. Finally, in 2013 further improvements in the axial stability allowed the observation of single discrete spin flips [74]. These advances became possible through the implantation of a very strong magnetic bottle $B_2 = 298\,000\text{ T m}^{-2}$ and the systematic reduction of background noise. Even today the reduction of the background noise is still one of the crucial experimental difficulties towards detecting single proton spin flips, as will be discussed in detail in section 3.1.

2.9 Double trap scheme

The usage of a strong magnetic bottle is essential for the determination of the proton spin state. Its strength, however, poses a fundamental limitation for the determination of the eigenfrequencies. The axial motion oscillates with an amplitude r_z which is a function of its energy. For typical axial energies of $E_z = k_B T_z \approx 4 k_B$ the axial amplitude is around $50\ \mu\text{m}$. In the presence of the magnetic bottle a change of $50\ \mu\text{m}$ corresponds to a change in the magnetic field of $0.8\ \text{mT}$. This leads to shift on the Larmor frequency by $20\ \text{kHz}$ on a total frequency of $50\ \text{MHz}$.

An accurate description of the width of the Larmor resonance line yields

$$\delta\omega_L = \frac{1}{m\omega_z^2} \frac{B_2}{B_0} k_B T_z \omega_L \quad (2.54)$$

and it was demonstrated that the g factor is limited at the ppm (part per million) level [45, 73]. This technique was also recently used to measure the antiproton g factor with $0.8\ \text{ppm}$ [46]. In order to reach precisions at the ppb level or below, a line width reduction is mandatory. However, neither the frequencies ω_z and ω_L nor the magnetic field B_0 can be changed as they are constrained by the

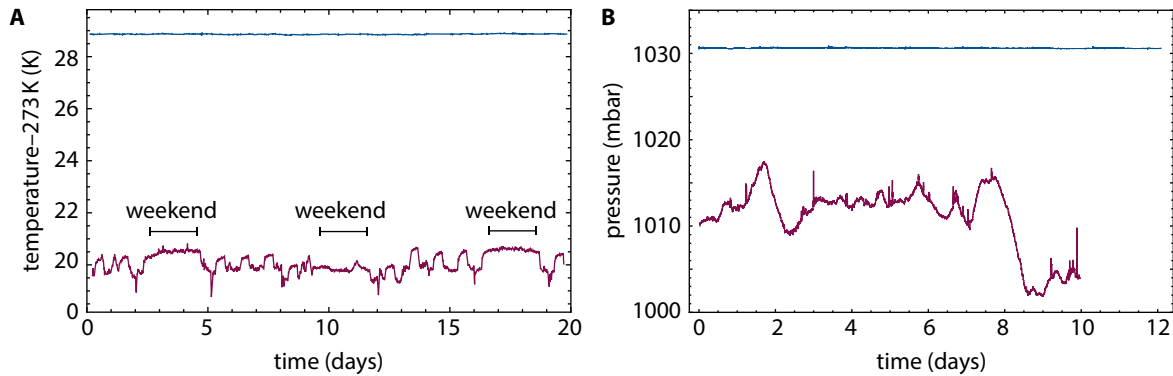


Fig. 2.9: (A) The red line shows the lab temperature. Each work day the ventilation is started in the morning. The temperature in the box is shown in blue. The temperature set point well above the room temperature to have a well decoupled system. (B) The red line shows the temperature in helium recovery line. To stabilize the pressure in the cryostat and in the magnet a setpoint of 1030 mbar is used.

experiment. Furthermore a reduction of the axial temperature to the mK range is not feasible and also a decrease of the magnetic bottle strength B_2 cannot be done without losing the ability to detect spin flips.

An elegant solution to this problem is the spatial separation of spin state detection and high-precision frequency measurements by utilizing two traps. This *double trap technique* was first introduced by H. Häffner and co-workers [47] and later successfully implemented in the proton g -factor experiment [75]. The analysis trap (AT) contains the magnetic bottle is used for the spin state detection, whereas the precision trap (PT) has an about 100 000 more homogeneous magnetic field and is used for the high-precision frequency determination.

A double trap measurement is schematically shown in figure 2.8. The measurement starts in the AT where the spin state is identified. In the next step the particle is transported to the precision trap and the free cyclotron ω_c is measured at the same time as a probe frequency $\omega_{\text{rf}} \approx \omega_L$ is applied to induce a change in the spin state. Since the spin state after the excitation is not known, the particle is finally transported back to the AT and the spin state is read out once more. The information about the initial and the final spin state is used to decide whether a spin flip occurred in the PT. Repeating this sequence for several hundred probing frequencies the Larmor resonance is scanned and eventually the g factor can be determined.

2.10 Experimental setup

The experimental setup is shown in figure 2.10 and is similar to the setup of the prior proton run [76, 48]. The Penning trap system is placed in the horizontal bore of a superconducting magnet at $B = 1.9\text{ T}$ which is oriented with its north pole facing north-northwest ($342(5)^\circ$). A cryostat filled with liquid helium and nitrogen cools the setup down to temperatures near 4 K at the position of the trap. The 4 K stage is surrounded by an additional 77 K shields to reduce the thermal load. The table

with the cryostat on top can be rotated in all directions which allows the adjustment of the angle of the trap with respect to the magnet bore. Also the relative position of the trap with respect to the magnet center can be adjusted due to a flexible bellow.

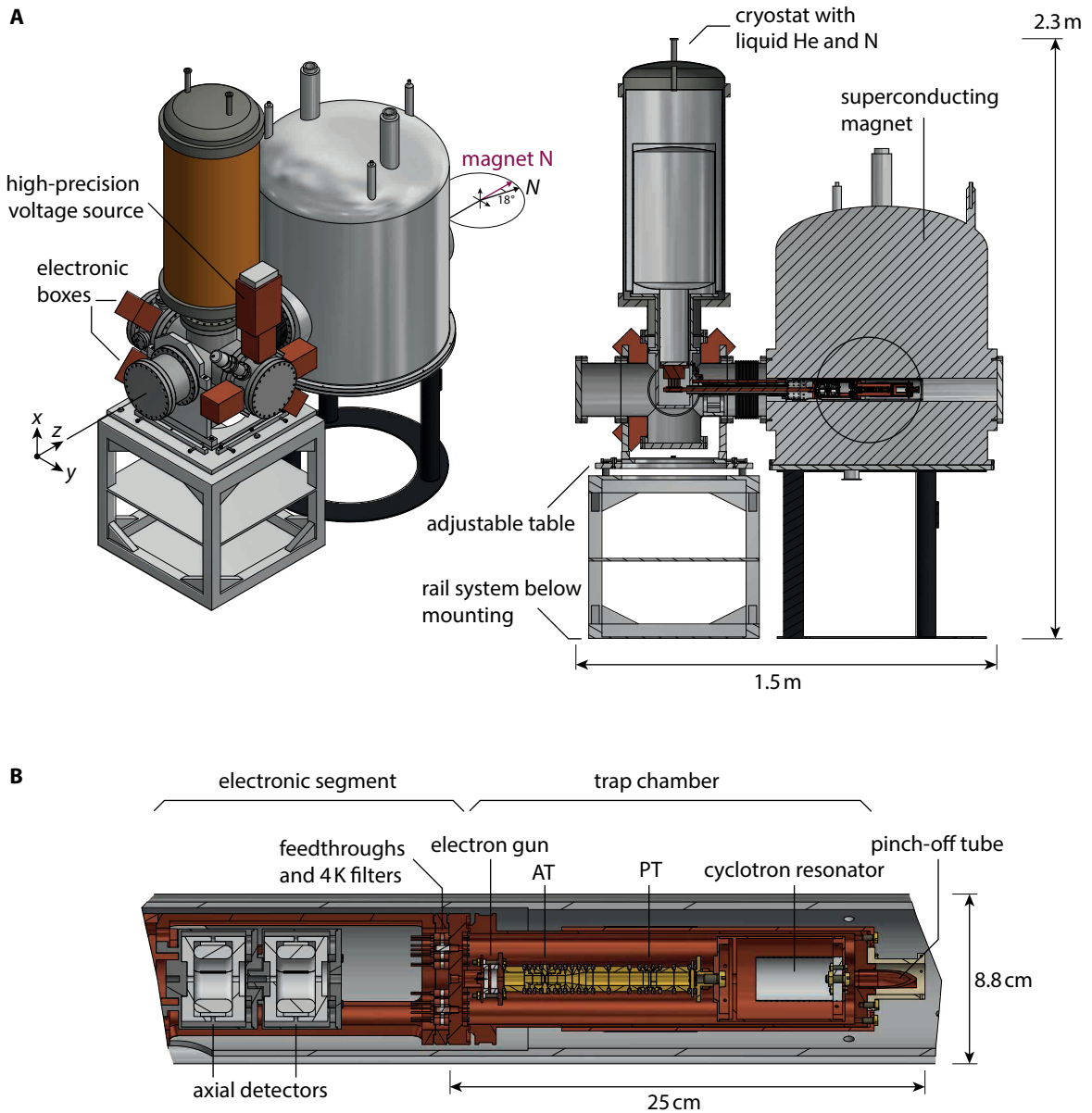


Fig. 2.10: (A) 3D and cut view of the whole experiment (temperature stabilization not shown) The magnet bore is tilted by 18° with respect to the geographic north. The various electronic boxes contain switches, filters and feedthroughs to the vacuum chamber. (B) Zoomed view of inner setup composed of electronic segment and trap chamber. The electronic segment contains the two axial resonators as well as the axial amplifiers. The cyclotron resonator is placed in the trap chamber below the trap system of AT and PT. An additional electron gun allows the in trap production of protons.

The whole setup is surrounded by a (not shown) wooden box for an active temperature stabilization. Within the box all room temperature electronics, such as supplies, switches and excitation generators are placed. The box is typically heated by a conventional space heater to about 29°C. This allows a decoupling from the lab temperature which typically varies by 19 – 21°C. The heater is controlled by a PID controller whose temperature sensor is placed in the air of the box. Heater pulses are integrated by the thermal mass of the apparatus. Temperature data of the stabilized box is shown in figure 2.9 A.

The helium reservoir is connected to a helium recovery line. The temperature of the 4 K stage is correlated to the pressure in the helium cryostat vessel, and pressure fluctuations thus lead to particle instabilities. To reduce pressure fluctuations the Helium reservoir of cryostat and magnet are actively stabilized to about 30 mbar above atmospheric pressure, see figure 2.9 B. The nitrogen reservoirs have a reduced influence on the particle due to their indirect coupling to the 4K trap chamber.

The inner part of the experiment inside the magnet bore contains the electronic segment and the trap chamber, both at 4 K. Two superconducting axial resonators are placed in the electronic segment [64] and are directly connected to the pinbase where all electrical feedthroughs are placed. The feedthroughs lead into the trap chamber which is hermetically sealed. This is achieved by pumping the trap chamber at room temperature to pressures of 10^{-7} mbar through a small copper tube soldered in the trap chamber. The copper tube is then pinched-off which effectively seals the inner volume by cold welding the copper tube. The pinched-off volume allows pressures below 10^{-14} Pa [77] which ensures a clean environment for stable particle storage.

Inside the chamber the trap system is assembled consisting of the electrode gun, the analysis trap (AT) and the precision trap (AT). On top of the trap system the cyclotron resonator is attached. The electrodes are made of oxygen-free copper and galvanically gold plated with a layer of 8 μm gold on top of 7 μm silver. Both traps are designed in orthogonal and compensated design [45]. To electrically isolate them from each other sapphire rings are placed in between. The ring electrode of the AT is made of ferromagnetic Co/Fe to create the strong magnetic inhomogeneity.

The electron gun is used to create electrons at defined energies by field emission. The electrons hit a polyethylene target on the opposite side of the trap system where, due to the impact, atoms are sputtered of the surface and are subsequently ionized by the electron beam. Positively charged fragments are captured in the precision trap. Dedicated cleaning procedures such as voltage ramps or selective excitations allow the preparation of a single proton.

An extract of the complete connection diagram (appendix B.1) is shown in figure 2.11 for the PT. The first column (I) shows the instruments connected to the apparatus at room temperature. The second column (II) lists all electronic boxes at room temperature. The connections are guided by vacuum feedthroughs to the vacuum part of the experiment. (III) and (IV) are filter stages at 77 K and at 4 K, respectively. The pinbase between (IV) and the trap chamber (V) contains all electronic feedthroughs. The various types of connections are labeled with 1 – 11 and are similar to the connections in the rest of the trap system. Line (1) shows a feedback line which is guided by a low temperature coax cable. The end is mounted in close proximity to the axial detection line to allow for a capacitive signal coupling. Line (2) and (3) are part of the axial detection system. The green box in

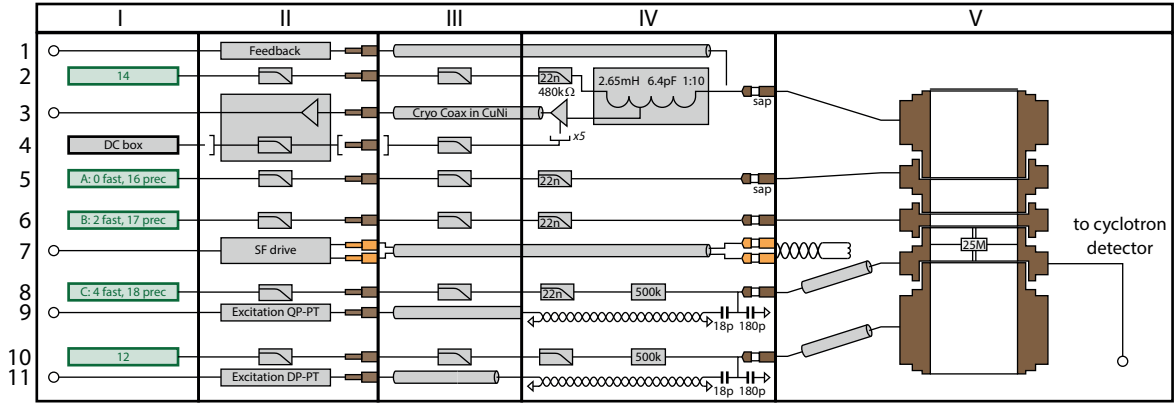


Fig. 2.11: Exemplary connection scheme of the precision trap. Details are explained in the text.

(I) is the high-precision voltage source UM1-14 from *Stahl-Electronics*. This DC connection is filtered three times in (II)-(IV) by low pass filters. If not indicated otherwise the RC filters have $R = 500 \text{ k}\Omega$ and $C = 8.2 \text{ nF}$. The axial resonator coil is shown as a gray box. One end of the coil is connected to the DC line. The other end is directly connected to a sapphire feedthrough on the pinbase. The signal is picked up by an inductive voltage divider with $\kappa = 0.1$. The signal is amplified at (IV) and at (II) indicated by the triangles. The cryogenic amplifier requires 5 DC connections shown by connection (4). The axial detector is then directly connected to the endcap of the precision trap. Lines (5),(6) and (8) are the precision channels of the voltage source to bias the trap electrodes. As all DC connections they are filtered at all three stages (II)-(IV). Line (7) is the connection for the spin-flip coil positioned in the trap chamber (V) to drive magnetic dipole transitions between the spin states. The spin-flip coils are also used to drive quadrupole excitations such as a magnetron coupling in the AT, where no segmented electrode is mounted. The two lines (9) and (11) are excitation lines. The connection is made with a coaxial cable in combination with a twisted pair. The rf-signals merge on the pinbase with the DC lines (8) and (10) which are blocked by a $500 \text{ k}\Omega$ resistor. To reduce external noise on the unfiltered excitation lines a capacitive voltage divider is used. Inside the trap chamber the lines are connected with the electrodes by coax cables. (9) is used for the quadrupole excitation to drive sidebands and is thus connected to a segmented electrode. The two segments are connected by a $25 \text{ M}\Omega$ resistor. The other segment is used for a connection to the cyclotron resonator which is placed inside the trap chamber to minimize the wire length.

The experiment is controlled by LabVIEW from *National Instruments* which allows the readout and programming of all instruments related to the experiment. The signal readout is performed with a SR780 Dynamic Signal Analyzer by *Stanford Research Systems* (SRS) which was modified to accept a 10 MHz clock input. The frequency lock is supplied by a FS725 Rubidium Frequency Standard from SRS and is used for all instruments such as various frequency generators.

Chapter 3

The Analysis Trap (AT)

The analysis trap is used to measure the proton spin state and is thus indispensable to the double-trap technique. Due to the intrinsic weakness of the proton magnetic moment a strong magnetic inhomogeneity is required to couple the proton spin to the axial motion. However, this *magnetic bottle* makes the analysis trap a challenging environment to work with. This chapter introduces the theoretical description of the axial frequency stability followed by experimental results. Several optimizations were implemented to reach the highest stability ever achieved in a proton analysis trap. Finally, the AT is characterized with respect to trap harmonicity and detector temperature..

3.1 Stability of the axial frequency

3.1.1 Theoretical description

It was shown before in section 2.8 that in the analysis trap the axial frequency depends on the spin state of the proton due to the presence of the magnetic bottle characterized by $B_{2,AT}$. A change of the spin state $\Delta m_s = \pm 1$ leads to a measurable frequency change of

$$|\Delta v_{z,SF}| = g \frac{q\hbar B_{2,AT}}{8\pi^2 m^2 v_z} \approx \frac{1}{4\pi^2} \frac{h v_+ B_{2,AT}}{m v_z B_{0,AT}} \frac{g |\Delta m_s|}{2} = 172(3) \text{ mHz} . \quad (3.1)$$

A large magnetic bottle $B_{2,AT} = 298\,000(5000) \text{ T m}^{-2}$ is beneficial to obtain a significant change in the axial frequency but also introduces energy dependent frequency shifts as introduced in equation (2.28). The absolute axial frequency is given by

$$\Delta v_z(E_+, E_-, m_s) = \frac{1}{4\pi^2} \frac{h v_+ B_{2,AT}}{m v_z B_{0,AT}} \left[\left(n_+ + \frac{1}{2} \right) + \frac{v_-}{v_+} \left(n_- + \frac{1}{2} \right) + \frac{g}{2} m_s \right] , \quad (3.2)$$

where the energies were replaced with the corresponding energy levels of a quantum harmonic oscillator with principal quantum number n_{\pm} and $m_s = \pm \frac{1}{2}$. A change of the principal quantum number $n_+ \rightarrow n_+ \pm 1$ introduces a frequency shift of $\Delta v_z = 62 \text{ mHz}$ and a change from $n_- \rightarrow n_- \pm 1$ a

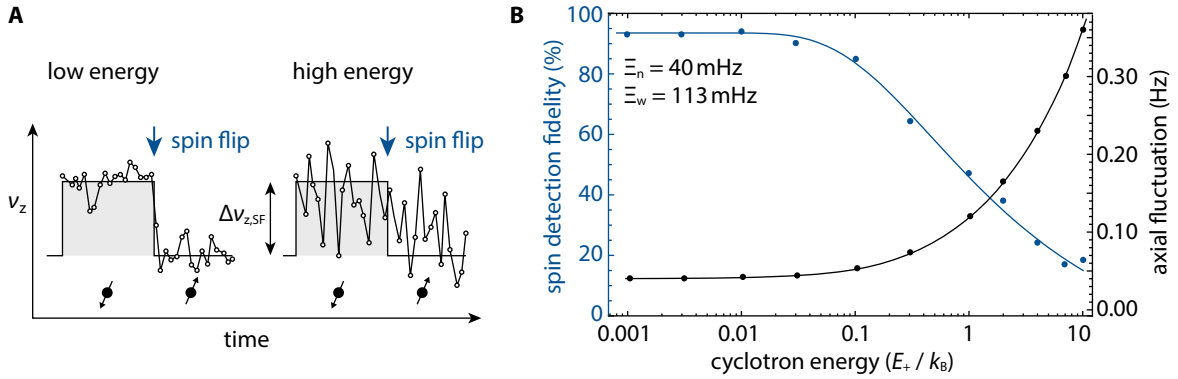


Fig. 3.1: (A) Schematic sequence of axial frequency measurements in the analysis trap in the presence of a spin flip (blue arrow) for low and high energy. In case of low energy the background noise is sufficiently low to assign a spin flip event based on the axial frequencies. In case of high energy and thus large background fluctuations no spin flip can be identified. (B) The axial fluctuation is a function of energy which is directly correlated to the spin detection fidelity in blue. 100% fidelity is never reached because the background noise never reduces to zero.

shift of $\Delta v_z = 52 \mu\text{Hz}$, respectively. In the presence of many quantum transitions the spin state detection becomes less reliable or even impossible which is characterized by the *spin state detection fidelity*. The probability to determine the correct spin state, greatly depends on the ability to distinguish the frequency change due to a spin flip from the background noise on the axial frequency. Figure 3.1 A illustrates subsequent measurements of the axial frequency over time. During the axial frequency measurements a spin flip occurs, indicated by the blue arrow. As a consequence the axial frequency changes which can be seen easily in case of the low energy particle. In the case of a high energy particle the background fluctuations are large compared to $\Delta v_{z,SF}$ and the spin flip is not detected.

The origin of the background fluctuations are spurious *transition rates* $p_+ = dn_+/dt = \dot{n}_+$ and $p_- = dn_-/dt = \dot{n}_-$ which must be minimized to achieve a high fidelity. It can be shown with time dependent perturbation theory [78, 58], that the transition rates scale proportionally to the principal quantum numbers $p_{\pm} \sim n_{\pm} \sim E_{\pm}$ which means that a particle with lower energy exhibits smaller heating rates.

To further investigate the axial stability in the analysis trap a series of axial frequency measurement $\{v_1, v_2, \dots, v_n\}$ is assumed. To measure the axial stability independently of slow drifts of the axial frequency, which are for example caused by temperature drifts in the voltage supply, the *axial fluctuation* $\delta_i = v_i - v_{i+1}$ is introduced with $i \in \{1, \dots, n-1\}$. The standard deviation for this set of axial frequency differences $\Xi = \text{sd}(\delta_i)$ is to first order normally distributed and characterizes the axial stability.

In order to achieve the highest possible spin state detection fidelity the axial fluctuation must be

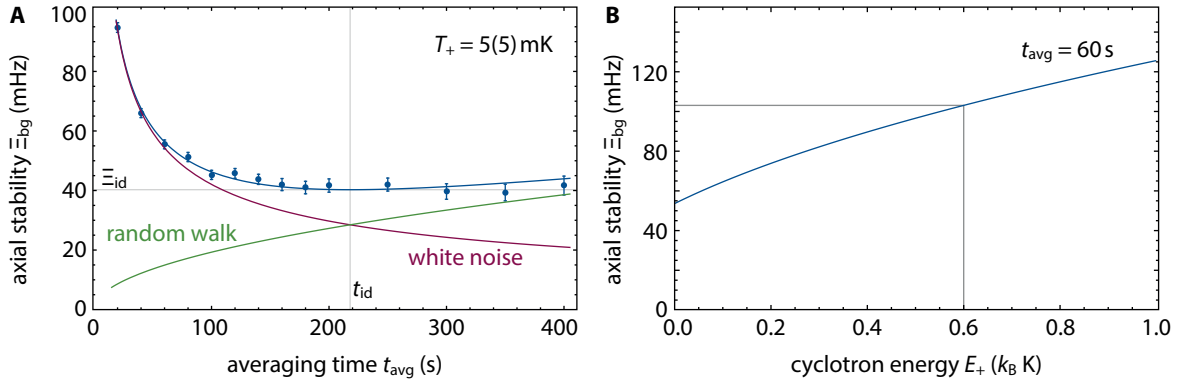


Fig. 3.2: (A) Allan deviation of the axial stability for a proton with $T_+ = 5(5)$ mK. The blue line shows a fit based on the two contributions of random walk (green line) and white noise (red line). At an ideal averaging time of 220 s a stability of 40 mHz is achieved. The random walk in this data set corresponds to in average one quantum jump each 12 min. (B) Axial stability as a function of modified cyclotron energy. All data was recorded with an averaging time of $t_{\text{avg}} = 60$ s. Typically, proton temperatures $E_+ \leq k_B 600$ mK are used for the experimental g -factor routine.

minimized. The background fluctuation Ξ_{bg} is composed of two components

$$\Xi_{\text{bg}} = \sqrt{\Xi_n(t_{\text{avg}})^2 + \Xi_w(t_{\text{avg}})^2} = \sqrt{\frac{s_n^2}{t_{\text{avg}}} + s_w^2 t_{\text{avg}}}, \quad (3.3)$$

which are illustrated in figure 3.2 A. The white noise component $\Xi_n(t_{\text{avg}})$ decreases with increasing FFT averaging time with square root of t_{avg} and predominantly arises due to fit and voltage noise. The random walk component, which mainly arises due to the modified cyclotron transition rate, increases with time. A minimization with respect to t_{avg} shows that the ideal measurement time is given by $t_{\text{id}} = \sqrt{s_n^2/s_w^2}$ with an ideal stability $\Xi_{\text{id}} = \sqrt{2s_n s_w}$. At the measurement time t_{id} white noise Ξ_n and random walk Ξ_w have the same contribution to the overall fluctuation. To connect the fluctuation to the model of cyclotron quantum jumps the walk contribution can be expressed as a function of the cyclotron transition rate [58]

$$\Xi_w = \sqrt{\frac{1}{\sqrt{2}} \Delta v_{z,+}^2 p_+ t_{\text{avg}}} \Rightarrow s_w^2 = \frac{1}{\sqrt{2}} \Delta v_{z,+}^2 p_+. \quad (3.4)$$

$p_+ = p_+(E_+)$ is a linear function of the modified cyclotron energy and is the essential parameter to obtain a suitable axial stability. For a constant averaging time the expected behavior is described by

$$\Xi_{\text{bg}} = \sqrt{\frac{s_n^2}{t_{\text{avg}}} + \frac{1}{\sqrt{2}} \Delta v_{z,+}^2 p_+(k_B T_+) t_{\text{avg}}} \sim \sqrt{a + b T_+}, \quad (3.5)$$

where a and b are constants. Such a behavior is shown in figure 3.2 B with a non-zero offset at $E_+ = 0$. In contrast, if the ideal averaging time t_{id} is chosen, the behavior is

$$\Xi_{\text{bg}} = \sqrt{2s_n \sqrt{\frac{1}{\sqrt{2}} \Delta v_{z,+}^2 p_+(k_B T_+)}} \sim c T_+^{1/4} \quad (3.6)$$

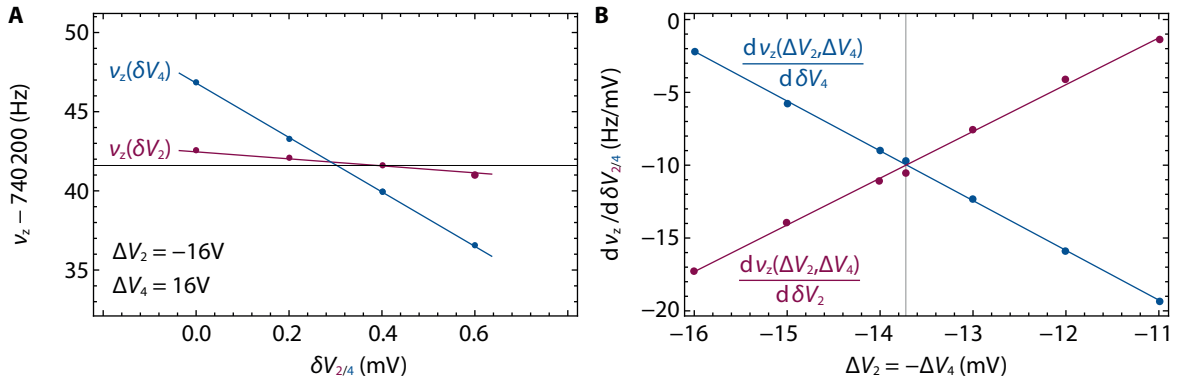


Fig. 3.3: (A) The axial frequency is measured as a function of a change on one correction electrode. The blue curve is for a variation δV_4 , while the red curve is a variation δV_2 on the other correction electrode. This is repeated for several sets of offset voltages $\Delta V_2 = -\Delta V_4$ until both frequency shifts are identical. (B) The plot shows the slopes as introduced in (A). For offsets $\Delta V_2 = -\Delta V_4 = -13.7(2)$ V on the correction electrodes the frequency shifts are identical and the trap asymmetry is compensated.

with constant c . In the ideal case, the fluctuations vanish for $E_+ \rightarrow 0$ with an averaging time of $t_{\text{id}} \rightarrow \infty$. During the measurement a fixed averaging time is typically chosen, but it can be advantageous to characterize the noise carefully in order to determine the ideal averaging for several cyclotron energies.

3.1.2 Experimental optimization and characterization

To characterize the axial stability as a function of temperature and averaging time the particle is tuned into resonance with the axial detector and the particle signal is measured in the time domain with an *M-AUDIO FastTrack Pro* soundcard. Afterward, the data is processed by a *Fast Fourier Transform* (FFT) algorithm with variable settings. The result of a 16 h time signal is shown in figure 3.2 A where the same signal was analyzed for different averaging times. The theoretical model for random walk and white noise contribution is in excellent agreement with the measured data. The best stability is achieved for an averaging time of about 220 s with $\Xi_{\text{id}} = 40$ mHz. This is a significant improvement of 15 mHz compared to the previous experimental run [76] and improves the spin state detection fidelity by about 10%, compare figure 3.1 B. The stability during the g -factor measurement is shown in figure 3.2 B as a function of the modified cyclotron energy at a constant averaging time.

To reach the stability stated here many optimizations of the analysis trap were required and are discussed briefly within this section as well as adjustments that had little or no effect. It should also be noted, that not for all steps the improvement in mHz was explicitly measured because some steps were performed at the same time.

- **Axial temperature and trap anharmonicity**

The temperature of the axial resonator and the trap's anharmonicity play an important role for a high axial stability due to the coupling of the particle energy to the axial frequency in

the presence of electrostatic imperfections. A lower resonator temperature leads to a narrower distribution of particle energies and thus a sharper axial dip. As a consequence of the improved measurement precision and the smaller white noise contribution a higher axial stability is achieved. The resonator temperature was reduced by active feedback and the trap anharmonicity was minimized by scanning the trap's tuning ratio.

- **Asymmetry compensation**

Small potential offsets on the order of several mV on individual electrodes or small machining and alignment errors in the trap setup break the symmetry of the trap and cause deviations from the ideal potential. These asymmetries can be partially compensated with small offset potentials ΔV_i on the trap electrodes [58]. Typically, asymmetries are compensated for the correction electrodes V_2 and V_4 as well as for the endcaps V_1 and V_5 . An offset on the ring electrode is of no concern because it effectively shifts the absolute value of TR which is optimized independently.

As a first step, the endcap offsets are set to zero $\Delta V_1 = \Delta V_5 = 0$ and only the correction electrodes are tuned. A voltage variation δV_2 on one correction electrode shifts the center of the potential and changes the C_j coefficients (section 2.2) which leads to an axial frequency shift $\Delta \nu_z(\delta V_2)$. In a perfectly symmetric trap a change δV_4 on the opposite correction electrode would lead to the same frequency shift $\Delta \nu_z(\delta V_4)$ and a comparison between both frequency shifts enables the minimization of the asymmetry. Figure 3.3 A shows such a measurement of the axial frequency as a function of applied offset voltages on the correction electrodes. The two offsets ΔV_2 and ΔV_4 to compensate the asymmetry are varied until the frequency behavior is identical for variations δV_2 or δV_4 . The result of such a measurement sequence is shown in figure 3.3 B with the point of intersection at $\Delta V_2 = -\Delta V_4 = -13.7(2)$ mV when a symmetric frequency change is measured. Note, that this kind of compensation is arbitrary in a sense, that any offset on one correction electrode, for example of 1 mV, can either be compensated by a 1 mV offset on the opposite correction electrode, by -1 mV on the same correction electrode or by two offsets with $+0.5$ mV and -0.5 mV on both electrodes.

In the next step, a *global asymmetry compensation* is performed by applying a voltage to one endcap. However, this offset on the endcap changes the offset on the correction electrodes that minimize the trap asymmetry and for each new voltage ΔV_1 the correction electrode compensation $\Delta V_{2/4}$ has to be redone. The process is repeated until both slopes are identical and, in addition, $d\nu_z/d\delta V_4 = 0 = d\nu_z/d\delta V_2$. This led to the final setting of $\Delta V_1 = -462$ mV and $\Delta V_{2/4} = \mp 27.9$ mV.

After the implementation of the global asymmetry compensation the axial frequency stability changed from 40(1) mHz to 37(2) mHz. During the g -factor measurement only the correction electrode compensation was used because the influence of the global compensation on the stability was too small to justify the usage of second UM1-14 voltage supply which would have been necessary to apply a stable voltage to the endcap.

- **Endcap switches**

All traps in the experiment are operated with a UM1-14 voltage supply which provides three ultra-stable channels for the ring electrode and the two correction electrodes (typically $0.1 \mu\text{V}$ fluctuations) along with less stable, additional channels for the endcaps (typically $10 \mu\text{V}$ fluctuations). To get rid of the much higher fluctuations on the endcaps *KEMET EE2-5SNUH* signal relays were implemented. These are used to short the endcaps to ground instead of applying 0 V with the UM1-14. Fluctuations on the endcap have a significant impact on the axial frequency stability and the switches immediately improved the quality of the dip S/N .

- **Temperature stabilization**

The external temperature of the laboratory has a large influence on the axial frequency which is mostly due to temperature dependent voltage drifts of the voltage source. A change of 1 K on the voltage supply temperature corresponds to a voltage change of $10 \mu\text{V}$ which shifts the axial frequency by 3.7 Hz . To achieve a temperature stability of 10 mK , which corresponds to an axial stability of $> 36\text{ mHz}$, the whole setup is surrounded by a temperature stabilized box with an internal temperature of 29°C . The voltage source is furthermore surrounded by a massive copper block to remove small fluctuations.

- **Low-pass filters** To reduce short-time fluctuations of the voltage source film capacitors with $47 \mu\text{F}$ were connected to all channels at room temperature. With these filters connected the voltage requires a couple of minutes to settle down to its final value. At the current level of precision no effect on the stability was observed which indicates that the measurement was not limited by the voltage stability. However, for future applications when limited by voltage fluctuations such filters might prove useful.

- **Cable connectors**

The original setup used several BNC cables to guide the ultra-stable voltage channels to the trap. These allowed quick access to the channels for probing or to apply higher voltages for trap cleaning. However, measurements confirmed that such BNC connectors are highly sensitive to external temperature changes such as heating pulses from the PID controlled temperature stabilization. Temperature fluctuations change the contact potentials between the male and the female plug which creates offset voltages in the order of several μV and shifts the particle by a few Hz . Soldered connections, SMA-connectors or gold-plated banana plugs are typically less sensitive to such influences by around one order of magnitude. For that reason, all BNC connections were replaced with solder joints and SMA-connections which greatly improved the stability.

- **Cryo-liquid pressure stabilization** The pressure in the helium cryostat has a direct influence on the temperature of the 4 K stage and is thus correlated to the frequency stability of the proton. A pressure stabilization for the helium reservoir was installed and set to 1030 mbar . The frequency dependence also applies to the nitrogen reservoir. However, due to a negligible effect on the stability at the current level of precision no pressure stabilization was installed. Such

a stabilization will be of potential interest for a further improved apparatus.

3.2 Detection system temperature

During the detection with a dip spectrum, the proton is in constant thermal equilibrium with the detector and the expectation value of the axial energy is related to the detector temperature $\langle E_z \rangle = k_B T_z$. Due to the continuous energy thermalization the axial frequency permanently changes in the presence of B_{2AT} and electrostatic imperfections C_4 , as described by equation (2.28). The dip spectrum “smears out” resulting in a smaller signal-to-noise ratio. A smaller S/N leads to a larger white noise contribution or equivalently to a larger uncertainty on the frequency measurement. Thus, a small axial temperature is crucial and must be optimized carefully.

To measure the axial temperature of the detection system the technique of sideband cooling is being used. During the excitation with the coupling drive at $\nu_z - \nu_-$ the magnetron mode and axial mode exchange energy and reach an equilibrium state defined by

$$\langle E_- \rangle = -\frac{\nu_-}{\nu_z} \langle E_z \rangle = -\frac{\nu_-}{\nu_z} k_B T_z \Rightarrow T_- = -\frac{\nu_-}{\nu_z} T_z < 0, \quad (3.7)$$

where the average magnetron energy is connected by the frequency ratio to the temperature of the axial detection system. Once the coupling drive is turned off in cycle (i) the magnetron temperature acquires an arbitrary but fixed value $T_-^{(i)}$ on a Boltzmann distribution

$$\rho(T_-^{(i)}) = -\frac{1}{k_B T_-} \exp\left(-\frac{T_-^{(i)}}{T_-}\right). \quad (3.8)$$

Due to the magnetic bottle the axial frequency is shifted as function of the magnetron temperature

$$\Delta\nu_z(T_-^{(i)}) = \frac{1}{2\pi} \frac{1}{m\omega_z} \frac{B_{2,AT}}{B_{0,AT}} k_B T_-^{(i)} = 71.4 \text{ Hz K}^{-1} T_-^{(i)} \quad (3.9)$$

after each coupling. The process of coupling both modes and measuring the axial frequency $\nu^{(i)}$ is repeated several hundred times. The resulting frequency distribution $\{\nu^{(1)}, \dots, \nu^{(n)}\}$ is transformed to extract the temperature information

$$\{T^{(1)}, \dots, T^{(n)}\} = \left\{ \frac{\nu^{(1)} - \nu_{\min}}{72 \text{ Hz K}^{-1}}, \dots, \frac{\nu^{(n)} - \nu_{\min}}{72 \text{ Hz K}^{-1}} \right\} \quad (3.10)$$

with $\nu_{\min} = \min(\{\nu^{(1)}, \dots, \nu^{(n)}\})$ which defines the “cut” of the Boltzmann distribution with $T_{\min} = 0 \text{ K}$. Note that the routine must run sufficiently long to have a high probability that the estimated cut is likely to be the real cut.

Figure 3.4A shows the result of such a measurement with the result of $T_z = 18.1(6) \text{ K}$.¹ This rather high temperature is due to undesired positive feedback from the amplifier which became

¹The data was analyzed using a maximum likelihood analysis based on the probability density $\rho(T)(1 - \Theta(T - T_{\max}))$. T_{\max} denotes the highest temperature that could have been recorded based on the limited frequency span on the FFT. The Heaviside Theta function Θ cuts off the upper tail of the Boltzmann distribution that was outside the experimental resolution. This becomes important for large temperatures when a large fraction of data points lies not within the frequency window that is recorded.

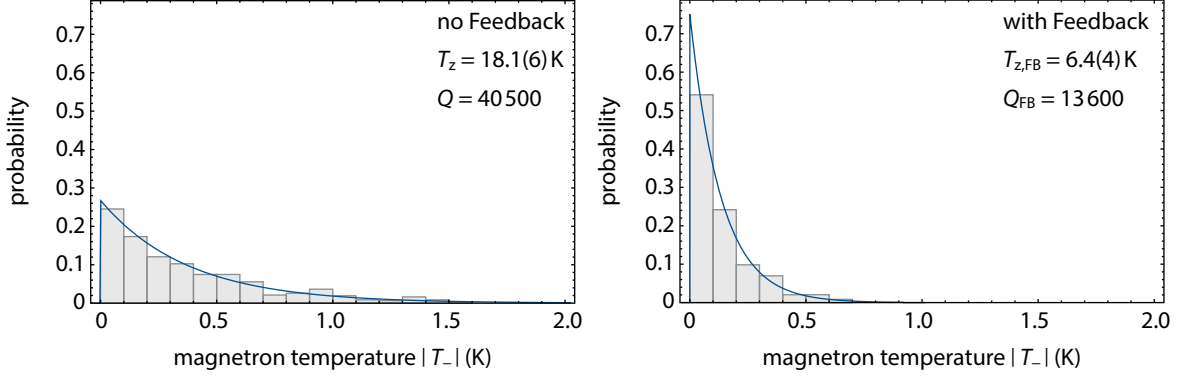


Fig. 3.4: The axial temperature is measured by successively coupling magnetron and axial mode. The resulting distribution yields the temperature of the detection system. Feedback, right side, greatly reduces the axial temperature.

worse over time since the Q-value of the resonator increased by almost a factor of two within two years. To obtain a lower temperature and thus a better axial frequency stability negative feedback was used [67]. The Q-value was decreased to 13600 which corresponds to an expected temperature change of $T_{z,FB} = T_z \cdot Q_{FB}/Q = 18.1 \cdot 13600/40500 = 6.1$ K. This theoretical expectation is in good agreement with the directly measured value of $T_z = 6.4(4)$ K, figure 3.4 B.

3.3 Tuning ratio optimization

In the presence of electrostatic field imperfections and the magnetic bottle the axial frequency shifts as a function of energy which limits the frequency stability. While the magnetic bottle cannot be reduced, the anharmonicities of the electrostatic potential can be minimized by optimizing the tuning ratio TR . Typically, two different methods are used to minimize the anharmonicities.

The first is the optimization of the dip signal-to-noise ratio. This is illustrated in figure 3.5 where several spectra can be seen as a function of the tuning ratio. At the step size of $\Delta TR = 5 \times 10^{-5}$ the ideal TR can be clearly identified as the black spectrum.

The behavior of the S/N as a function of TR , indicated by the dashed line, can be described analytically. Starting from the lineshape for the dip as introduced in equation (2.38) and (2.42) the trap anharmonicities in case of a non-ideal tuning ratios must be taken into account, because they introduce energy dependent frequency shifts. Due the continuous energy exchange between the axial detector and the proton the thermal Boltzmann distribution has to be convoluted with the original lineshape of the dip, resulting in

$$\chi(\omega) = R_{\text{eff}}(\omega) \frac{1}{T_z} \int \frac{(\omega^2 - \tilde{\omega}_z^2)^2}{(\omega^2 - \tilde{\omega}_z^2)^2 + \left(\frac{\omega R_{\text{eff}}}{T_p}\right)^2} e^{-\frac{T}{T_z}} dT, \quad (3.11)$$

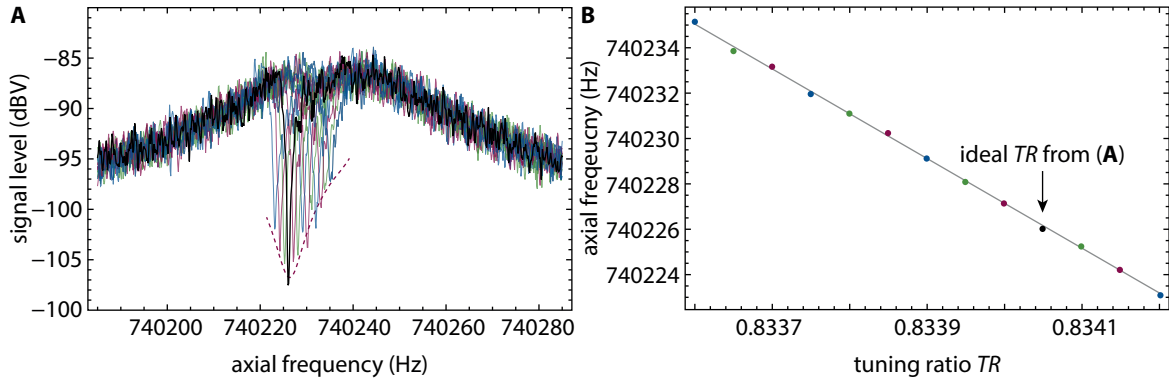


Fig. 3.5: (A) TR scan by recording a dip spectrum for each TR value. The tuning ratio was varied from 0.8336 to 0.8342. The ideal TR with best signal-to-noise ratio is indicated by the black line. The dashed red line indicates the theoretical expectation for the signal-to-noise ratio. (B) Absolute frequency as a function of the tuning ratio. This characterizes the trap dependent parameter D_2 with $\Delta\nu_z = -19.75(15) \text{ Hz TR}^{-1}$.

where

$$\tilde{\omega}_z = \omega_z \left(1 + \frac{3 D_4 \Delta TR}{4 C_2^2} \frac{k_B}{qV_0} T_z \right) \quad (3.12)$$

is the shifted frequency due to the anharmonicities. The ideal tuning ratio is defined by the condition $\omega_z = \tilde{\omega}_z$ or equivalently $\Delta TR = TR - TR_{\text{id}} = 0$. The logarithmic signal-to-noise ratio is then obtained by

$$S/N_{\text{theory}} = 10 \log_{10} \left[\frac{\left(\sqrt{4k_B T_z \chi(\omega)} \kappa \right)^2 + u_{\text{in}}^2}{u_{\text{in}}^2} \right]. \quad (3.13)$$

The result of this equation is shown by the dashed line in figure 3.5 A and is in good agreement with the observed behavior. The parameter D_4 only depends on the trap geometry and can be calculated from potential theory. The S/N_{theory} relation can also be used the other way around to obtain the unknown axial detector temperature T_z by measuring the scaling of the S/N . However, the decoupling κ and u_{in} must be known to ensure precise predictions. Furthermore, it must be ensured that higher order contributions such as C_6 have no significant impact on the axial frequency.

The second method uses feedback to find the ideal tuning ratio. Feedback can be used to change the temperature of the axial detector with the relation $T_{z,\text{FB}} = T_z Q_{\text{FB}}/Q$ where Q is the quality factor of the resonator without feedback and F_{FB} with feedback. To find the ideal tuning ratio, the axial frequency is measured at various tuning ratios with and without feedback and the each frequency difference is related to the theoretical expectation

$$\Delta\tilde{\omega}_z = \omega_z \left(1 + \frac{3 D_4 \Delta TR}{4 C_2^2} \frac{k_B}{qV_0} T_z \right) - \omega_z \left(1 + \frac{3 D_4 \Delta TR}{4 C_2^2} \frac{k_B}{qV_0} T_{z,\text{FB}} \right) \quad (3.14)$$

$$= \omega_z \left(1 + \frac{3 D_4 \Delta TR}{4 C_2^2} \frac{k_B}{qV_0} (T_z - T_{z,\text{FB}}) \right). \quad (3.15)$$

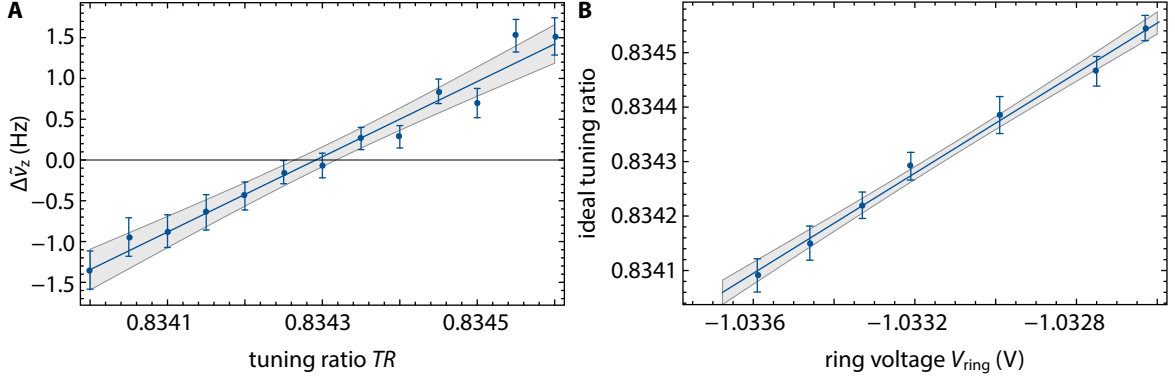


Fig. 3.6: (A) For each tuning ratio the axial frequency was measured with and without feedback. The difference between both measurements is shown in the plot as a function of TR . The ideal tuning ratio is the point where the axial frequency is energy independent and the difference between feedback and no feedback vanishes. (B) The ideal TR depends on the applied ring voltage. Each of the presented data points is a result of an optimization as shown in part A.

Minimizing $\Delta\tilde{\omega}_z$ yields the ideal tuning ratio $\Delta TR = 0$ as shown figure 3.6 A. As for the S/N method the procedure can be repeated to reduce the statistical error. The advantage of the feedback TR scan compared to the S/N analysis is the simpler behavior. The root of a weighted linear fit immediately allows the determination of the ideal tuning ratio without a detailed analytic description or further assumptions. In practice, the S/N method is the typical way to quickly optimize TR or to get a rough first estimate.

The axial frequency in the AT is a function of the absolute particle energy and each particle energy is associated with a different TR and a different ring voltage that centers the particle on the resonator. To avoid scanning TR for each new energy the ideal tuning ratio as a function of the ring voltage was calibrated and is shown in 3.6 B.

3.4 Spin-flip probability

In the presence of spin flips during a measurement sequence of axial frequencies the fluctuation Ξ_{SF} , induced by the spin flips [58], adds to the background fluctuation Ξ_{bg} in equation (3.3)

$$\Xi = \sqrt{\Xi_{\text{bg}}^2 + \Xi_{\text{SF}}^2} = \sqrt{\Xi_{\text{bg}}^2 + p_{\text{SF,AT}} \Delta v_{z,\text{SF}}^2} . \quad (3.16)$$

Equation 3.16 can thus be used to measure the spin-flip probability in the analysis trap for a known background fluctuation. The measurement is conducted by repeating the sequence

$$v_{z,1} \rightarrow v_{\text{ref}} \rightarrow v_{z,2} \rightarrow v_{L,\text{off}} \rightarrow v_{z,3} \rightarrow v_L \rightarrow v_{z,4} \quad (3.17)$$

where the $v_{z,i}$ indicate 60 s axial frequency measurements and $v_L = 49.995$ MHz and $v_{L,\text{off}} = 45$ MHz are 20 s excitations with an on-resonant and an off-resonant excitation to drive spin transitions. Dur-

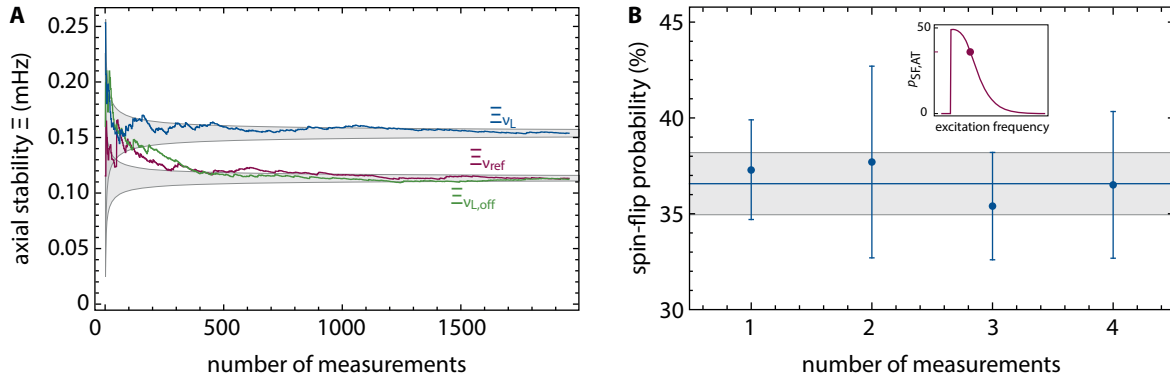


Fig. 3.7: (A) Evolution of the standard deviation for the on-resonant Ξ_{v_L} and off-resonant $\Xi_{v_{L,off}}$ excitation together with the reference measurement $\Xi_{v_{ref}}$ without excitation. The gray error bands show the standard error mean. Reference and off-resonant measurement are perfectly consistent with each other which indicates that no undesired side effects are neglected. (B) The measurement in (A) was repeated four times to gain more statistics. The data was then used to calculate the spin-flip probability. The result is the blue line with gray error band. The small inset shows a schematic Larmor resonance with relative position of the applied excitation drive.

ing v_{ref} no excitation is performed. The corresponding fluctuations are calculated by

$$\Xi_{v_{ref}} = \text{sd}(\{v_{z,1} - v_{z,2}\}), \quad \Xi_{v_{L,off}} = \text{sd}(\{v_{z,2} - v_{z,3}\}), \quad \Xi_{v_L} = \text{sd}(\{v_{z,3} - v_{z,4}\}), \quad (3.18)$$

where the argument of sd contains normally distributed frequency differences. The result of such measurements is shown in figure 3.7. The background fluctuation is consistent between reference and off-resonant measurement, which indicates that no additional dynamic was induced due to the spin-flip drive (such as for example heating effects that change the background fluctuation). The overall result is

$$p_{SF,AT} = 0.366(16) . \quad (3.19)$$

Because the Larmor resonance in the analysis trap is shaped like a Boltzmann distribution due to the thermally distributed axial energy [51, 79], the Larmor drive frequency for the g -factor measurement was tuned a bit higher than the actual ideal Larmor frequency. This ensures that in the event of magnetic field drifts the spin-flip probability does not drop to 0% at the sharp left edge of the distribution but rather moves to the right flank, compare inset in figure 3.7 B .

Chapter 4

The Precision Trap (PT)

In contrast to the analysis trap the purpose of the precision trap is the measurement of the proton eigenfrequencies with highest precision in a homogeneous magnetic field. This chapter introduces a considerably improved cyclotron detector which enabled a two times faster data taking rate in the final g -factor measurement. Furthermore, several trap characteristics such as the tuning ratio, the detector temperature, and the magnetic field are explained in detail, as they will become important for the systematics of the g -factor evaluation. The fit model used to extract the eigenfrequencies from the axial frequency spectra is briefly explained along with its role in future experiments, and finally the lineshape of the g -factor resonance in the PT is discussed.

4.1 Improved cyclotron detector

Section 3.1 discussed the correlation between the cyclotron energy and the axial stability during the determination of the spin state. Low cyclotron energies are crucial to reach a high spin read-out fidelity. However, each cyclotron frequency measurement via sideband coupling increases the cyclotron energy to

$$\langle E_+ \rangle = k_B T_+ = k_B \frac{\omega_+}{\omega_z} T_z \approx k_B 600 \text{ K} , \quad (4.1)$$

leading to a far too high energy to detect spin flips in the analysis trap. To reduce the cyclotron energy to $\langle E_+ \rangle < k_B 1 \text{ K}$ during each cycle, the particle is coupled to a cyclotron resonator and resistively cooled. The cyclotron detector with physical temperature T_+ and coupling constant τ_+ is connected to a segmented correction electrode of the precision trap and acts as a thermal bath. The modified cyclotron mode thermalizes with the resonator as long as it is coupled. Once the coupling is interrupted by tuning the cyclotron resonator frequency away from the particle's modified cyclotron frequency ω_+ , the mode energies "freezes" to a fixed energy. The individual "frozen" energies are Boltzmann distributed and connected to the detection system temperature T_+ .

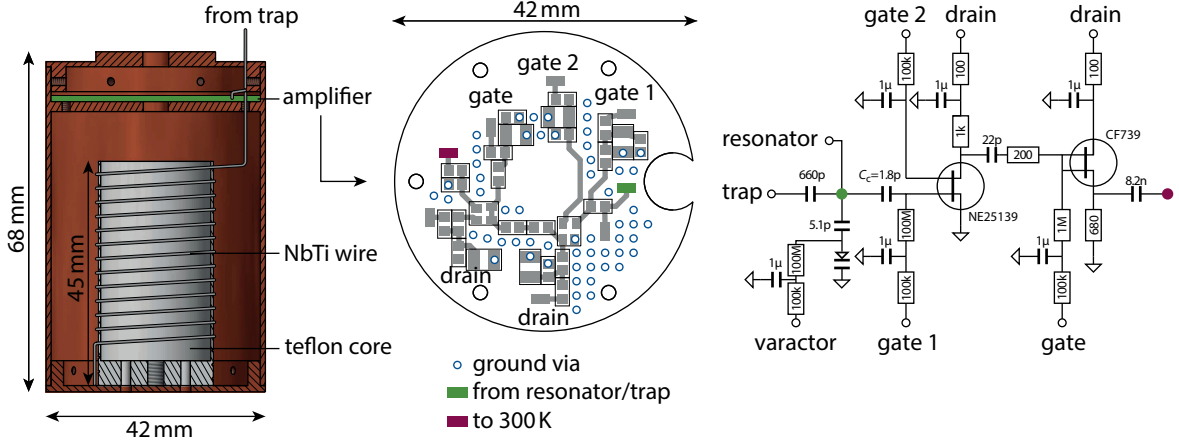


Fig. 4.1: The left part shows a schematic setup of the superconducting coil within the copper housing. The green area shows where the amplifier is placed. The amplifier board layout is shown in the middle, and a schematic of the used electronic components is displayed on the right.

In the previous g -factor measurement [48] the reduction of the particle energy consumed about 100 min out of a total cycle time of 160 min per data point, which is a dramatic limitation for high statistics. For more efficient *cooling*, a resonator with smaller temperature and smaller coupling time is beneficial, as it decreases the number of cooling attempts and the time per attempt, respectively.

The design of the new cyclotron resonator is shown in figure 4.1 and is based on the prior design discussed in [58]. A hollow cylindrical Teflon core with a diameter of 23.1 mm is placed in a polished copper housing. The resonator coil is made out of NbTi superconducting wire and consists of 12.2 turns and a spacing of 2.83 mm between adjacent turns. The *cold end* of the coil is grounded to the housing while the *hot end* is connected to the segmented trap electrode and the amplifier input. To minimize parasitic capacitance, parasitic inductance, and sensitivity to stray noise the resonator is placed inside the trap chamber in close proximity to the PT together with the cryogenic ultra low-noise amplifier which is located inside the copper housing of the resonator assembly. The amplifier layout is the well established design that has been used over several experimental generations [80]. A tunable varactor diode (MACOM MA46H072) is used to tune the resonator frequency at 28.96 MHz within a range of about ± 600 kHz.

To optimize coupling time τ_+ and temperature T_+ the resonator was systematically characterized. The *unloaded* (bare coil, no trap or amplifier attached) quality factor is $Q = 16200$ at a resonance frequency of 85.5 MHz with an inductance of $L_+ = 1.7 \mu\text{H}$. In the next step amplifier, trap and varactor are connected to the resonator as shown in figure 4.1. The varactor is decoupled with a 5.1 pF capacitor which is chosen such that the modified cyclotron frequency is located in the middle of the tunable resonator frequency range. The amplifier is decoupled with $C_c = 1.8$ pF. The whole assembly was tested at 4K for various coupling factors κ defined by

$$\kappa = \frac{C_c}{C_c + C_{\text{in}}} \quad (4.2)$$

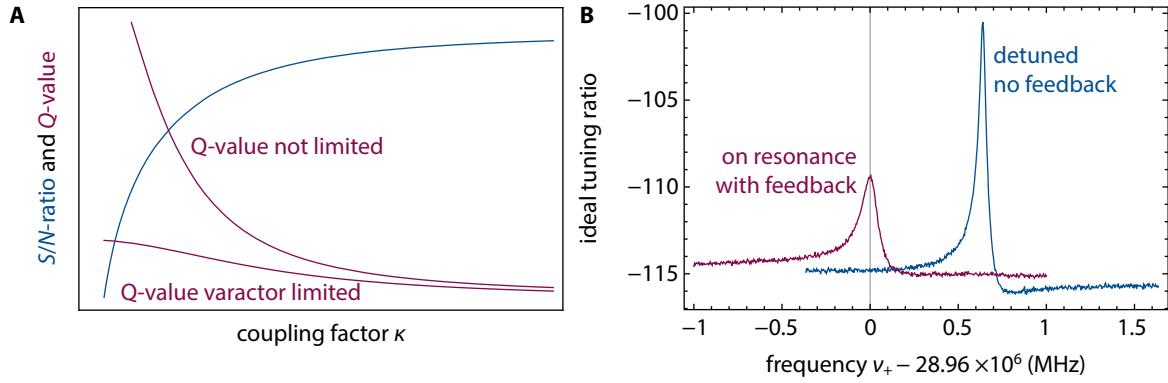


Fig. 4.2: (A) Blue shows the signal-to-noise ratio on a logarithmic scale. The red curves show the behavior of the Q -value as a function of the coupling factor. For further details refer to text. (B) Cyclotron resonator spectrum for the case with/without feedback and detuned/on resonance. Tuning and feedback are independent parameters and only two out of four possible spectra are shown for simplicity.

to analyze the scaling of S/N and Q . The theoretical expectation

$$S/N \approx \frac{\sqrt{4k_B T R_{\text{eff}} \kappa}}{e_n}, \quad Q = \frac{R_{\text{eff}}}{\omega L_+} \quad (4.3)$$

is used to measure the input capacitance $C_{\text{in}} = 1.3(1)$ pF and the input resistance $R_{\text{in}} = 730(30)$ k Ω of the amplifier assuming the independently measured amplifier input noise $e_n = 0.8$ nV $\sqrt{\text{Hz}}^{-1}$. R_{eff} is the effective parallel resistance of the whole system composed of R_{in} and the parallel resistance of resonator and varactor R_p

$$R_{\text{eff}} = \frac{R_{\text{in}} \kappa^{-2} R_p}{R_{\text{in}} \kappa^{-2} + R_p}. \quad (4.4)$$

Both S/N and Q can be tuned by an appropriate choice of κ . This behavior is shown in figure 4.2 A. For large values of κ the signal increases at constant background noise and thus increasing the S/N . At the same time the Q -value usually decreases, since $R_{\text{in}} \ll R_{\text{res}}$ and with larger coupling the input resistance limits the effective parallel resistance more and more. In the opposite case with $\kappa \rightarrow 0$ no signal passes to the amplifier and $S/N \rightarrow 0$. The Q -value, however, increases to the unloaded Q -value unless limited by the varactor. The resonator, as measured during the experimental run is shown in figure 4.2 B and has a quality factor of $Q_+ = 1400$ and a signal-to-noise of $S/N = 15$ dB.

A high Q -value ensures the required small coupling time between particle and resonator for the cooling

$$\tau_+ = \frac{m}{Q_+ \omega_+ L_+} \frac{D_+^2}{q^2} \approx 40 \text{ s}. \quad (4.5)$$

as introduced in section 2.5. Furthermore, the lowest achievable temperature with feedback cooling,

$$T_{\text{min}} \approx 2\sqrt{T_G T_+} \Big|_{T_+=9.6\text{K}} = 3.4 \text{ K} \quad \text{with} \quad T_G = 10^{\frac{S/N}{10}} T_+ \quad (4.6)$$

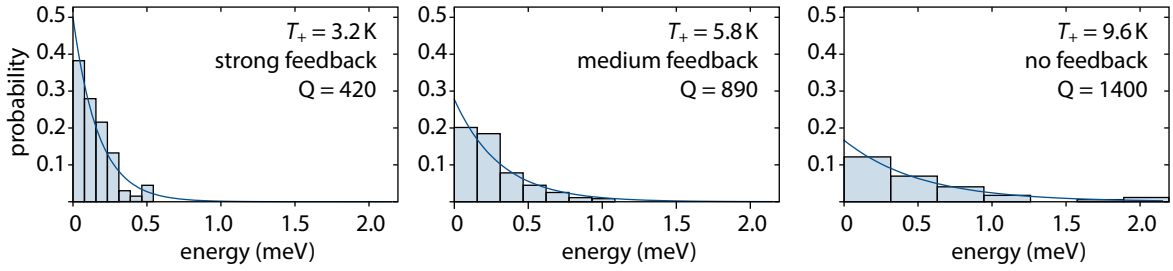


Fig. 4.3: The cyclotron temperature was measured with strong/medium negative feedback and without. The initial temperature of the detection system can be reduced by a factor of 3. The plots show the distribution of successive energy measurements after coupling the proton to the resonator. The slope of the Boltzmann distribution yields the temperature.

is derived in [67] and scales with the signal-to-noise ratio and the initial temperature of the detector $T_+ = 9.6(5)$ K. That is why both a high Q and a high S/N are beneficial but exclude each other. In practice the varactor is the limiting contribution to the overall effective resistance but cannot be decoupled stronger without losing tuneability. As a result, a rather strong coupling of $\kappa = 0.6$ is chosen.

To verify the theoretical expectation of T_{\min} the temperature of the resonator is characterized for different feedback strengths. This is done following the method described in section 3.2. After coupling the proton to the resonator, it is transported to the analysis trap and the energy is measured. This process is repeated until a Boltzmann distribution is recorded that characterizes the temperature. Independent measurements show that the transport itself has negligible influence on the energy and heating effects can be neglected. However, the temperature measure in the analysis trap has to be corrected due to the fact that the magnetic moment is an adiabatic constant [81]

$$\mu_+ = \frac{E_+}{B} . \quad (4.7)$$

This implies that the radial energies change when transporting the particle through a magnetic gradient and the measured energy distribution in the analysis trap is thus corrected by a factor of $B_{0,PT}/B_{0,AT} = 1.6$. The final result of three temperature measurements is shown in figure 4.3. By applying strong feedback a temperature reduction by a factor of three was achieved.

Compared to the previous run [76] the minimum temperature was decreased from 8 K to 3.2 K while the cooling constant was reduced more than a factor of 2. This allows a cold particle to be prepared in the final proton g -factor measurement in about 25 min with an energy < 0.6 K k_B , which is a difference by a factor of 4 compared to the previous measurement. This is a substantial improvement of the new cyclotron resonator – effectively doubling the data acquisition rate during the g -factor measurement.

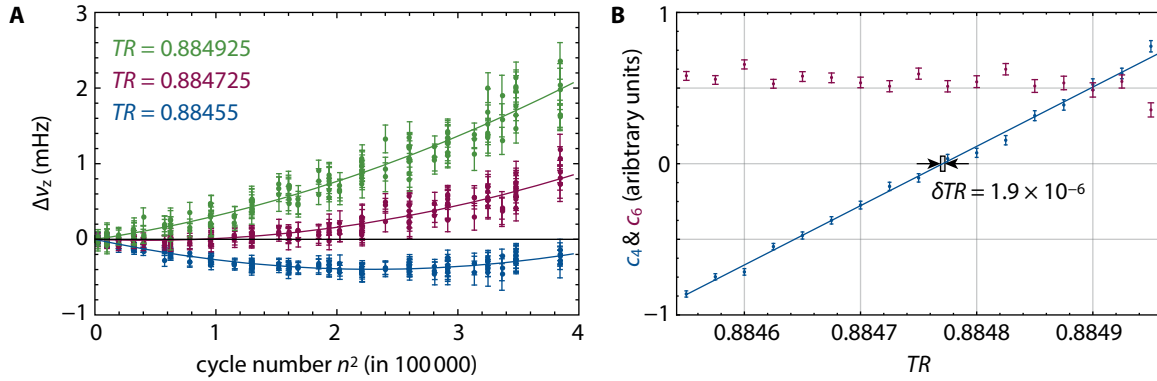


Fig. 4.4: (A) The plot shows the shift of the axial frequency after a magnetron excitation with a defined number of cycles. This is repeated for different cycle numbers and TR . The resulting lines are fitted with a polynomial function that scales proportional to C_4 . Each curve thus leads to a value of C_4 . These are shown in blue in (B) where the ideal TR with vanishing C_4 was determined with a precision of $\Delta TR = 1.9 \cdot 10^{-6}$ after a two week optimization. The data points in red represent the scaling of C_6 which is consistent with a constant.

4.2 TR optimization

The tuning ratio TR in the PT constitutes a critically important parameter for the g -factor measurement since a non-ideal TR leads to systematic shifts on g , see section 2.4. The usual, quick approach to optimize the tuning ratio is to record several dip spectra for different TR and optimizing the signal-to-noise ratio. This was discussed for the analysis trap in section 3.3 but is not as well suited for a high quality TR optimization as the method of magnetron bursts.

The principle is based on equation (2.28) where the axial frequency as a function of the magnetron energy is given by

$$\begin{aligned} \frac{\Delta v_z}{v_z} &= \underbrace{\frac{1}{qV_0} \frac{C_4}{C_2^2}}_{c_4} 3 E_- + \underbrace{\frac{1}{q^2 V_0^2} \frac{C_6}{C_2^4} \frac{45}{4}}_{c_6} \left(E_-^2 - 2 \left(\frac{v_z}{v_+} \right)^2 E_+ E_- + E_z E_- \right) + \mathcal{O}(C_n) \\ &\approx c_4 E_- + c_6 E_-^2 + \mathcal{O}(c_n) \end{aligned} \quad (4.8)$$

with the new coefficients c_j for simplicity. The linear scaling with E_- in the C_6 term is neglected since for small detunings from the ideal TR the behavior is dominated by the term $c_4 E_-$. To measure the frequency shift as a function of the magnetron energy the particle is excited with a burst at the magnetron frequency with fixed excitation time (equivalent to the number of excitation cycles). The number of cycles n of the excitation pulse is proportional to the radius the particle is excited to $n \sim r_-$, hence the energy scales with $E_- \sim n^2$.

The measurement is conducted by first determining the axial frequency of the proton in thermal equilibrium. The proton is then excited with a predefined number of cycles and the shifted axial frequency is measured. With sideband cooling the magnetron energy is brought back to thermal equilibrium and the same scheme is applied again for several different numbers of cycles. The whole

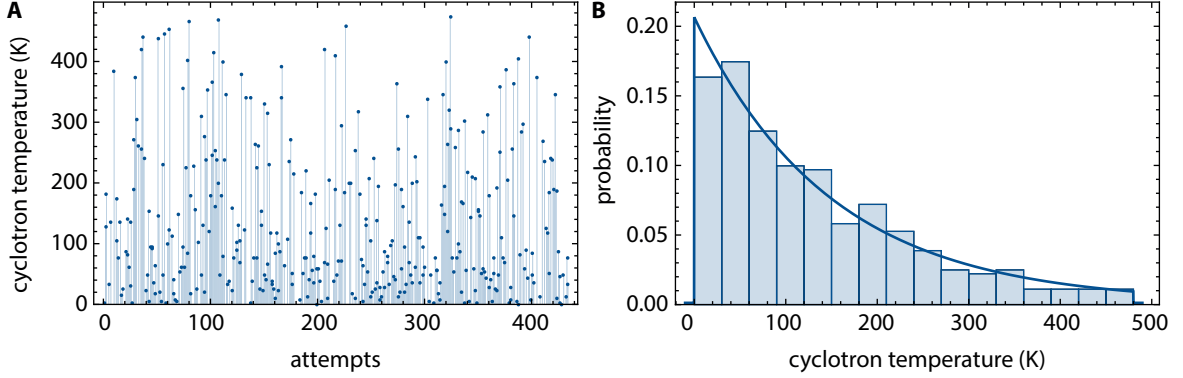


Fig. 4.5: (A) Result of more than 400 energy measurements in the AT after coupling the axial mode to the modified cyclotron mode in the PT. (B) Histogram of the energy distribution. The slope is proportional to the axial temperature of the PT.

process is done for several different TR around the expected ideal TR which is shown in figure 4.4 A. Each color in the plot represents one tuning ratio and is fit with the function defined in equation (4.8). Figure 4.4 B shows the fit parameters c_4 (blue) and c_6 (red) as a function of TR . The root of this curve yields the ideal tuning ratio defined by $C_4 = E_4 + D_4 TR_{id} = 0$. A scaling of c_6 in this scanning range cannot be resolved.

The method described here enables the measurement of TR_{id} with a precision of $\delta TR = 1.9 \cdot 10^{-6}$ within about 12 days. During a test measurement various parameters were changed such as the external temperature of the apparatus, the pressure stabilization or variation with time. No effect on the tuning ratio was observed at the current level of precision. The only influence on TR which can be significant up to shifts of $1 \cdot 10^{-4}$ is a reloading of the trap which changes offset potentials on the electrodes and thus influences the ideal potential configuration. During the g -factor measurement, the tuning ratio was optimized for each individual proton separately. Finally, the tuning ratio was re-measured after two months of continuous operation to verify the original value. Both measurements, $TR = 0.885262(3)$ and $TR = 0.885264(3)$, are in perfect agreement.

4.3 Temperature of the axial detection system

The availability of the magnetic bottle in the analysis trap can be used to directly measure the temperature of the axial detection system in the precision trap. To measure T_z the modified cyclotron mode and the axial mode are coupled. The Boltzmann distributed energy E_+ is then determined in the AT as in section (3.2). The slope T_+ of the Boltzmann distribution yields the axial temperature

$$T_+ = \frac{\nu_+}{\nu_z} T_z . \quad (4.9)$$

Due to the larger energy spread $\nu_+/\nu_z \gg \nu_-/\nu_z$, the temperature determination with the cyclotron sideband provides a more sensitive and robust measurement than the magnetron sideband. Small spurious changes in the magnetron energy during the transport between the traps have insignificant

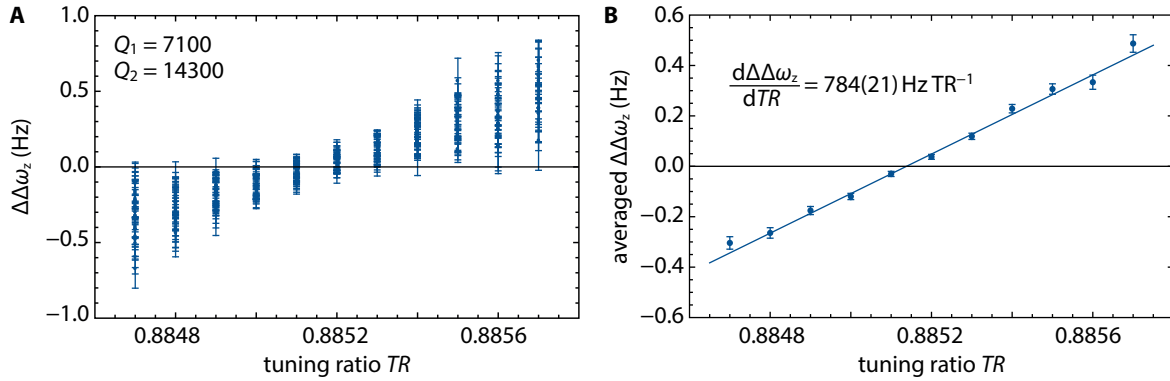


Fig. 4.6: (A) Repeated measurements of $\Delta\Delta\omega_z$ as a function of TR . For each TR the data is averaged and plotted in (B) with a linear fit. The slope is used to characterize D_4T_z .

influence on the E_+ measurement. Independent measurements showed that the energy spread due to the transport is more than three order of magnitude smaller than the cyclotron induced spread which is

$$T_z \frac{v_+}{v_z} \Delta v_z = 4 \text{ K} \frac{28.96 \text{ MHz}}{633665 \text{ Hz}} \frac{72 \text{ Hz}}{\text{K}} \approx 13 \text{ kHz} \quad (4.10)$$

for e.g. $T_z = 4 \text{ K}$. Typically, spectra with a span of 800 Hz are recorded to search for the particle signal in the analysis trap. Ring voltage, as well as the tuning ratio, are then adjusted such that the axial frequency changes about -600 Hz . This is repeated until a particle dip is found within one of these spectra. The distribution of such a measurement sequence is shown in figure 4.5. The measurement was repeated several times and with various feedback strengths. Ultimately, a temperature of $3.65(25) \text{ K}$ was measured. Correcting by the ratios of magnetic fields as introduced in the previous section the temperature of the PT axial resonator, $T_z = 5.9(1.0) \text{ K}$, is obtained.

4.4 D_4T_z characterization

An important input parameter used in the final g -factor evaluation is the product D_4T_z which characterizes systematic electrostatic shifts. After thermalization of each mode with the axial mode, the three mode energies can be expressed by the temperature of the axial detection system $\langle E_+ \rangle = k_B \frac{\omega_+}{\omega_z} T_z$, $\langle E_z \rangle = k_B T_z$ and $\langle E_- \rangle = -k_B \frac{\omega_-}{\omega_z} T_z$. The electrostatic shifts in equation (2.28) then become

$$\frac{\Delta\omega_+}{\omega_+} = \frac{D_4T_z \Delta TR}{C_2^2} \kappa_+, \quad \frac{\Delta\omega_z}{\omega_z} = \frac{D_4T_z \Delta TR}{C_2^2} \kappa_z, \quad \frac{\Delta\omega_-}{\omega_-} = \frac{D_4T_z \Delta TR}{C_2^2} \kappa_- , \quad (4.11)$$

where $C_4 = E_4 + D_4(TR_{\text{id}} + \Delta TR) = D_4 \Delta TR$ was used. The three parameters $\kappa_{+/z/-}$ are known from equation (2.28) and depend on numerical constants and frequency ratios. By measuring the axial shift $\Delta\omega_z$ as a function of the detuned tuning ratio $\Delta TR = TR_{\text{id}} - TR$ the parameter D_4T_z can be characterized.

However, the quantity $\Delta\omega_z = \omega_{z,\text{shifted}} - \omega_{z,0}$ is not directly accessible because the unshifted frequency $\omega_{z,0}$ is unknown. Instead two measurements are conducted at the same tuning ratio, thus

same $\omega_{z,0}$, but different temperatures

$$\begin{aligned}\Delta\Delta\omega_z &= (\omega_{z,\text{shifted}}(T_{z,1}) - \omega_{z,0}) - (\omega_{z,\text{shifted}}(T_{z,2}) - \omega_{z,0}) \\ &= \omega_{z,\text{shifted}}(T_{z,1}) - \omega_{z,\text{shifted}}(T_{z,2}) \\ &= \frac{D_4 T_z \Delta TR}{C_2^2} \kappa_z \left(1 - \frac{Q_1}{Q_2}\right) \omega_z .\end{aligned}\quad (4.12)$$

The temperature change is achieved by varying the Q -value of the detection system with feedback. The temperatures are then related by $T_{z,1} = T_z$ and $T_{z,2} = Q_1/Q_2 T_z$. The absolute temperature is not required to calculate the relative temperature change. The results of such a measurement is presented in figure 4.6. In total four such measurements were performed and yield the final result of $D_4 T_z = 4.75(14) \times 10^{10} \text{ m}^{-4} \text{ K}$

This measurement can also be used to estimate the axial detection system temperature T_z by using the theoretical value for D_4 . Since $D_4 = 3.50(35) \times 10^9 \text{ m}^{-4}$ depends only on the trap geometry, the error can be conservatively chosen to be 10% based on the machining tolerances. This leads to an estimated temperature of $T_z = 13.6(1.4) \text{ K}$ which is in disagreement with the previously measured temperature. Great effort was made to understand this discrepancy and many measurements were conducted but the problem remains yet to be understood. To incorporate both methods, the error was increased to $T_z = 13.6(8.1)$ and the systematic errors for the final g -factor are based on this value.

4.5 Magnetic field contributions

The strong magnetic field inhomogeneity in the analysis trap $B_{2,\text{AT}}$ has a relevant influence on the homogeneity of the precision trap described by $B_{1,\text{PT}}$ and $B_{2,\text{PT}}$.

The linear magnetic field $B_{1,\text{PT}}$ has no direct consequence for the g -factor measurement but was characterized for completeness. To measure $B_{1,\text{PT}}$ the free cyclotron frequency is measured which characterizes the magnetic field through the relation $B = m/q\omega_c$. This is repeated for several offsets on one of the correction electrodes. Using the analytic description of the trap potential a change on the correction electrode can be related to a position change of the particle by $0.81 \mu\text{m mV}^{-1}$. The result of the $B_{1,\text{PT}}$ measurement is shown in figure 4.7 B and leads to $68.5(1.5) \mu\text{T mm}^{-1}$.

The quadratic term $B_{2,\text{PT}}$ was one of the major limitations of the previous g -factor measurement [48] due to its contribution to the linewidth. A reduction of this limitation was thus a primary task for the new experimental run. To reduce $B_{2,\text{PT}}$ the distance between both traps was increased by an additional transport electrode as shown in figure 4.7 A.

In order to characterize the field inhomogeneity after the modification the axial frequency in the presence of a non-zero $B_{2,\text{PT}}$ is considered and depends on the modified cyclotron energy

$$\Delta\nu_z = \frac{1}{4\pi^2 m \nu_z} \frac{B_{2,\text{PT}}}{B_{0,\text{PT}}} E_+ \quad (4.13)$$

see equation (2.28). Thus, thermal fluctuations in the modified cyclotron energy E_+ have a direct impact on axial stability. Furthermore, the stability of the axial frequency has a direct impact on the

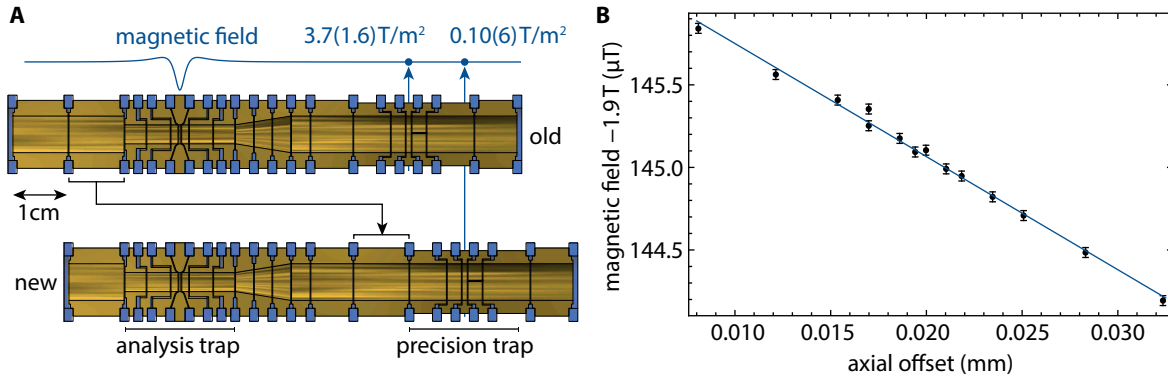


Fig. 4.7: (A) Optimization of the trap geometry to reduce the residual magnetic field inhomogeneity $B_{2,PT}$. The distance between AT and PT was increased by 1 cm with an additional transport electrode. This led to a reduction of 37(26) compared to the previous value. (B) Measurement of the free cyclotron frequency as a function of a potential offset. This can be related to a measurement of the magnetic field as a function of the axial position and characterizes $B_{1,PT}$.

modified cyclotron frequency measurement because it is measured with sideband coupling, section 2.6. Each time ν_+ is measured the modified cyclotron energy acquires a different fixed value on a Boltzmann distribution with expectation value $\langle E_+ \rangle = \frac{\nu_+}{\nu_z} k_B T_z$. This leads to an axial frequency shift

$$\Delta\nu_z = \frac{1}{4\pi^2 m \nu_z} \frac{B_{2,PT} T_z}{B_{0,PT}} \frac{\nu_+}{\nu_z} k_B \approx 8 \text{ mHz} \times B_{2,PT} T_z \quad (4.14)$$

parametrized by the product $B_{2,PT} T_z$. A small $B_{2,PT}$ is important for high stability and the associated narrow linewidth of the g -factor resonance. Furthermore, a small $B_{2,PT}$ also reduces the systematic shift on $\Delta\nu_+$ and $\Delta\nu_L$ which, however, cancel in the g -factor ratio to first order.

The product $B_{2,PT} T_z$ is measured by recording a series of axial frequency measurements with a $\nu_+ - \nu_z$ coupling drive in between. Each coupling drive changes the modified cyclotron energy according to a Boltzmann distribution

$$\rho_+(x) = \Theta(x) \frac{1}{\Delta\nu_z} \exp\left(-\frac{x}{\Delta\nu_z}\right). \quad (4.15)$$

This must be added to the normal distributed scatter of the axial frequency

$$\rho_z(y) = \frac{1}{\sqrt{2\pi} \sigma} \exp\left(-\frac{y^2}{2\sigma^2}\right). \quad (4.16)$$

The result is an asymmetric frequency distribution expressed by the convolution

$$\rho_+ * \rho_z = \frac{1}{2\Delta\nu_z} e^{-\frac{-2\Delta\nu_z x + \sigma^2}{2\Delta\nu_z^2}} \text{erf}\left(\frac{-\Delta\nu_z x + \sigma^2}{\sqrt{2}\Delta\nu_z \sigma}\right), \quad (4.17)$$

where erf is the error function. The asymmetry can be increased by raising the detector temperature with feedback. A characteristic measurement is shown in figure 4.8 A. The frequency distribution of

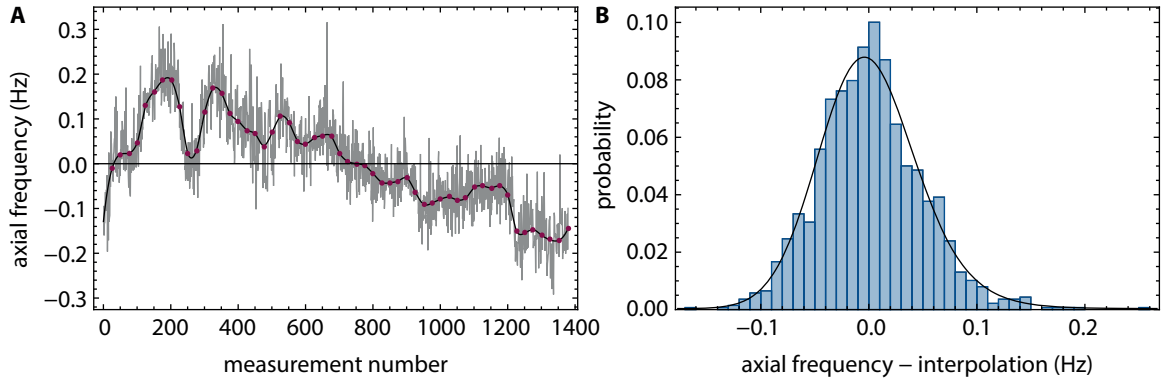


Fig. 4.8: (A) Sequence of axial frequency measurements with $\nu_+ - \nu_z$ sideband drives between each two measurements. The red dots represent the median value of the adjacent 50 measurements. The black line is an interpolation to third order. (B) Distribution of the axial frequency with value of interpolation subtracted. The asymmetry characterizes $B_{2,PT} T_z$.

interest is superimposed by a walk caused by temperature and pressure effects on the apparatus that cannot be easily avoided. To track the walk over time the median of 50 measurements is evaluated each 25 measurements. The resulting red points were interpolated to third order and yield the black background curve which can be subtracted from each individual measurement. The parameters of the resulting distribution $\rho_+ * \rho_z$ are determined by a maximum likelihood analysis. The evaluation process was tested with simulations to verify that the analysis procedure yields reliable results and does not, for example, depend on the bin size of the background determination.

Figure 4.8 B shows the histogram of the resulting frequency distribution with a feedback strength of $Q_1/Q_0 = 17500/6600$. The measurement was repeated with different feedback strengths for consistency. The final result is $B_2 T_z = 1.306(38) \text{ T m}^{-2} \text{ K}$. The second parameter $\sigma = 38.5(9) \text{ mHz}$ can be compared to an independent measurement of the axial frequency where no sideband was driven, $\sigma_{\text{ref}} = 40.5(2.6)$, which is in good agreement and independently justifies the analysis. The contribution to the overall cyclotron stability in equation (4.14) can now be calculated to be $\Delta\nu_z = 10 \text{ mHz}$. The stability of the cyclotron frequency is thus not limited by the thermal fluctuations in E_+ but by the stability of the axial frequency caused by thermal drifts, voltage instabilities and averaging. Based on a detector temperature of $T_z = 13.6(8.1) \text{ K}$ the result above corresponds to a residual magnetic field inhomogeneity of $B_{2,PT} = 0.10(6) \text{ T m}^{-2}$. This is a reduction by a factor of 37(26) compared to the previous experimental run [76].

External magnetic field fluctuations are another influence on the cyclotron frequency stability, namely short term fluctuations or sudden changes in the external field caused by cryo-filling or work in the lab. Therefore, a superconducting self-shielding coil [82] was wound around the trap chamber, its center aligned with respect to the precision trap's ring electrode. An SMD (Surface-Mounted Device) quench resistor placed on the superconducting wire is used to switch between active mode (superconducting) and non-active (quenched) mode. A heat dissipation with a power of $> 1.4 \text{ mW}$ is sufficient to obtain an immediate quench. The shielding factor of 69(1) was measured in a test setup

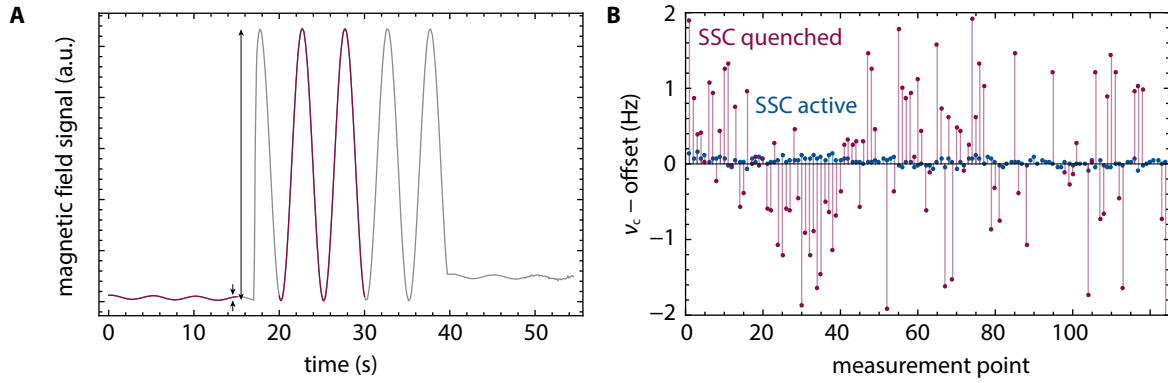


Fig. 4.9: (A) Test measurement of the shielding factor with external sinusoidal excitation. The gray line represents the measured data starting with an active coil which is then quenched. The red lines are fits that are used to obtain the shielding factor of 69(1). (B) Stability of the free cyclotron frequency with self-shielding coil active (blue) and quenched (red). Several red points are missing because the double dip was not sufficient for the fit to converge.

by comparing the amplitudes of an external sinusoidal magnetic field disturbance for both states.

Figure 4.9 B shows the performance in the actual experiment. The free cyclotron frequency was continuously measured for both the active and quenched coil. The active self-shielding coil has a tremendous impact and increases the stability by more than a factor of 10. The exact number cannot be calculated because many double dip spectra are not sufficient for the fitting routine to converge and the free cyclotron frequency cannot be determined properly. This is indicated by the missing red points in the figure.

Continuous logging of the cyclotron frequency similar to the blue data over a few days allows the assignment of the long term drift stability

$$\frac{1}{t} \frac{\Delta \nu_c}{\nu_c} = 2.9(3) \times 10^{-9} \text{ h}^{-1} . \quad (4.18)$$

This value is comparable with, for example, the superconducting magnet at the antiproton g -factor experiment at CERN with $3.2(4) \times 10^{-9} \text{ h}^{-1}$. Such slow drifts constitute no limitation for a 300 ppt g -factor measurement since measurements are typically performed on a minute timescale and ν_L and ν_c are measured in parallel, for details see section 7. One reason for these drifts, among others, is the stress on the horizontal setup as a function of the cryo-liquid fill levels. The variation in the weight of the cryostat induces small movements of the trap chamber in the magnetic field which leads to a drift in the cyclotron frequency.

The overall free cyclotron stability is shown in figure 4.10. The previous apparatus from 2014 enabled a measurement with 3.3 ppb fractional precision based on a cyclotron stability of ~ 400 mHz. The developments presented in this work made it possible to improve the stability by an order of magnitude to ~ 40 mHz and ultimately allowed a g -factor measurement in the sub-ppb regime. In contrast to 2014 the stability is not limited by the influence of $B_{2,PT}$ anymore but by the axial stability which is at ~ 40 mHz. A further reduction either requires the direct measurement of the modified

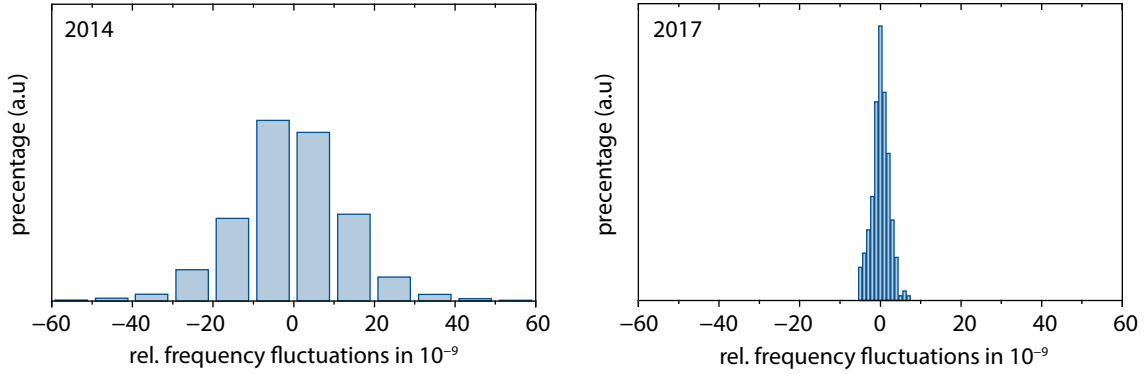


Fig. 4.10: Comparison of the cyclotron frequency stability from 2014 and the current experiment. The new stability allows for sub-ppb measurements. The improvement was mainly achieved by optimizing the trap geometry and by the implantation of a self-shielding coil. The cyclotron frequency determination is limited by axial frequency stability.

cyclotron frequency with the phase method, see section 9.2, or an improved axial stability by an increased averaging time and a further stabilized high-precision voltage source.

4.6 Frequency fitting

4.6.1 Analytic model

To calculate the line shape of the dip spectrum with resonator the lumped circuit model is used [62]. The particle is modeled as a series tuned RLC circuit in and the resonator as a parallel tuned RLC circuit. The impedance of particle and resonator in parallel is given by

$$Z(\omega) = \left(\frac{1}{\frac{1}{i\omega c_1} + i\omega l_1 + r_1} + i\omega C_0 + \frac{1}{i\omega L_0} + \frac{1}{R_0} \right)^{-1}, \quad (4.19)$$

where C_0 , L_0 and R_0 are defined by the resonator, and l_1 , c_1 and r_1 by the particle. The corresponding Johnson-Nyquist noise is defined by

$$u_n = \sqrt{4k_B T \Delta\nu \operatorname{Re}[Z]} \quad (4.20)$$

with the real part of the impedance as the resistive component. To simplify the expression the substitution

$$C_0 \rightarrow \frac{1}{\omega_0^2 L_0} \quad c_1 \rightarrow \frac{1}{\omega_1^2 l_1} \quad (4.21)$$

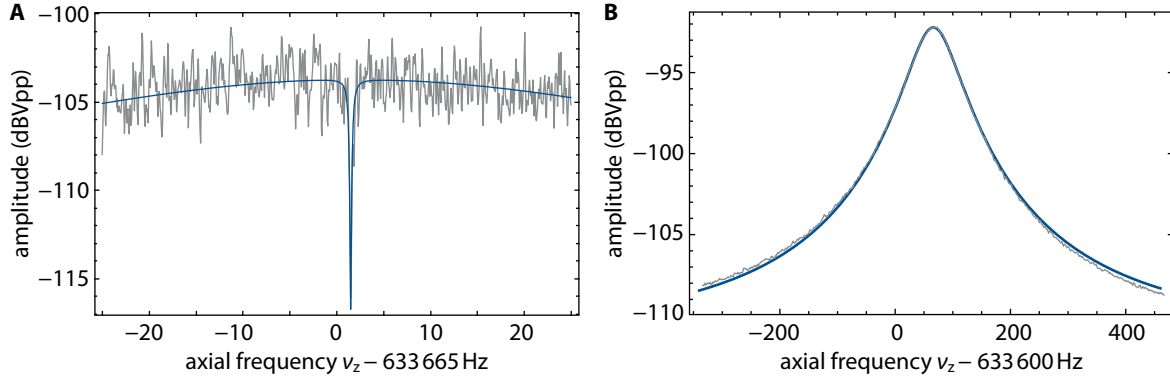


Fig. 4.11: (A) Full dip model in comparison to a measurement spectrum. (B) Resonator model compared to a measurement spectrum. A small deviation can be seen on the edges due to an asymmetry that is not included in the model.

with ω_0 the resonator frequency and ω_1 the particle frequency is used. The real part finally reads

$$\begin{aligned} \text{Re}[Z] &= \frac{A}{B + C + D} & (4.22) \\ A &= L_0^2 R_0 \omega^2 \omega_0^4 (R_0 r_1 \omega^2 + r_1^2 \omega^2 + l_1^2 (\omega^2 - \omega_1^2)^2) \\ B &= 2L_0^2 R_0 r_1 \omega^4 \omega_0^4 \\ C &= L_0^2 \omega^2 \omega_0^4 (r_1^2 \omega^2 + l_1^2 (\omega^2 - \omega_1^2)^2) \\ D &= R_0^2 \left(r_1^2 (\omega^3 - \omega \omega_0^2)^2 + (L_0 \omega^2 \omega_0^2 - l_1 (\omega^2 - \omega_0^2) (\omega^2 - \omega_1^2))^2 \right) . \end{aligned}$$

Expressed with the Johnson-Nyquist noise on a logarithmic scale

$$u_{\log} = 10 \log \left[\left(\frac{u_n}{1 \text{ V}} \right)^2 \right] = 20 \log \left[\sqrt{4k_B T \Delta\nu \text{Re}[Z]} \right] \quad (4.23)$$

the lineshape can be fit to a real dip spectrum as shown in figure 4.11 A and to a resonator spectrum, figure 4.11 B . The resonator model shows a small discrepancy on the edges due to a small asymmetry in the background.

To account for the real background a heuristic approach is used and the real part of the impedance is substituted by

$$\text{Re}[Z'] = A_0 \cdot \text{Re}[Z] + B_0 + C_0 (\omega - \omega_0) , \quad (4.24)$$

where A_0 accounts for the amplitude, or an offset on a logarithmic scale, and does not affect the shape of the resonator or the fit. B_0 is used to introduce background noise for example by the amplifier and C_0 is an asymmetry parameter to match real-world spectra. The analytic model can now be used to analyze the robustness of the fitting algorithm, which will be introduced in the next section.

4.6.2 Fit algorithm

To understand the fit algorithm a brief introduction to the fit model parameters is necessary. Only the single dip will be discussed but the same arguments apply to double dip. The description of the

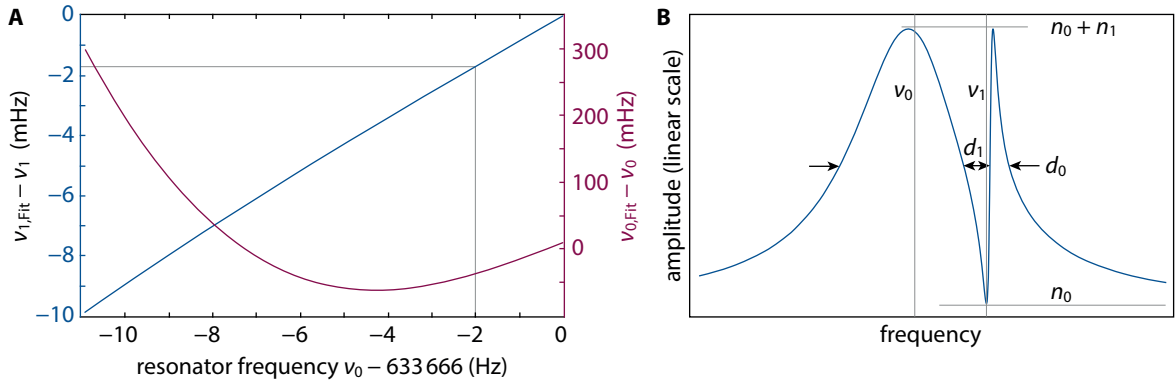


Fig. 4.12: (A) The systematic deviation between fitted frequency (blue) $\nu_{1,Fit}$ and real frequency ν_1 increases the further the resonator frequency ν_0 is detuned from the particle frequency $\nu_1 = 633\,666$ Hz. The same is true for the predicted resonator frequency (red) $\nu_{0,Fit}$ which is, however, less critical since it is no input parameter for the g factor. (B) Parameters of the fit model, for further details refer to text.

single dip is based on a simplified lineshape model

$$\rho(\nu) = n_0 + \frac{4(\nu - \nu_1)^2 n_1}{d_1^2 \left(\frac{4(\nu - \nu_1)^2}{d_1^2} + \left(1 + \frac{4(\nu - \nu_0)(\nu - \nu_1)}{d_0 d_1} \right)^2 \right)} \quad (4.25)$$

on a linear scale as shown in figure 4.12 B. Offset and signal-to-noise ratio are defined by n_0 and n_1 . The dip width and frequency are governed by d_1 and ν_1 and in case of the resonator with d_0 and ν_0 . In this simplified model the dip always shorts the resonator perfectly, which means that the resonator background n_0 is at the same level as the dip minimum. Typically, this is not realized in the experiment and introduces limitations for the fit algorithm. Another question is, how well the parameters approximate the real values for a spectrum as shown in figure 4.11 A where only limited information of the resonator is included in the spectrum. A well-defined resonator frequency ν_0 can often not be guaranteed for small frequency spans because the resonator is almost flat and noisy.

To analyze the limitations systematically, dips that match the experimental spectra in the precision trap are simulated with the full analytic model in equation (4.24). The particle frequency is fixed at $\nu_1 = 633\,666$ Hz and defines the dip position. A slight asymmetry is chosen defined by C_0 to match the experimental background. The span is set to 50 Hz and the S/N is chosen to be around 6 dB. The simulated input parameter for the resonator frequency is then varied from $\nu_0 = 633656$ Hz to 633666 Hz. Each simulated spectrum is fit with the simplified model and the output parameters of the fit algorithm are compared to the input parameters of the simulation. Figure 4.12 A shows the deviation of $\nu_{0,fit}$ and $\nu_{1,fit}$ from the real input frequencies. The deviations vanish if the particle frequency matches the resonator frequency. The results scale only weakly with typical asymmetries C_0 and this presents no limitation for typical experimental asymmetric backgrounds.

Figure 4.12 A has important consequences for the g -factor measurement. If the particle is centered with respect to the resonator frequency within an uncertainty of 2 Hz, the deviation of the axial frequency is smaller than 1.8 mHz which corresponds to $< 10^{-10}$ ppb shift. If the S/N is changed to

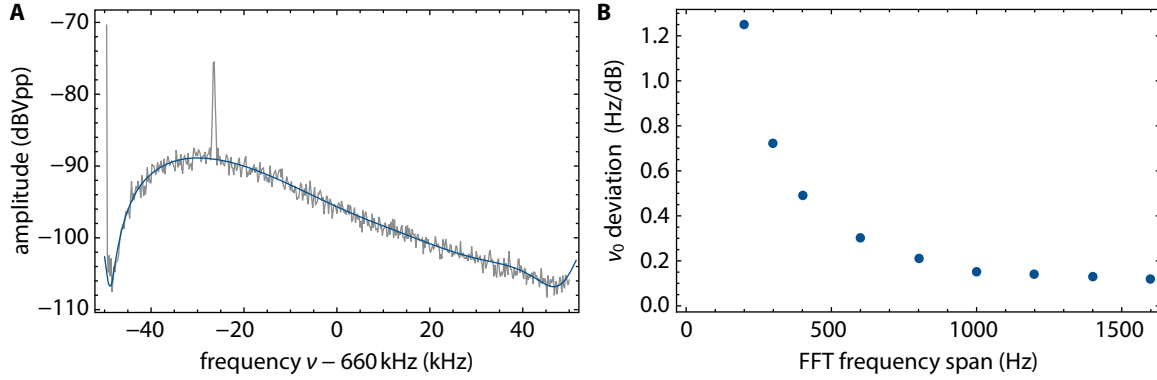


Fig. 4.13: (A) Background noise on the spectrum analyzer around the PT resonator peak. (B) Deviation of the fitted resonator frequency and the real resonator frequency ν_0 as a function of the FFT span. The deviation scales linearly to first order with asymmetry.

around 4 dB this changes to 2 mHz.

In conclusion, it is highly important to determine the real resonant frequency of the detection system with high precision and center the particle dip with respect to this frequency. This ensures that the fit leads to robust results that do not limit the frequency determination on the 100 ppt level. Here, all parameters of the fit are varied for the optimization. It is also possible to use the real resonator frequency, determined by a reference spectrum, as input and keep ν_0 fixed during the fit. This is discussed in the next section.

4.6.3 Determination of the resonator frequency

Ideally, the resonator would be completely symmetric and finding the resonator frequency would be straight-forward. However, an experimental spectrum has an asymmetric background which must be taken into account. Resonator spectra are simulated which match the experimental conditions. As a starting point, a large spectrum of the resonator with background was measured with a spectrum analyzer and is shown in figure 4.13 A. The blue line is a heuristic fit with a series $g(\nu) = \sum_{i=-5}^5 a_i \nu^i$. Around the resonator peak a Taylor series up to second order is sufficient to describe the background. The analytic model of the resonator is derived the same way as the complete dip model before

$$\text{Re}[Z_{\text{res}}] = \frac{1}{\frac{1}{R_0} + \frac{1}{L_0^2} \left(\frac{1}{\omega^2} - \frac{1}{\omega_0^2} \right)^2} . \quad (4.26)$$

Combined with the background this leads to the model for the resonator

$$\text{Re}[Z'_{\text{res}}] = A_0 \cdot \text{Re}[Z_{\text{res}}] + B_0 + C_0(\omega - \omega_0) + D_0(\omega - \omega_0)^2 . \quad (4.27)$$

Asymmetric PT spectra without white noise are generated for different frequency spans. Afterward, the deviation of the fit resonator frequency from the real resonator frequency is calculated for different asymmetries. The asymmetry is characterized in dB by the difference between the first frequency

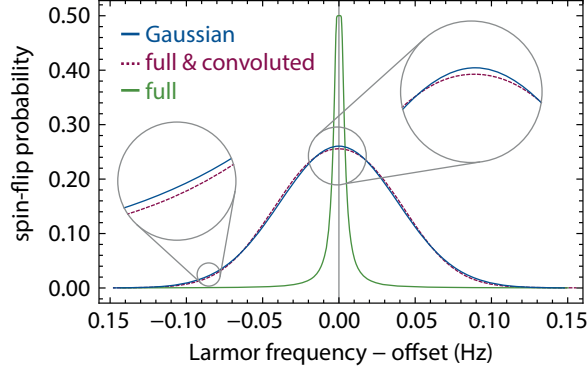


Fig. 4.14: Comparison between the full theoretical model for the lineshape (red) and the Gaussian approximation (blue). The full solution of the lineshape without convolution is shown in green.

point (left side of the spectrum) and the last frequency point (right side of the spectrum). The deviation between input and output resonator frequency is shown in figure 4.13 as a function of the used frequency span for the spectrum. A reference spectrum of 800 Hz is suitable to determine the resonator frequency well below 1 Hz.

In the final g -factor routine several reference spectra of the resonator were recorded during each cycle to continuously track the frequency ν_0 of the resonator. The resonator frequency was then used as a fixed input parameter during the fits of the dip spectra. The result with fixed parameter ν_0 is compared to the free parameter case during the fit in detail in chapter 7.

4.7 Line shape of the g -factor resonance

A detailed understanding of the lineshape in an inhomogeneous magnetic field is essential for the measurement of the g -factor and depends on the trap characteristics such as the detector. The g -factor lineshape has been discussed in great detail in [79]. To derive the lineshape in the precision trap the results are briefly discussed within this section.

In an inhomogeneous magnetic field $B = B_{0,PT} + B_{2,PT} z^2$ along the axial direction the particle's Larmor frequency depends on the axial energy $E_z = \frac{1}{2} m \omega_z^2 r_z^2$, or equivalently on the position. Due to the axial motion a modulation of the Larmor frequency occurs with

$$\omega_L(t) = \omega_{L,0} \left(1 + \frac{B_{2,PT}}{B_{0,PT}} z(t)^2 \right) . \quad (4.28)$$

Averaged over time $\langle z(t)^2 \rangle = r_z^2/2$ the change of the Larmor frequency $\Delta\omega_L$, the *linewidth parameter*, can be expressed as

$$\Delta\omega_L = \omega_L \frac{B_{2,PT}}{2B_{0,PT}} r_z^2 \Big|_{r_z^2 = \frac{k_B T_z}{m\omega_z^2}} \approx 0.09 \text{ Hz} . \quad (4.29)$$

This parameter is compared to the coupling between the particle and the axial detector

$$\gamma = \frac{1}{\tau_z} = \frac{R_{\text{eff}}}{m} \left(\frac{q}{D_z} \right)^2 \Big|_{R_{\text{eff}}=Q_z \omega_z L_z} \approx 2.24 \text{ Hz} . \quad (4.30)$$

For the case $\gamma \gg \Delta\omega$ the axial motion is *strongly coupled* to the thermal bath which is one of the two limits where the line profile can be evaluated as a simple function. The lineshape can be expressed as a Lorentzian profile

$$\chi(\omega) = \frac{1}{\pi} \frac{\frac{\Delta\omega_L^2}{\gamma}}{(\omega - \omega_L - \Delta\omega_L)^2 + \left(\frac{\Delta\omega_L^2}{\gamma} \right)^2} \quad (4.31)$$

that is shifted by $\Delta\omega$. This shift also affects the free cyclotron frequency and, to first order, cancels during the g -factor measurement. To account for the cyclotron frequency instability the lineshape is convoluted with a normal distribution $N(0, \sigma)$, where the width σ is given by the frequency stability. Finally, the convoluted lineshape $\chi_L = \chi * N(0, \sigma)$, a Voigt profile, is used to express the spin-flip probability as a function of the applied drive frequency

$$\mathcal{P}(t_{\text{exc}}, \chi_L) = \frac{1}{2} \left(1 - \exp \left[-\frac{1}{2} \omega_R^2 t_{\text{exc}} \chi_L(\omega) \right] \right) \quad (4.32)$$

with excitation time $t_{\text{exc}} = 120 \text{ s}$ and Rabi frequency ω_R . The full lineshape is approximated with a normal distribution as shown in figure 4.14, in comparison to the full analytic solution [79]. Deviations in the expectation value, e.g. due to a slight asymmetry of the full solution, are more than one order of magnitude smaller than the experimental error. Furthermore, the discrepancy between both lineshapes at the top and on the sides is beyond the experimental resolution. For more details refer to the g -factor evaluation in chapter 7.

Chapter 5

First Steps in phase space

The idea to measure the phase of a particle's motion to determine the g factor of a bound electron was introduced by S. Stahl [83]. The detection of spin flips demands resolving tiny frequency changes $\Delta\nu_{z,\text{SF}}$ which can be tracked by measuring the phase of the motion rather than the frequency. Typically, such a phase measurement is about one order of magnitude faster which increases the range of modified cyclotron energies that can be accepted to detect spin flips in the analysis trap. In consequence, shorter experimental cycle times can potentially be reached. The first part of this chapter discusses the theoretical concepts of the phase method, whereas the second part focuses on experimental results.

5.1 Phase method

Figure 5.1 shows the basic principle of a phase sensitive measurement. First, the axial motion is excited with a frequency close to the expected axial frequency $\nu_{\text{rf}} \approx \nu_z$. This excitation imprints a defined but unknown phase. Next, the phase evolves with the true axial frequency for a time t_{evol} . During the evolution time the detector is detuned with negative feedback to reduce the decay time of the particle motion. Finally, the detector is brought into resonance again and the peak in the spectrum is read out to extract the phase information with a fast Fourier transformation. A change in the axial frequency $\Delta\nu_z$ results in a phase change

$$\Delta\varphi = 2\pi \Delta\nu_z t_{\text{evol}} \quad (5.1)$$

and scales with the evolution time. To obtain a large phase difference the choice of longer evolution time is beneficial but requires a coherent evolution for a greater amount of time. In case of a spin flip with $\Delta\nu_{z,\text{SF}} = 172 \text{ mHz}$ a phase change of $\Delta\varphi = 62^\circ \text{ s}^{-1}$ must be resolved and the single readout error must be well below $\Delta\varphi$. The following sections will discuss various parameters that must be optimized to achieve small single phase readout errors.

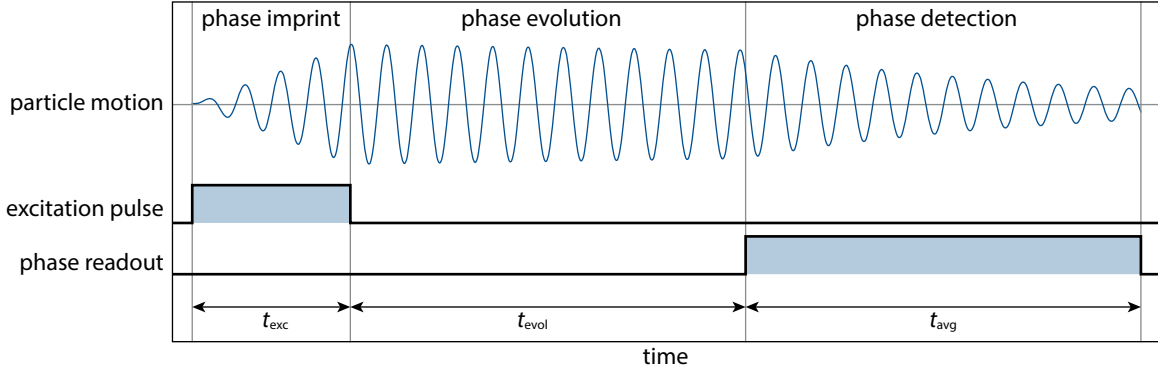


Fig. 5.1: Measurement principle of the phase method. During the phase imprint the amplitude increases due to the excitation pulse. The particle is then decoupled from the resonator and evolves for the time t_{evol} . Finally, the resonator is brought into resonance again, a decaying peak signal is observed, and the phase read out during t_{avg} .

5.1.1 Phase stability as function of S/N

One apparent parameter to achieve a high phase resolution in measurements is the signal-to-noise ratio, the level between excited proton peak and noise floor of the resonator. To calculate the dependence of the phase stability as a function of S/N the phase space is considered generated by the coordinates x and $\dot{x}/\omega = v/\omega$, compare figure 5.2 A. The particle moves on a circle around the origin described by the vector $\rho \equiv (x, -v/\omega)$ where the length is defined by

$$\rho \equiv |\rho| = \sqrt{\frac{2E}{m\omega^2}} \quad (5.2)$$

which is the same as the axes vertices

$$\hat{x} \equiv \sqrt{\frac{2E}{m\omega^2}} \quad \text{and} \quad \hat{v}/\omega \equiv \sqrt{\frac{2E}{m\omega^2}}, \quad (5.3)$$

as a result of $E_{\text{total}} = \frac{1}{2}m\omega^2\hat{x}^2 = \frac{1}{2}m\hat{v}^2 = \frac{1}{2}m\omega^2\rho^2$.

The vector can be described in polar coordinates by (ρ, φ) with a probability distribution assigned to each. The angular component φ is evenly distributed in the interval $[0, 2\pi)$ since no angle can be preferred due to noise. For the radial component the energy distribution is given by

$$f(E) = \frac{1}{E_0} e^{-E/E_0} dE. \quad (5.4)$$

Substituting $E = \frac{1}{2}m\omega^2\rho^2$ and adding the angular dependence leads to

$$f(\rho, \varphi) = 2\lambda\rho e^{-\lambda\rho^2} d\rho \frac{d\varphi}{2\pi} \quad \text{with} \quad \lambda = \frac{m\omega^2}{2E_0}. \quad (5.5)$$

This result can also be obtained by considering the covered area in the phase diagram. It is proportional to the Boltzmann distributed energy. In the case above the circle has an area proportional to ρ^2 and thus ρ^2 must be Boltzmann distributed or ρ like equation (5.5).

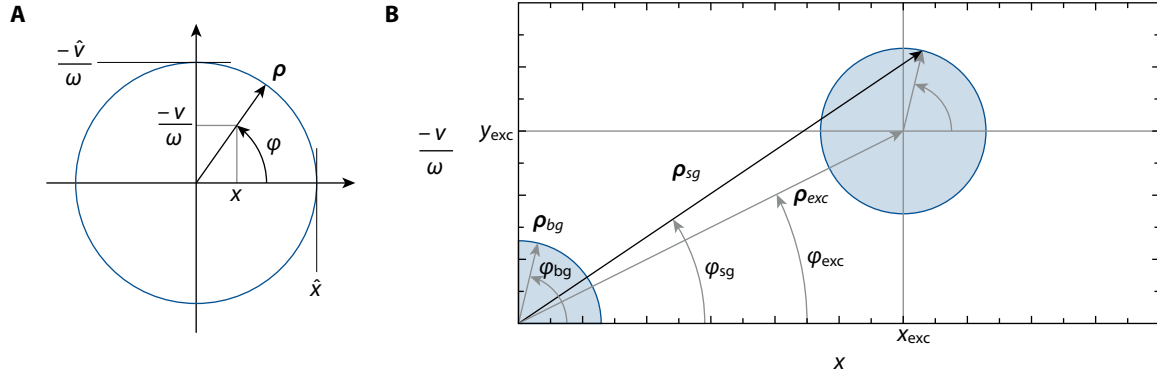


Fig. 5.2: (A) Phase space diagram (B) Particle in phase space after excitation for S/N calculation.

To calculate the phase stability as a function of the S/N Figure 5.2 B is considered [58, 84, 85]. The blue circle describes the phase scatter due to interaction of the particle with the resistive detection system at temperature T_z . The particle is excited to an amplitude $|\rho_{exc}|$ and the phase of the resulting signal is measured. However, the measured phase of the signal φ_{sg} differs from the ideal phase φ_{exc} due to the excitation pulse because the random phase of the noise floor adds to amplitude and phase ($\rho_{sg} = \rho_{bg} + \rho_{exc}$).

To derive the phase stability the shifted two dimensional probability density $f(\rho, \varphi, \rho_{exc})$ is required, that describes the probability to find a particle at any given point (ρ, φ) assuming that the energy is Boltzmann distributed. The solution is given by shifting equation (5.5) to $\rho_{exc} = (x_{exc}, y_{exc})$. For that purpose the polar coordinates are changed to Cartesian coordinates using the determinant of the Jacobian matrix $dx dy = \rho d\rho d\varphi$ and the usual transformation $(x, y) = (\rho \cos \varphi, \rho \sin \varphi)$

$$f(\rho, \varphi) = \frac{\lambda}{\pi} \rho e^{-\lambda \rho^2} d\rho d\varphi = \frac{\lambda}{\pi} e^{-\lambda(x^2+y^2)} dx dy = f(x, y) . \quad (5.6)$$

This result can now be shifted by (x_{exc}, y_{exc}) and translated back to polar coordinates

$$f(x - x_{exc}, y - y_{exc}) = \frac{\lambda}{\pi} e^{-\lambda((x-y_{exc})^2+(y-y_{exc})^2)} dx dy \quad (5.7)$$

$$= \rho \frac{\lambda}{\pi} e^{-\lambda((\rho \cos(\varphi)-x_{exc})^2+(\rho \sin(\varphi)-y_{exc})^2)} d\rho d\varphi = f(\rho, \varphi, \rho_{exc}) . \quad (5.8)$$

An integration over the complete phase space Ω shows that

$$\int_{\Omega} dA f(\rho, \varphi, \rho_{exc}) = \int_0^{\infty} d\rho \int_{-\pi}^{\pi} d\varphi f(\rho, \varphi, \rho_{exc}) = 1 . \quad (5.9)$$

The radius of the blue circle in Figure 5.2 B describes the average amplitude of the particle due to the energy distribution. It can be determined analytically in case of no offset by calculating the expectation value

$$|\rho_{bg}| = \int_{\Omega} dA f(\rho, \varphi, \mathbf{0}) \rho = \frac{1}{2} \sqrt{\frac{\pi}{\lambda}} \quad (5.10)$$

and similar in case with offset for the resulting signal (only numerically)

$$|\rho_{sg}| = \int_{\Omega} dA f(\rho, \varphi, \rho_{exc}) \rho . \quad (5.11)$$

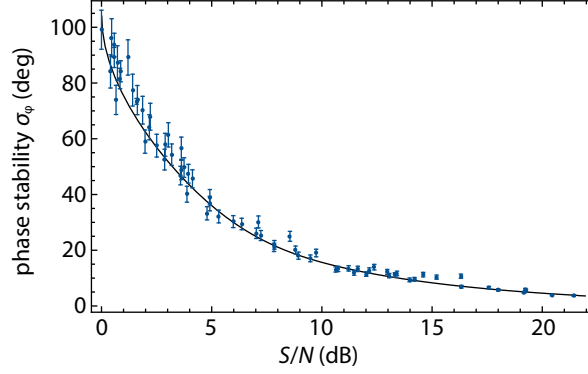


Fig. 5.3: Calculated phase stability as a function of the signal-to-noise ratio, prediction and measured data.

The S/N in decibel is defined as

$$S/N_{\log}(\rho_{\text{exc}}) = 20 \log \left(\frac{|\rho_{\text{sg}}|}{|\rho_{\text{bg}}|} \right) \quad (5.12)$$

and can now be calculated for any offset $(x_{\text{exc}}, y_{\text{exc}})$. The actual phase stability for successive measurements at the same excitation strength is given by the standard deviation

$$\sigma_{\varphi}(\rho_{\text{exc}}) = \sqrt{\int_{\Omega} dA f(\rho, \varphi, \rho_{\text{exc}}) (\varphi - \varphi_{\text{exc}})^2} \quad (5.13)$$

Equation (5.12) for the x -axis and (5.13) for the y -axis are combined to obtain Figure 5.3. The theoretical prediction is indicated as the solid black line. The experimental data where the phase stability was measured as a function of the signal-to-noise ratio is in good agreement with the expectation.

It can be instructive to consider the limit of σ_{φ} for 0 dB signal-to-noise. The noise circle is then exactly centered around the origin and no phase information is contained anymore

$$\lim_{\rho_{\text{exc}} \rightarrow 0} \sigma_{\varphi}(\rho_{\text{exc}}) \approx 103.923^{\circ} \quad (5.14)$$

This is the same result as the standard deviation of a uniform distributed interval $[0, 2\pi)$ given by

$$\tilde{\sigma}_{\varphi} = \sqrt{\frac{2\pi - 0}{12}} \approx 103.923^{\circ} \quad (5.15)$$

or in other words maximum uncertainty.

5.1.2 Optimization of the averaging time

The excited particle cools due to the interaction with the detector. As a result an exponentially decaying signal is measured. The chosen averaging time of the FFT has a large influence on the measured S/N and thus on the phase stability. For short FFT times the white noise still limits the stability while for long FFT times the signal has already decayed and only noise is measured. In order to incorporate the averaging time behavior the S/N is analytically derived for a decaying signal, following arguments in [58].

The voltage signal due to the excited particle is

$$U = R_{\text{eff}} I . \quad (5.16)$$

The current is expressed by

$$I = \frac{q}{D_z} \dot{z} \quad (5.17)$$

as introduced earlier. Using effective values this equation can be written as

$$I = \frac{1}{\sqrt{2}} \frac{q}{D_z} v_z = \frac{1}{\sqrt{2}} \frac{q}{D_z} \omega_z r_z = \frac{q}{D_z} \sqrt{\frac{E_z}{m}} , \quad (5.18)$$

where $E_z = \frac{1}{2} m \omega_z^2 r_z^2$ was used in the last step. In case of an excited particle that cools down to thermal equilibrium an exponential decay must be added to the equation resulting in $I \cdot e^{-t/\tau}$. Furthermore, the signal is averaged for the time t_{FFT} which leads to

$$\bar{U} = R_{\text{eff}} \frac{q}{D_z} \sqrt{\frac{E_z}{m}} \left(\frac{1}{t_{\text{FFT}}} \int_0^{t_{\text{FFT}}} e^{-t/\tau} dt \right) \quad (5.19)$$

$$= R_{\text{eff}} \frac{q}{D_{\text{eff}}} \sqrt{\frac{E_z}{m}} \frac{\tau}{t_{\text{FFT}}} \left(1 - e^{-t_{\text{FFT}}/\tau} \right) . \quad (5.20)$$

The signal-to-noise ratio is defined as

$$S/N = \frac{\sqrt{(R_{\text{eff}} I)^2 + \sum e_n^2}}{\sqrt{\sum e_n^2}} , \quad (5.21)$$

where the numerator takes into account that the signal is always the real signal together with the noise sources e_n . This subtlety becomes especially important when working with very low S/N . On a logarithmic scale the S/N , as defined here, has an effective range of $[0, \infty)$. Based on the input noise of the amplifier the Johnson-Nyquist noise reads

$$e_n = \sqrt{4k_B T R_{\text{in}} \Delta\nu} \Big|_{\Delta\nu=(t_{\text{FFT}})^{-1}} \sim \frac{A_0}{\sqrt{t_{\text{FFT}}}} \quad (5.22)$$

which scales with the square root of the FFT time. Combined with the signal this leads to

$$S/N_{\log}(t_{\text{FFT}}) = 20 \log \left(\frac{\sqrt{(B_0/t_{\text{FFT}} (1 - e^{-t_{\text{FFT}}/\tau}))^2 + (A_0/\sqrt{t_{\text{FFT}}})^2}}{A_0/\sqrt{t_{\text{FFT}}}} \right) \quad (5.23)$$

with scale parameters A_0 and B_0 . To test the theoretical prediction the phase stability was measured as a function of the FFT averaging time with an exponentially decaying signal ($\tau = 250$ ms) generated by a function generator. The measured signal-to-noise ratio is shown in figure 5.4 B. Based on the S/N the expected phase stability can be calculated. The result is shown in Figure 5.4 A with the expected behavior as the solid black line. Data and expectation are in good agreement. The ideal averaging time is found for roughly $t_{\text{avg}} \sim \tau$.

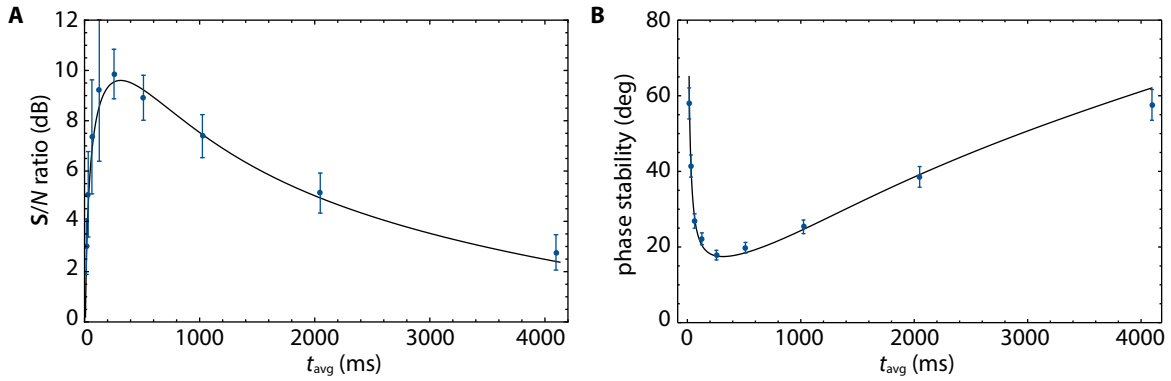


Fig. 5.4: (A) The measured S/N as function of the FFT averaging time. (B) Phase stability as a function of the FFT averaging time. The black line is a fit with the expected behavior. The blue data points were measured with an FFT and a decaying signal with time constant of 250 ms.

5.1.3 Fourier vs Laplace transform

So far only the Fourier transform \mathcal{F} was considered to determine the phase, however, also the two-sided Laplace transform \mathcal{B} (bilateral Laplace transform) is suitable. Fourier and two-sided Laplace transform are connected by

$$\begin{aligned}
 \mathcal{B}\{f(t)\} &= \int_{-\infty}^{\infty} f(t)e^{-st} dt \quad s \in \mathbb{C} \\
 &= \int_{-\infty}^{\infty} f(t)e^{-(\sigma+i\omega)t} dt \\
 &= \int_{-\infty}^{\infty} (f(t)e^{-\sigma t}) e^{-i\omega t} dt \\
 &= \sqrt{2\pi} \mathcal{F}\{f(t)e^{-\sigma t}\} \quad \sigma \in \mathbb{R}
 \end{aligned} \tag{5.24}$$

which means that taking the two-sided Laplace transform is basically as taking the Fourier transform of a by $e^{-\sigma t}$ scaled version of the original function. The scaling with $e^{-\sigma t}$ can also be understood as a weighting of the original time data where for $\sigma > 0$ early data has a higher weight while later data is suppressed. For the decaying particle signal this is advantageous. In case of the FFT it was found that the ideal averaging time is close to the decay time of the particle. Averaging for longer times does not increase the S/N anymore since more and more noise is added and outweighs additional signal information. The idea of weighting the data allows to use this additional information by averaging longer without losing S/N .

To test this a simulation was made that generates time data of a decaying sinus with defined phase and noise. For each data set a Fourier transform was performed. In addition the data was multiplied by a factor of $e^{-t/t_{\text{decay}}}$ and then Fourier transformed. Figure 5.5 A shows the result of the Laplace transform for different t_{decay} times. The minimum is found for $t_{\text{decay}} = \tau$. For $t_{\text{decay}} \rightarrow \infty$ the phase stability converges against the value of the Fourier transform.

Figure 5.5 B shows a direct comparison between Laplace and Fourier transform. The amplitude

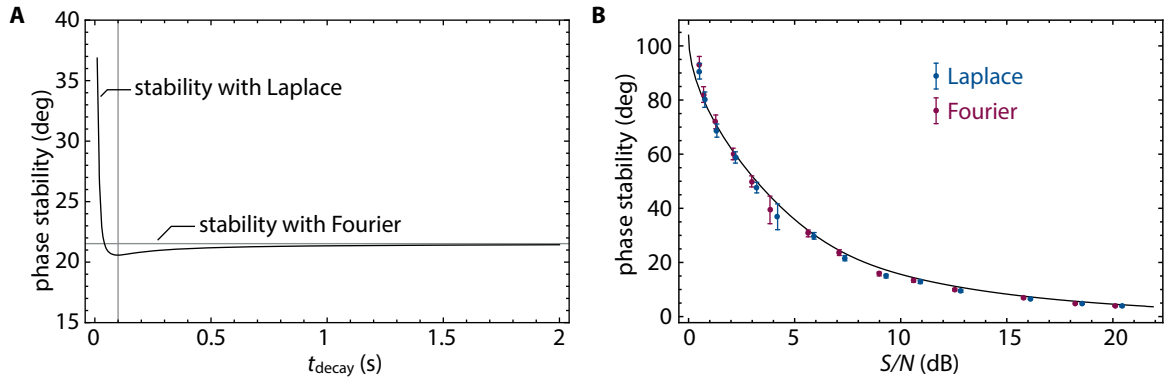


Fig. 5.5: (A) A numeric simulation is used to generate time data of a decaying signal ($\tau = 100$ ms). The phase stability is calculated for different decay estimates t_{decay} in the Laplace transformation. Ideal stability is achieved when the real decay time matches the decay time in the Laplace transformation. For large decay time estimates the phase stability converges against the Fourier phase stability (B) Comparison between Laplace and Fourier transform. The averaging time is set to the decay time which is ideal for the Fourier transform. The decay estimate is also set to the decay time which is ideal for the Laplace transform. It can be seen that for identical transients the Laplace transform results in a higher S/N and thus in a higher phase stability. Both methods are consistent with the theoretical expectation.

of the simulated signal was varied and the ideal phase stability for the Fourier and for the Laplace transform were calculated. As expected the S/N is slightly higher with the Laplace transform due to the noise suppression and thus the phase stability is slightly better.

Even at the ideal averaging time of the Fourier transform the Laplace transform is already advantageous. However, the Laplace transform allows also to average for even longer times without losing phase stability. Instead of speaking about phase stability it is equivalent to discuss the S/N. In the next part the analytic expressions shall be discussed for a detailed understanding of the averaging process.

Similar to the Fourier case an analytical expression can be derived for the Laplace where the data is scaled by $e^{-t/t_{\text{decay}}}$. The scaling of the noise changes to

$$\begin{aligned}
 u_n &\sim \frac{1}{t_{\text{FFT}}} \int_0^{t_{\text{FFT}}} \frac{1}{\sqrt{t}} e^{-t/t_{\text{decay}}} dt \\
 &\sim \frac{A_0}{t_{\text{FFT}}} \text{erf}(B_0 \sqrt{t_{\text{FFT}}}) ,
 \end{aligned} \tag{5.25}$$

where $\text{erf}(x)$ is the error function. This leads to the modified function

$$S/N = \frac{\sqrt{\left(\frac{C_0}{t_{\text{FFT}}} \int_0^{t_{\text{FFT}}} e^{-t/\tau} e^{-t/\tau} dt \right)^2 + \left(\frac{A_0}{t_{\text{FFT}}} \text{erf}(B_0 \sqrt{t_{\text{FFT}}}) \right)^2}}{\left(\frac{A_0}{t_{\text{FFT}}} \text{erf}(B_0 \sqrt{t_{\text{FFT}}}) \right)} . \tag{5.26}$$

Using the fit parameter A_0, B_0 and C_0 the behavior can be described precisely as shown in Figure 5.6 A and B. Here signal (numerator) and noise level (denominator) are plotted separately. Finally, the individual parts can be combined to obtain the signal-to-noise ratio as a function of the averaging

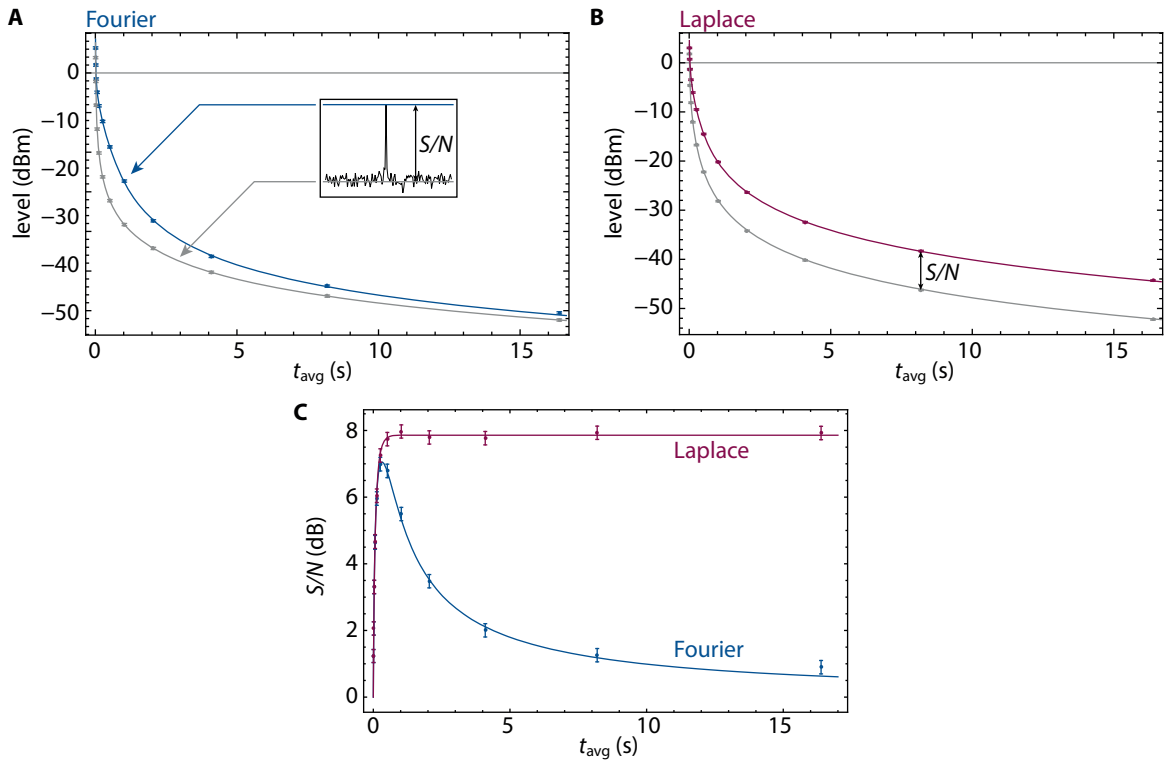


Fig. 5.6: (A) Signal (blue) and noise (gray) level evaluated with a Fourier transform as a function of the averaging time. (B) Signal (red) and noise (gray) level evaluated with a Laplace transform as a function of the averaging time. (C) Comparison of the S/N based on the Fourier and Laplace analysis. The Laplace transformation converges against a fixed value for long averaging times.

time for the Fourier and the Laplace case. Figure 5.6C shows that the Fourier transform loses for long averaging time while the Laplace transform converges against a finite value that is better than the best value of the Fourier case.

In practice the Laplace transformation allows to “squeeze out” a little more information but should be seen as fine tuning if other parameters are already rather well optimized. The Laplace equation requires to record the whole time signal for each averaging and perform the processing separately. The Fourier transform, on the other hand, is a built-in function and the phase can be analyzed with e.g. an *SRS SR1 Audio Analyzer* directly.

5.1.4 Bleeding and zero padding

Any experimentally determined time signal is recorded with a certain sample number n for a specific time $t_{\text{avg}} \equiv \Delta t$. This leads to discrete time steps $dt = \frac{\Delta t}{n}$. In the frequency spectrum a frequency range of $\Delta\nu = \frac{n}{\Delta t}$ is governed with frequency intervals $d\nu = \frac{1}{\Delta t}$. The maximum frequency that can be sampled is the Nyquist frequency $\nu_{\text{max}} = \frac{\Delta\nu}{2} = \frac{n}{2\Delta t}$. The phase method, as described above, relies on a signal within one bin where phase and amplitude are calculated. However, due to the discrete

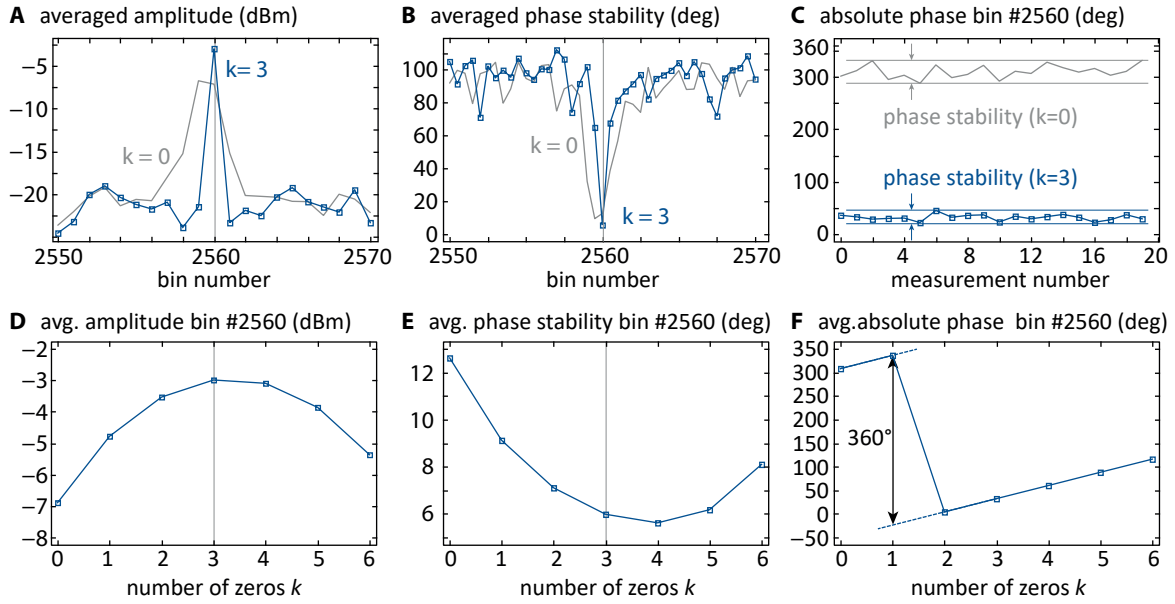


Fig. 5.7: Signal optimization with zero padding. A detailed description is found in the text.

nature of the frequency spectrum with frequency steps $d\nu$ the signal is not in general confined within a single frequency bin. Instead the signal “bleeds” to adjacent bins and the phase information is not contained in a single bin anymore. A continuous logging of the axial frequency accompanied by a random walk necessarily leads to such bleeding effects between bins.

In order to confine all available information within a single bin the time data is post-processed with *zero padding*. This means that k zeros are added to the time data leaving the time steps invariant

$$dt' = \frac{\Delta t'}{n'} = \frac{\Delta t + k dt}{n + k} = \frac{\Delta t}{n} = dt \quad (5.27)$$

but changing the frequency steps

$$d\nu' = \frac{1}{\Delta t'} = \frac{1}{\Delta t + k dt} \neq d\nu . \quad (5.28)$$

This process does not add any information to the transient but modifies the position of a signal relative to the bins. Choosing an appropriate number of zeros allows to center a signal within a bin which typically leads to an improved measured phase stability.

To get a clearer understanding of the process an example is given. Ten transient time signals with $\Delta t = 256$ ms and $n = 2^{14}$ at a frequency of 9998 Hz are generated and Gaussian white noise with a standard deviation of 10 Hz is overlaid. Based on this data the phase can be acquired 10 times. The frequency is chosen such that the signal is not well centered within a single bin

$$n = 9998 \text{ Hz} \times 256 \text{ ms} = 2559.49 . \quad (5.29)$$

The averaged amplitude of the ten measurements is shown in figure 5.7 A as the gray line. In the next step zeros are added to the time transient and the signal is analyzed again. The peak amplitude

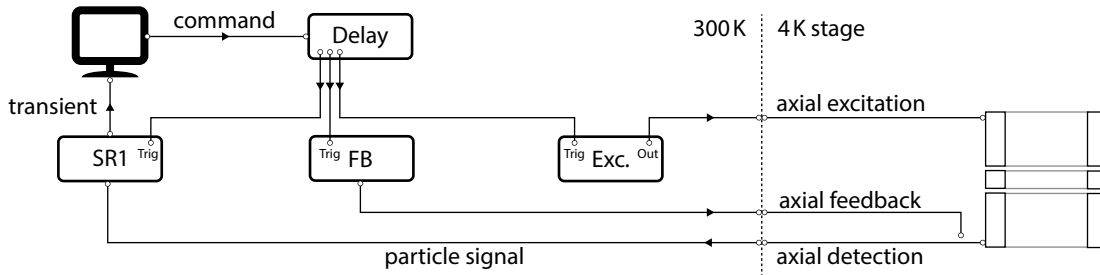


Fig. 5.8: Simplified experimental setup for the phase method consisting of a delay generator, a feedback generator, an excitation generator and an SR1 audio analyzer for the time data recording.

in bin 2560 as a function of these appended zeros is shown in **D** with a maximum for $k = 3$. This corresponds to the blue line in **A**. The signal is centered significantly better within a single bin. The absolute phase in bin 2560 for the individual measurements is plotted in **C**. The first observation is, that the absolute phase scales with the number of applied zeros, as shown in **F** with an additional phase jump of 2π . The second observation is the improved scatter of the phase, as indicated in figure **E** showing the average phase stability (standard deviation of the 10 individual phase measurements). Finally, **B** shows the same averaged phase stability for ± 10 bins around 2560. Once again the phase information is distributed over several bins in the unoptimized case (gray line) while after zero padding (blue line) the signal is better centered.

Zero padding has important consequences for the analysis. When dealing with long continuous measurements it allows to compensate drifts by centering the signal in the analysis. This leads to a significantly improved phase stability. Due to the scaling of the absolute phase with the number of zeros this must be carefully considered. However, since only relative frequencies matter for the spin state analysis in the AT, changing the absolute phase is of less concern. Finally, one should note that the ideal average amplitude does not necessarily correspond to the ideal average phase stability, compare **D** and **E**. Simulations show that the ideal number of zeros should be defined by maximizing the amplitude in the bin rather than by minimizing the phase stability. This leads in average to a better result with less scatter regarding the predicted absolute phase. The impact of zero padding on the data analysis is discussed at the end of section 5.2.4 on experimental results.

5.2 Experimental results

5.2.1 Setup

A simplified setup for the phase measurement is shown in figure 5.8. All instruments are phase locked with a Stanford Research Systems FS725 Rubidium Frequency Standard (not shown). Once the *SRS Digital Delay Generator DR645* receives the trigger command by the computer it starts its trigger sequence. First, the local oscillators used for down- and up-mixing (not shown) are triggered to initialize their internal phases to ensure they are the same for each new measurement. In the

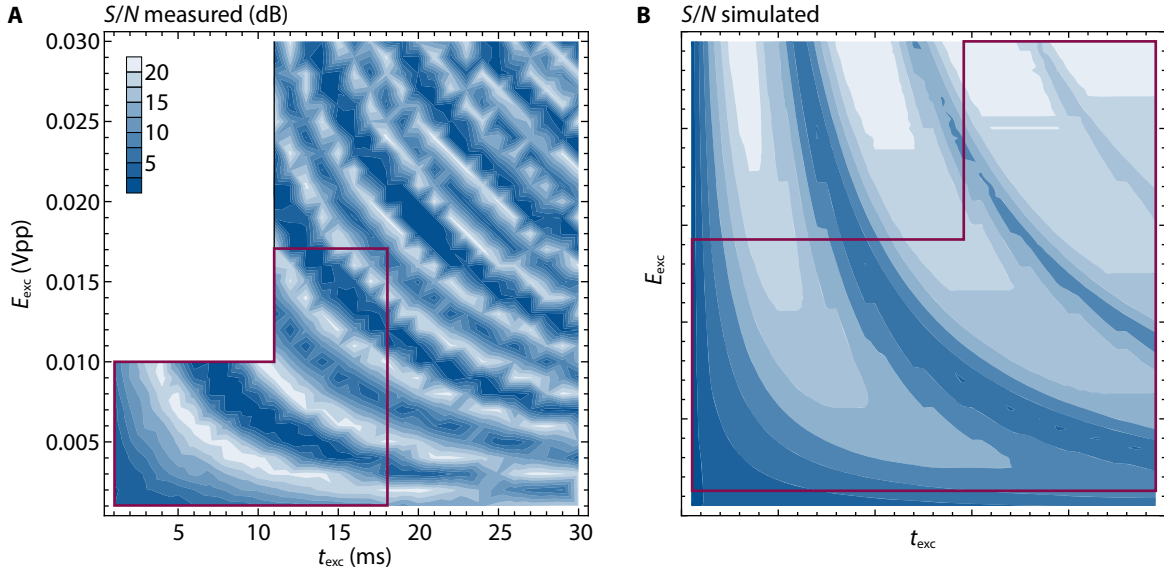


Fig. 5.9: (A) Signal-to-noise ratio measured in the PT as a function of excitation time t_{exc} and amplitude E_{exc} . The same behavior is found in the AT. The white area was not covered by the parametric measurement scheme. (B) Simulation of a driven Duffing oscillator (with $C_4 \neq 0$ and $C_6 \neq 0$) similar to experimental conditions. The plot shows the maximum amplitude (equivalent to the S/N) after the excitation time. The red borders indicate roughly the parts between measurement and simulation that correspond with each other.

second step the excitation generator is triggered and applies an excitation signal to the trap for the time t_{exc} with amplitude E_{exc} . The next trigger pulse activates the feedback to increase the resonator's time constant and the particle can evolve for t_{evol} . In the last step the feedback is turned off (or changed based on the measurement scheme) simultaneously with the transient readout with an SR1 Audio Analyzer. The SR1 allows the direct readout of the phase or the storage of the full time signal. Afterward, a time t_{cool} is added to ensure that the particle is back in equilibrium before the next excitation is applied.

5.2.2 Excitation pulse optimization

The initial excitation, defined by its frequency ν_{exc} , excitation time t_{exc} and amplitude E_{exc} , is highly important for the phase stability because it defines the S/N . The ideal frequency can be matched easily with a sufficiently broad excitation pulse but the ratio between time and amplitude remains to be optimized. In case of an ideal harmonic oscillator a longer time or amplitude both improve the resulting amplitude of the particle. However, the larger S/N does not necessarily lead to higher phase stability in a real Penning trap because larger axial amplitudes are accompanied by stronger deviations from the ideal quadrupole potential $C_4 \neq 0$ and $C_6 \neq 0$ introducing incoherent evolution. The better the ability to compensate the trap the larger amplitudes can be used to improve the phase stability by maximizing S/N .

The S/N as a function of t_{exc} and E_{exc} was measured in the PT and is shown in figure 5.9 A with

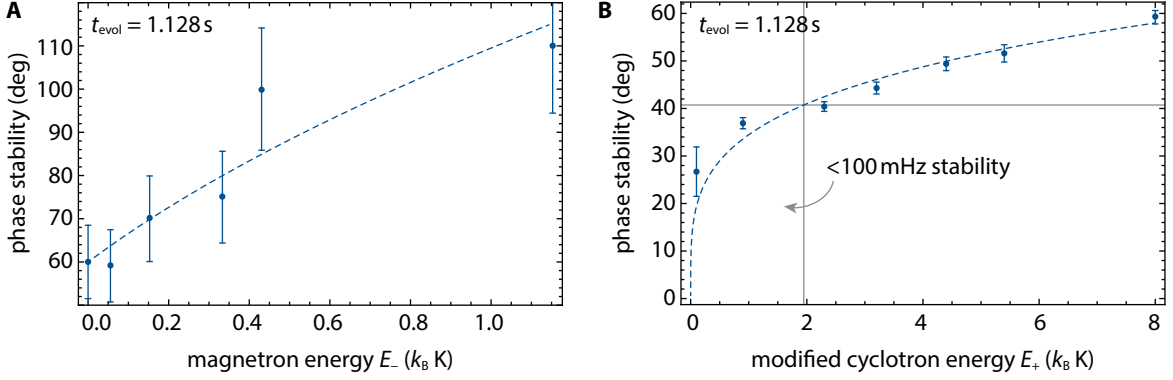


Fig. 5.10: (A) Scaling of the phase stability with the magnetron energy. The measurement was conducted at an early stage where the ultimate stability was not yet reached. The dashed line shows a two parameter fit based on the theoretical noise behavior $\sqrt{a + b E_-}$ for a fixed averaging time. (B) Scaling of the phase stability with the modified cyclotron energy where the number of averages was set to the ideal averaging time based on the Allan deviation. The dashed line shows the same expected $\sim E_+^{1/4}$ behavior as for measurements with dip spectra. However, due to the shorter measuring time the phase method allows a larger temperature acceptance.

a notable periodic structure. The same behavior was verified experimentally for S/N and the phase stability in the AT. The structure can be understood by solving the Duffing equation [59] (for simplification $q = m = V_0 = 1$)

$$\ddot{z} + \gamma \dot{z} + 2C_2 \left(z + 2 \frac{C_4}{C_2} z^3 + 3 \frac{C_6}{C_2} z^5 \right) = (\Theta(t) - \Theta(t - t_{\text{exc}})) E_{\text{exc}} \sin(\sqrt{2C_2}t) \quad (5.30)$$

and evaluating the achieved amplitude after the excitation time. The result of such a numerical simulation is presented in figure 5.9 B and is in fair qualitative agreement with the measured result. The larger the excitation amplitude, or excitation time, the more sensitive the phase evolution becomes on anharmonicities and the areas of good S/N smaller which can be seen on the diagonal of figure 5.9 A. For the measurement optimization the first maximum was chosen. Because of its wider distribution the optimization point is less sensitive to small changes of the ideal parameters.

5.2.3 Temperature optimization

The phase stability does not only depend on the parameters of the method but also on the axial stability itself. All typical optimization procedures outlined in the AT section 3.1.2 are also applicable for the phase stability. As discussed before in section 3.1 the axial stability strongly depends on the energy in the respective eigenmodes and scales with $\sqrt{a + b E_{\pm}}$ for a fixed averaging time and $c E_{\pm}^{1/4}$ for the ideal averaging time, where the parameters a, b and c depend on the individual contributions of noise and walk component. Figure 5.10 A shows an early measurement of the stability for different magnetron energies. For each point 50 phase measurements were performed and the stability evaluated.

The measurement with high impact for a g -factor measurement is shown in B. For each energy the phase was measured about 15 000 times. Naturally, during this time the phase passes 2π mul-

multiple times. A dedicated self-developed Mathematica algorithm was used to “unwrap” the phase and obtain a continuous evolution. Based on this signal the Allan deviation was calculated which yields the ideal number of measurements to reach the highest possible phase stability. For the lowest temperature of 0.1 K the ideal number of averages was found to be 9 corresponding to about 18 s of total measurement time. At 4 K the random walk is much stronger and only 2 number of averages should be chosen, about 4 s. The tremendous advantage of the phase method is the increase in temperature acceptance for the actual g -factor measurement. Typically, during the g -factor measurement cyclotron energies that correspond to < 100 mHz axial stability are accepted and allow for single spin-flip resolution. This corresponds to about 40° in phase stability which can be reached with particles up to 2 K instead of 600 mK in case of the normal dip spectrum method. In addition, the higher temperature acceptance allows for a faster particle preparation during the g -factor measurement. For typical parameters of the cyclotron detector temperature $T_+ = 3.2$ K the number of attempts to find a particle with sufficient energy can be reduced by about a factor of three.

5.2.4 Application to a Larmor resonance

The phase method was implemented in the analysis trap to measure the Larmor resonance in the presence of the magnetic bottle. For this purpose the phase is measured 10 times and averaged, followed by an excitation at ν_{exc} to drive spin transitions. Subsequently, another 10 phase measurements are conducted. The comparison between both average phases $\bar{\varphi}_i$ and $\bar{\varphi}_{i+1}$ yields the probability that a spin-flip occurred due to the excitation. For an evolution time of $t_{\text{evol}} = 1$ s and an averaging time of $t_{\text{avg}} = 0.256$ s the expected phase difference per spin-flip is $\Delta\varphi_{\text{SF}} = 70^\circ$. The sequence is repeated for several different excitation frequencies many times. Each phase measurement requires about 2 s and a measurement of $\bar{\varphi}_i$ about 20 s. This is a factor of 3 faster than the conventional method with a dip spectrum.

Analogously to section 3.4 a phase fluctuation can be defined as $\delta_i = \bar{\varphi}_i - \bar{\varphi}_{i+1}$. In the presence of spin-flips the standard deviation of the phase fluctuation Ξ increases weighted by the spin-flip probability

$$\Xi = \sqrt{\Xi_{\text{bg}}^2 + p_{\text{SF,AT}} \Delta\varphi_{\text{SF}}} , \quad (5.31)$$

where Ξ_{bg} is the background fluctuation without spin flips. Figure 5.11 A shows the equivalent data compared to figure 3.7 A but measured with the phase method. On- and off-resonant data points are clearly separated. The off-resonant background corresponds to an axial stability of

$$\Delta\nu = \frac{1}{t_{\text{evol}}} \frac{\Delta\varphi}{360^\circ} = \frac{1}{1.128 \text{ s}} \frac{46.8^\circ}{360^\circ} = 115 \text{ mHz} . \quad (5.32)$$

Using the threshold method (described in section 6.2.2) the data can be analyzed to assign the measured spin-flip probability to each excitation frequency. Due to the finite detection fidelity F the measured spin-flip probability p_{meas} is connected to the real spin-flip probability $p_{\text{SF,AT}}$ by

$$p_{\text{meas}} = p_{\text{SF,AT}} F + (1 - p_{\text{SF,AT}})(1 - F) , \quad (5.33)$$

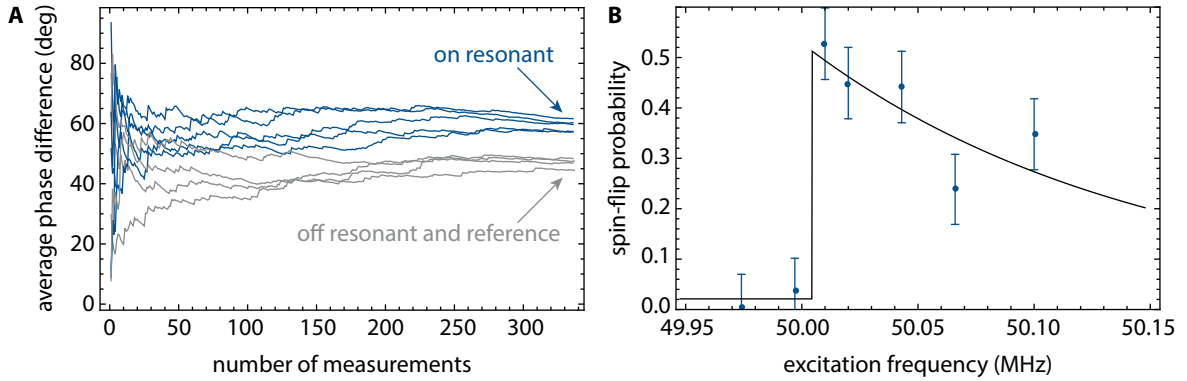


Fig. 5.11: (A) Evolution of the standard deviation of the phase fluctuation for different spin-flip drive frequencies. (B) The true spin-flip probability as a function of the Larmor excitation frequency is shown and was measured with the phase method.

where the fidelity is known by an off-resonant reference measurement. The final result in figure 5.11 B shows the Larmor resonance in the analysis trap measured with the phase method. The data was analyzed with zero-padding where it was ensured that for each pair of $\bar{\varphi}_i$ that are compared the same number of zeros was added. This is no limitation since usually the same number of zeros is required for subsequent measurements to center the frequency in a bin. The reason is that not more than 7 zeros ($t_{\text{avg}} = 256 \text{ ms}$, $n = 2^{14}$, $\nu_{\text{signal}} \approx 10 \text{ kHz}$) are required to center the particle within the next adjacent bin of width $d\nu \approx 3.9 \text{ Hz}$. Thus, each zero can correct for about 600 mHz frequency misplacement. This is about one order of magnitude more than the background stability and thus of no concern between measurements. Using zero padding the background stability was improved from $53.7(2.0)^\circ$ to $46.8(0.8)^\circ$, a significant improvement for the spin-flip measurement.

5.2.5 Single spin-flip resolution

The successful measurement of the Larmor resonance in the analysis trap demonstrated the ability to measure statistical spin-flips. However, the double trap method requires single spin-flip resolution with a stability below 40° for an evolution time of 1.128 s. This has been demonstrated before by measuring the axial frequency with dip spectra [74]. After careful optimization of all relevant parameters of the phase method discussed throughout the previous sections single spin flips were detected.

The result is shown in figure 5.12 and uses the same experimental scheme as explained for the Larmor resonance. The difference to the statistical demonstration is an improved background stability and the $\bar{\varphi}_i$ were obtained with only 7 measurements which leads to about 14 s to determine the spin state. The phase method allows the determination of the spin state about a factor of four faster which would reduce the total cycle time (compare section 7) by up to 33%. In addition, the higher temperature acceptance saves another 15% which in total almost doubles the data acquisition time.

Eventually, the final g -factor measurement was done with the measurement of frequency spectra

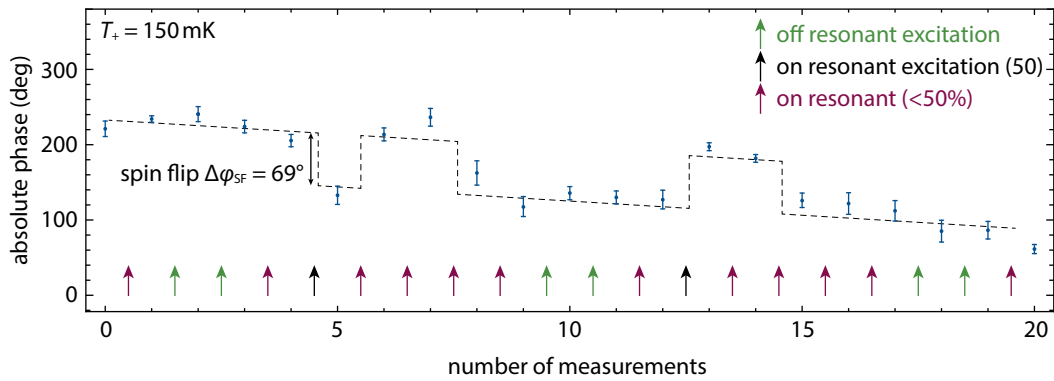


Fig. 5.12: Demonstration of single spin-flip resolution with the phase method. Discrete jumps are repeatedly observable overlaid by a small drift.

rather than the phase method. The reason is the temporal instability of the optimization parameters. Typically, an excellent stability was reached for a several hour measurement but afterward the stability at this parameter set became worse. This does not correlate with the stability measured with dip spectra and the reason for this behavior is not yet fully understood. The phase method would have required to re-optimize the parameters on a regular basis which cancels out the time savings.

One aspect, that was not discussed throughout this section, is the possibility to measure the modified cyclotron motion by the phase method using the methods PnP or PnA [86, 87]. This will become inevitable for future g -factor measurements due to the fact that the dip measurements reach a precision where the fit routine is limited. Furthermore, a direct measurement of the modified cyclotron frequency makes the result independent of the axial stability, which is the current limit in the experiment.

Chapter 6

Spin analysis

The experimental difficulty to find the Larmor frequency in the precision trap is due to the not directly accessible spin state in the precision trap. To determine whether a spin flip was induced during the Larmor excitation the spin state must be analyzed in the analysis trap where the spin state couples to the axial frequency. This is done twice, before and after the excitation of spin transitions in the precision trap, and a comparison before and after the procedures in the PT enables the assignment of a spin flip. In the first part of the chapter a likelihood function is derived which uses the information obtained in the AT to find the g -factor resonance parameters. The likelihood evaluation is based on probability theory and was first used in the previous g -factor measurement [76]. The second part discusses the algorithm to extract the spin state information based on axial frequency measurements in the AT. To that end, two different approaches are discussed, the *threshold method* which assigns binary values to the spin state up/down and the *Bayes method* which assigns continuous probabilities to be in a spin state. The last part describes simulations that test these methods and verify their validity.

6.1 Spin analysis in the precision trap

For the derivation of the likelihood function some basic relations are required and shall be presented without proof. Bayes' theorem connects the conditional probabilities of two events A and B

$$\mathcal{P}(A|B) = \mathcal{P}(B|A) \frac{\mathcal{P}(A)}{\mathcal{P}(B)} . \quad (6.1)$$

A new parameter C can always be introduced with the relation

$$\mathcal{P}(A) = \mathcal{P}(A|C) \mathcal{P}(C) + \mathcal{P}(A|\bar{C}) \mathcal{P}(\bar{C}) \quad (6.2)$$

with the complementary event $\mathcal{P}(\bar{C})$. Finally, reduction can be used to remove conditions if they add no additional information or are already included in other conditions

$$\mathcal{P}(A|BC) = \mathcal{P}(A|B) . \quad (6.3)$$

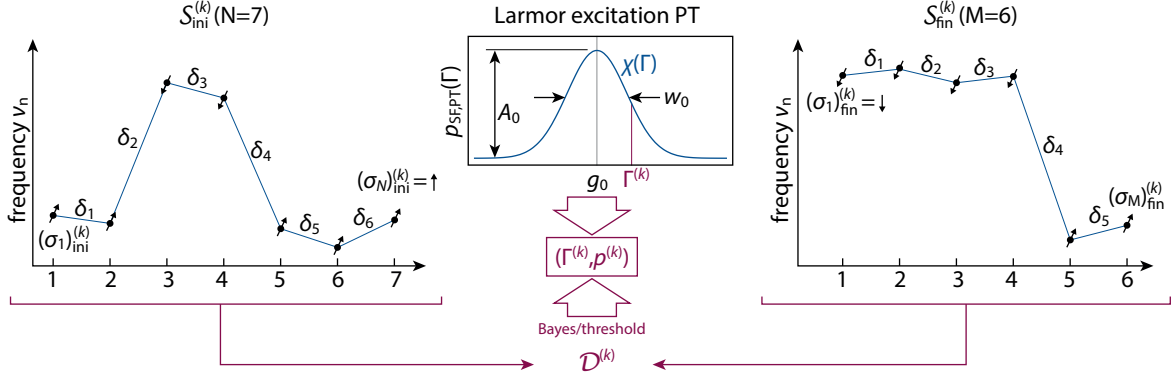


Fig. 6.1: The figure introduces many of the symbolic expressions used throughout this section for the k -th cycle of the g -factor measurement. Two axial series $\mathcal{S}_{\text{ini}}^{(k)}$ and $\mathcal{S}_{\text{fin}}^{(k)}$ are shown (left and right). The fluctuation data $(\delta_n)_{\text{ini}}^{(k)}$ and $(\delta_n)_{\text{fin}}^{(k)}$ are combined in the set $\mathcal{D}^{(k)}$. The Bayes or the threshold method is used to determine the initial $(\sigma_N)_{\text{ini}}^{(k)}$ and the final spin state $(\sigma_1)_{\text{fin}}^{(k)}$ and thus the probability $p^{(k)}$ for a spin flip in the precision trap. The center shows the g -factor resonance. The value of $\Gamma^{(k)}$ is defined by the Larmor excitation frequency and the measured free cyclotron frequency. Each cycle defines a tuple $(\Gamma^{(k)}, p^{(k)})$.

To begin, all necessary quantities shall be briefly defined, see figure 6.1. The evaluation assumes a g -factor resonance G with lineshape $p_{\text{SF,PT}}(\Gamma) = \chi(\Gamma; g_0, w_0, A_0)$ which yields the spin-flip probability as a function of Γ based on a resonance parameter set $\{g_0, w_0, A_0\}$. The parameters describe the position g_0 of the resonance, the width w_0 and the amplitude A_0 . In each cycle (k) a spin-flip attempt is performed at the frequency ratio $\Gamma^{(k)} = 2\nu_L^{(k)}/\nu_c^{(k)}$, where $\nu_c^{(k)}$ is the measured cyclotron frequency during cycle (k) and $\nu_L^{(k)}$ is the applied radiofrequency excitation to drive a spin flip in the PT. To determine whether the spin state changed during the excitation, two series of axial frequency measurements $\mathcal{S}_{\text{ini}}^{(k)} = \{\nu_1, \dots, \nu_N\}_{\text{ini}}^{(k)}$ and $\mathcal{S}_{\text{fin}}^{(k)} = \{\nu_1, \dots, \nu_M\}_{\text{fin}}^{(k)}$, before and after the spin-flip attempt, are measured in the AT to define the initial $(\sigma_N)_{\text{ini}}^{(k)}$ and the final spin state $(\sigma_1)_{\text{fin}}^{(k)}$. The two fluctuation series of the k -th cycle are combined by the definition $\mathcal{D}^{(k)} = \{\{\delta_1, \dots, \delta_{N-1}\}_{\text{ini}}^{(k)}, \{\delta_1, \dots, \delta_{M-1}\}_{\text{fin}}^{(k)}\}$ where the $\delta_n = \nu_n - \nu_{n+1}$ are the usual frequency differences of each series.

Now all parameters are introduced to define the probability for a specific g -factor resonance G under the condition that the axial fluctuations $\mathcal{D}^{(k)}$ were measured

$$\mathcal{P}(G|\mathcal{D}^{(1)} \dots \mathcal{D}^{(K)}) = \mathcal{P}(G|\{\mathcal{D}\}) \quad , \quad (6.4)$$

where the curly brackets are used as an abbreviation to indicate the set of fluctuations with K entries based on K measurement cycles. With Bayes' theorem this can be rewritten as

$$\mathcal{P}(G|\{\mathcal{D}\}) \stackrel{(6.1)}{=} \mathcal{P}(\{\mathcal{D}\}|G) \frac{\mathcal{P}(G)}{\mathcal{P}(\{\mathcal{D}\})} \quad , \quad (6.5)$$

where the term $\mathcal{P}(G)$ is the so-called prior probability which can be used to insert additional information. However, no such "additional knowledge" will be used. Instead, it is assumed that the prior is uniform over all resonance parameters which is a rather general assumption and certainly true. The term $\mathcal{P}(\{\mathcal{D}\})$ can be understood as an appropriate normalization constant and is of no further

concern at the moment. The remaining term can be simplified in the following calculation where the cycle index (k) is replaced on all terms by $*$ for simplicity:

$$\mathcal{P}(\{\mathcal{D}\}|G) = \prod_{k=1}^K \mathcal{P}(\mathcal{D}^*|G) \quad (\text{I})$$

$$\stackrel{(6.2)}{=} \prod_k \left[\mathcal{P}(\mathcal{D}^*|F^* G) \underbrace{\mathcal{P}(F^*|G)}_{=\chi^*} + \mathcal{P}(\mathcal{D}^*|\bar{F}^* G) \mathcal{P}(\bar{F}^*|G) \right] \quad (\text{II})$$

$$\stackrel{(6.3)}{=} \prod_k \left[\chi^* \mathcal{P}(\mathcal{D}^*|F^*) + (1 - \chi^*) \mathcal{P}(\mathcal{D}^*|\bar{F}^*) \right] \quad (\text{III})$$

$$\stackrel{(6.1)}{=} \prod_k \left[\chi^* \frac{\mathcal{P}(F^*|\mathcal{D}^*) \mathcal{P}(\mathcal{D}^*)}{\mathcal{P}(F^*)} + (1 - \chi^*) \frac{\mathcal{P}(\bar{F}^*|\mathcal{D}^*) \mathcal{P}(\mathcal{D}^*)}{\mathcal{P}(\bar{F}^*)} \right] \quad (\text{IV})$$

$$= \prod_k \left[\chi^* \frac{\mathcal{P}(F^*|\mathcal{D}^*)}{\alpha} + (1 - \chi^*) \frac{\mathcal{P}(\bar{F}^*|\mathcal{D}^*)}{1 - \alpha} \right] \mathcal{P}(\mathcal{D}^*) \quad (\text{V})$$

$$= \prod_k \left[\frac{\chi^* p^*}{\alpha} + \frac{(1 - \chi^*)(1 - p^*)}{1 - \alpha} \right] \mathcal{P}(\mathcal{D}^*) . \quad (6.6)$$

Step (I) assumes that the fluctuation series of individual cycles are logically independent. In that case it can be rewritten as a product over the total cycle number K . In step (II) a new parameter is introduced that describes whether a spin flip occurred $F^{(k)} = F^*$ in cycle (k) or not $\bar{F}^{(k)} = \bar{F}^*$. The term $\mathcal{P}(F^*|G)$ describes the probability for a spin flip under the condition of a specific resonance G . This is the spin-flip probability in cycle (k) which is given by the lineshape $p_{\text{SE,PT}}(\Gamma^{(k)}) = \chi(\Gamma^{(k)}) = \chi^*$. Step (III) removes the resonance condition G , because it is included in the information whether a spin flip occurred F^* or not \bar{F}^* . For step (IV) the Bayes theorem is used once more. The factor $\alpha = \mathcal{P}(F^*)$ lacks a physical interpretation because it describes the probability to have a spin flip without any background information. Finally, the term $\mathcal{P}(F^*|\mathcal{D}^*)$ in the last step is replaced with $p^{(k)} = p^*$ which is associated with the information obtained by the axial series in the AT, namely the probability for a spin flip based on the information of two axial series.

Equations (6.5) and (6.6) can be combined as

$$\mathcal{P}(G|\{\mathcal{D}\}) = \prod_k \left[\frac{\chi^{(k)} p^{(k)}}{\alpha} + \frac{(1 - \chi^{(k)})(1 - p^{(k)})}{1 - \alpha} \right] \mathcal{P}(G) . \quad (6.7)$$

The probability $\mathcal{P}(G|\{\mathcal{D}\})$ can be maximized with respect to the parameters of the lineshape $\chi^{(k)} = \chi^{(k)}(g_0, w_0, A_0)$. During the maximization the prior is kept constant or can be set to 1 which has no effect on the maximum of the function. The parameter α is set to 0.5 to give equal weighting of both summands¹. Finally, this defines the log-likelihood function to analyze the g -factor data

$$\mathcal{L} = 2 \sum_k \log \left[\chi(\Gamma^{(k)}; g_0, w_0, A_0) p^{(k)} + (1 - \chi(\Gamma^{(k)}; g_0, w_0, A_0))(1 - p^{(k)}) \right] , \quad (6.8)$$

where the data consists of K tuples $\{\Gamma^{(k)}, p^{(k)}\}_{k \in [1, \dots, K]}$. The $\Gamma^{(k)}$ values are directly measured in each cycle and are a direct input parameter. This leaves only the values $p^{(k)}$ to be derived, which is done

¹Instead of fixing α it can also be used as a parameter during the maximization. Simulations clearly show, however, that even for a fixed α the results are reliable and bias free. Thus maximizing with respect to α was not further investigated.

by analyzing the spin state in the analysis trap by comparing the initial and final spin state.

$$\begin{aligned}
p^{(k)} &= \mathcal{P}\left(F^{(k)} | \mathcal{D}^{(k)}\right) \\
&= \mathcal{P}\left(\uparrow_N | \{\delta_n\}_{\text{ini}}^{(k)}\right) \mathcal{P}\left(\downarrow_1 | \{\delta_n\}_{\text{fin}}^{(k)}\right) + \mathcal{P}\left(\downarrow_N | \{\delta_n\}_{\text{ini}}^{(k)}\right) \mathcal{P}\left(\uparrow_1 | \{\delta_n\}_{\text{fin}}^{(k)}\right) \\
1 - p^{(k)} &= \mathcal{P}\left(\bar{F}^{(k)} | \mathcal{D}^{(k)}\right) \\
&= \mathcal{P}\left(\uparrow_N | \{\delta_n\}_{\text{ini}}^{(k)}\right) \mathcal{P}\left(\uparrow_1 | \{\delta_n\}_{\text{fin}}^{(k)}\right) + \mathcal{P}\left(\downarrow_N | \{\delta_n\}_{\text{ini}}^{(k)}\right) \mathcal{P}\left(\downarrow_1 | \{\delta_n\}_{\text{fin}}^{(k)}\right) . \tag{6.9}
\end{aligned}$$

The probability for a spin flip in the PT during cycle k based on the two fluctuation series in the AT can be expressed as the probability to be \uparrow at the end of the initial series $\mathcal{P}(\uparrow_N | \{\delta_n\}_{\text{ini}}^{(k)})$ and \downarrow at the beginning of the final series $\mathcal{P}(\downarrow_1 | \{\delta_n\}_{\text{fin}}^{(k)})$, or vice versa and similarly in case of no spin flip during cycle (k). Each term on the right hand side has the same structure and gives the probability to be either spin up or spin down based on an observed fluctuation series.

To express the probability to be in a specific spin state based on measured data two methods will be discussed in the next section. The threshold method will assign the discrete values $\{0, 1\}$ to these probabilities. The Bayes method, however, allows assignment of continuous values in the interval $[0, 1]$. It can already be seen at this point, that the threshold method weights each data point equally, while the Bayes method includes the uncertainty in the measurement, an obvious advantage.

6.2 Spin analysis in the analysis trap

6.2.1 Measurement principle

To determine the spin state in the analysis trap an axial frequency series is measured where in between each two measurements a Larmor excitation is applied to change the spin. Such a series can be written as a set of axial frequencies given by $\mathcal{S} = \{\nu_1, \nu_2 \dots \nu_N\}$. The axial fluctuation $\delta_n = \nu_n - \nu_{n+1}$ of such a frequency series in the AT is shown in figure 6.2 as a histogram. The stability of the axial frequency for a given modified cyclotron energy is described by the blue normal distribution, where the left part of the figure shows a particle with low energy and the right part with high energy and a broader frequency distribution. The red curves shifted by $\pm \Delta\nu_{z,\text{SF}}$ are the distributions for events with a spin flip.

Based on these distributions each fluctuation point δ_n has some probability to belong to either the red or the blue curves and thus can be assigned to a spin state. If, for example, a jump of ± 200 mHz is observed during an axial series the probability that the particle is in spin down/up afterward is almost 100% for the left part of the plot with small background noise, whereas in the right plot this would correspond to 66% probability that the spin changed. This leaves a chance of 34% that the jump was just noise. To ensure that the spin state is always known with $>97\%$ certainty at the end of such a series, the measurement continues until the stop criterion is met $|\delta_{N-1}| = |\nu_{N-1} - \nu_N| > \Delta\nu_{\text{stop}}(E_+)$. This energy dependent threshold is chosen based on the noise model in the AT as introduced in section 3.1.

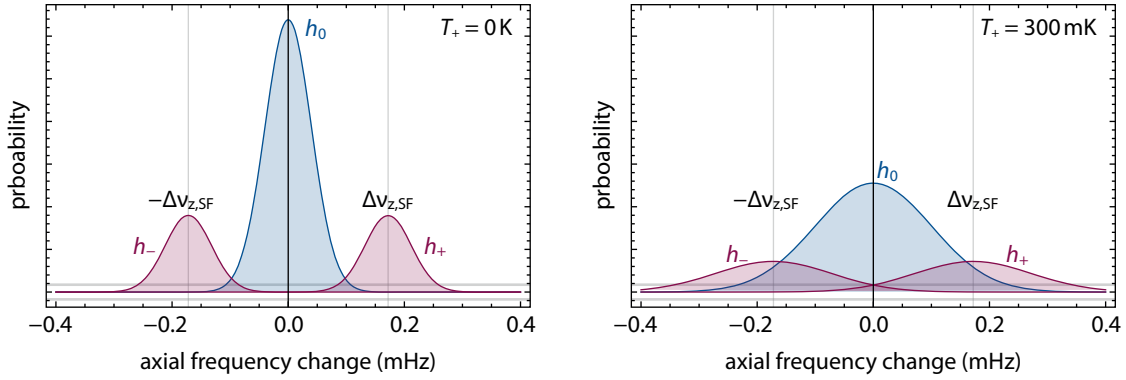


Fig. 6.2: Both plots show the probability to observe an axial frequency change during a sequence of axial measurements with spin-flip excitation in between. In the case of no spin flips only the blue curve h_0 is measured and defines the axial stability. The red curves h_{\pm} describe cases with spin flips and their relative amplitudes are defined by the spin-flip probability $p_{\text{SF,AT}} = 0.36$. In the case of a higher cyclotron energy the particle exhibits larger heating rates and thus a decreased stability which is shown by the broadened curves on the right hand side.

The stop criterion is a reliable choice to ensure high spin state detection fidelities at the end of a series. In principle, arbitrarily high detection fidelities can be reached by choosing a sufficiently large threshold. However, with increasing threshold the series becomes longer and consumes a significant amount of time (for example, in the g -factor measurement two axial series typically took 40 min which corresponds to 40 % of the total cycle time).

The more challenging and limiting factor for the spin state analysis is the determination of the spin state at the start of the series. Due to the fact that the first fluctuation point $|\delta_1| = |\nu_1 - \nu_2|$ is not necessarily significant relative to the background noise. Furthermore, it cannot even be ensured that a spin flip occurred during the first fluctuation point. In the next two sections two methods shall be discussed to assign spin states to the series.

6.2.2 Threshold method

The threshold method is discussed based on figure 6.3 where a typical axial series is shown in **A** with $\mathcal{S} = \{\nu_1, \dots, \nu_8\}$ and corresponding fluctuation $\{\delta_1, \dots, \delta_7\}$ in **B**. The series presented here is in case of small background fluctuations and the discrete step when a spin flip occurred can be identified easily. While such a clean trace of a spin flip will not be given for higher energies in general it is beneficial to discuss the method on a clear example.

Goal of the threshold method is to assign a spin state to the start and the end of the series. The true spin states σ_i can be written as $\{\sigma_1 = \uparrow, \dots, \sigma_8 = \uparrow\}$ and need to be identified by the threshold

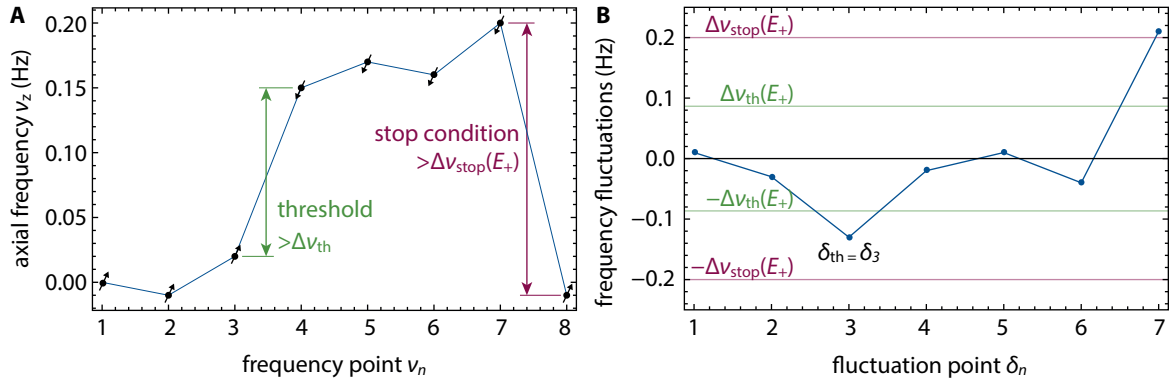


Fig. 6.3: (A) Typical axial frequency series in the analysis trap where the frequency is a function of the spin state. Once a frequency change larger than the stop condition, defined by the red threshold, is measured, the axial series ends and the spin state can be identified. To define the spin state at the start of the series, the green threshold criterion is being used, for more details see text. (B) Frequency fluctuations δ of corresponding axial series in (A). The final frequency change δ_7 meets the stop condition defined by the red lines, whereas δ_3 suffices the green threshold criterion.

method. The rule to assign a spin state with the threshold method is

$$\begin{aligned}
 \delta_n > \Delta\nu_{th} &\rightarrow \sigma_n = \downarrow \wedge \sigma_{n+1} = \uparrow && \text{spin flip} \\
 -\Delta\nu_{th} < \delta_n < \Delta\nu_{th} &\rightarrow \sigma_n = \sigma_{n+1} && \text{no spin flip} \\
 \delta_n < -\Delta\nu_{th} &\rightarrow \sigma_1 = \uparrow \wedge \sigma_{n+1} = \downarrow && \text{spin flip} .
 \end{aligned} \tag{6.10}$$

When applied to the example in figure 6.3, no spin flip occurred during ν_1 to ν_3 and ν_4 to ν_7 because $|\delta_n| < \Delta\nu_{th}$ for $n \in \{1, 2, 4, 5, 6\}$. Based on the first threshold event δ_{th} in a series the spin state σ_1 is determined. In this example, the first spin-flip event is δ_3 where the spin state changed from $\sigma_3 = \uparrow$ to $\sigma_4 = \downarrow$. Thus, the threshold method treats all prior spin states $n < 3$ with the same assignment and $\sigma_1 = \uparrow$. The stop criterion always ensures a significant frequency change $|\delta_{N-1}| = |\delta_7| > \Delta\nu_{stop} > \delta_{th}$ at the end of series and the final spin state can be determined with $\sigma_8 = \uparrow$. In the same manner, one can assign spin states to all frequencies of the whole series. In the example presented here, the threshold method is able to predict all values with correct values. However, for the general case with higher energies this will not be true and the method can even lead to inconsistencies. For example, two consecutive events with $\delta_n > 0$ and $\delta_{n+1} > 0$ both above the threshold would imply $\sigma_{n+1} = \uparrow \wedge \downarrow$. This problem occurs when the overlap of blue and red distribution in figure 6.2 is large and a frequency change by noise is assumed to be a spin flip and vice versa.

The choice of the threshold $\Delta\nu_{th}$ has a significant influence on the accuracy of the algorithm. From a heuristic point of view two limits may be considered. A very small threshold will almost always lead to the (usually false) identification of a spin flip. A very large threshold, on the other hand, will greatly reduce the false identification of spin flips in the presence of noise but also reduce the identification of real spin flips. None of these limits is desirable and the ideal threshold is in between.

To analyze the accuracy of the algorithm axial series with 100 000 frequency points were simulated

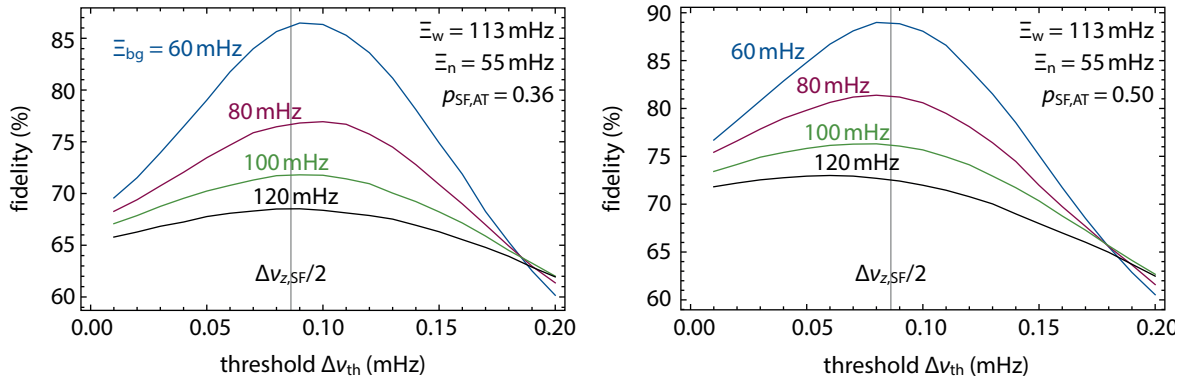


Fig. 6.4: The fidelity to detect a spin flip was evaluated for different thresholds and different background fluctuations Ξ_{bg} . The left plot was simulated with 36% spin-flip probability and the right plot with 50%. It can be seen that the ideal threshold parameter is a function of the background noise level and the spin-flip probability. A first estimate for an appropriate threshold is $\Delta v_{z,SF}/2$.

based on the noise model in the AT. The threshold method was then used to analyze the spin states and compare them to the original spin states. The fidelity, defined as

$$\mathcal{F} = \frac{N_{\text{correct}}}{N_{\text{correct}} + N_{\text{incorrect}}} \quad (6.11)$$

is the number of correctly identified spin states N_{correct} divided by the total number of spin states in the series. Note that the fidelity takes values between 50% and 100%. The result of such simulations is shown in figure 6.4 for two different spin-flip probabilities. The result clearly indicates that the threshold that maximizes the fidelity depends on the background noise and the spin-flip probability. A higher threshold reduces noise related false detections but at the same time more real spin flips are missed. The latter is suppressed in case of a low spin-flip probability which yields a higher fidelity at a higher threshold.

A big advantage of the threshold method is its simplicity. If a fixed threshold is chosen, instead of a varying function of the background noise, the threshold method is even independent of the noise model and requires only the frequency jump due to a spin flip $\Delta v_{z,SF}$ as input parameter. On the other hand, it does not offer any information about the significance of a spin flip and the determination is binary. The Bayes method, as described in the next section, will introduce probabilities between 0 and 1 that provide a weighting.

6.2.3 Bayesian method with random walk

The calculations in this section are closely related to [88] and lead to the same final result. The Bayes method as introduced here is a simplification of the original Bayes method which is discussed in great detail in [76]. While the simplified model allows less improvement compared to the threshold method it still presents an important consistency check. The Bayes approach with the full noise model (white noise + walk) has a larger noise model dependence and thus requires more input parameters which might prove less robust. The simplified model, on the other hand, only requires an

effective walk amplitude $\Xi_{w,\text{eff}} = \sqrt{\Xi_n^2 + \Xi_w^2}$, compare section 3.1. The greater model independence is won at the cost of a smaller detection fidelity. However, both algorithms were tested and led to the same consistent result within error bars and the same error.

The Bayes method is used to assign the probability, as introduced in (6.9), to be either spin up or down based on an observed frequency series. The calculation is based on the probability $P_n^\uparrow = \mathcal{P}(\uparrow_n | \{\delta_n\}) = \mathcal{P}(\sigma_n = \uparrow | \{\delta_n\})$ to be in the spin up state at position n of an axial frequency series under the condition that the fluctuation of the whole series is known. Recall that the fluctuation of a frequency series $\mathcal{S} = \{\nu_1, \dots, \nu_N\}$ is abbreviated with $\{\delta_n\} = \{\delta_1, \dots, \delta_{N-1}\}$ and the spin states with $\{\sigma_1, \dots, \sigma_N\}$. Additional abbreviations, $\uparrow_n = \uparrow$, $\uparrow_{n-1} = \uparrow'$, $\Delta = \{\delta_1, \dots, \delta_{n-1}\}$ and $\Delta' = \{\delta_1, \dots, \delta_{n-2}\}$, indicate that the last element is removed from the list. Furthermore the complementary event of $\mathcal{P}(\uparrow_n)$ is written as $\mathcal{P}(\downarrow_n)$:

$$\begin{aligned}
P_n^\uparrow &= \mathcal{P}(\uparrow_n | \{\delta_n\}) \\
&\stackrel{(6.3)}{=} \mathcal{P}(\uparrow_n | \Delta) \\
&\stackrel{(6.2)}{=} \mathcal{P}(\uparrow | \uparrow' \Delta) \cdot \mathcal{P}(\uparrow' | \Delta) + \mathcal{P}(\uparrow | \downarrow' \Delta) \cdot \mathcal{P}(\downarrow' | \Delta) \\
&\stackrel{(6.1)}{=} \frac{\mathcal{P}(\delta_{n-1} | \uparrow \uparrow' \Delta') \mathcal{P}(\uparrow | \uparrow' \Delta')}{\mathcal{P}(\delta_{n-1} | \uparrow \uparrow' \Delta')} \cdot \frac{\mathcal{P}(\delta_{n-1} | \uparrow' \Delta') \mathcal{P}(\uparrow' | \Delta')}{\mathcal{P}(\delta_{n-1} | \Delta')} + (\text{with } \downarrow') \\
&= \frac{\mathcal{P}(\delta_{n-1} | \uparrow \uparrow' \Delta')}{\mathcal{P}(\delta_{n-1} | \Delta')} \underbrace{\mathcal{P}(\uparrow | \uparrow' \Delta')}_{1 - p_{\text{SE,AT}}} \underbrace{\mathcal{P}(\uparrow' | \Delta')}_{P_{n-1}^\uparrow} + (\text{with } \downarrow') \\
&= \frac{\mathcal{P}(\delta_{n-1} | \uparrow \uparrow' \Delta')}{\mathcal{P}(\delta_{n-1} | \Delta')} (1 - p_{\text{SE,AT}}) P_{n-1}^\uparrow + \frac{\mathcal{P}(\delta_{n-1} | \uparrow \downarrow' \Delta')}{\mathcal{P}(\delta_{n-1} | \Delta')} p_{\text{SE,AT}} (1 - P_{n-1}^\uparrow) \\
&\stackrel{(6.3)}{=} \frac{\mathcal{P}(\delta_{n-1} | \uparrow \uparrow')}{\mathcal{P}(\delta_{n-1})} (1 - p_{\text{SE,AT}}) P_{n-1}^\uparrow + \frac{\mathcal{P}(\delta_{n-1} | \uparrow \downarrow')}{\mathcal{P}(\delta_{n-1})} p_{\text{SE,AT}} (1 - P_{n-1}^\uparrow) . \tag{6.12}
\end{aligned}$$

The last step is justified if the fluctuation is uncorrelated and the frequency change δ_{n-1} only depends on the spin states σ_n and σ_{n-1} . This assumption is true for a frequency series with a walk defined by $\nu_n = \nu_{n-1} + N(0, \sigma_w)$ where $N(0, \sigma_w)$ stands for a normally distributed random number. In comparison, a frequency series with white noise $\nu_i = \nu_0 + N(0, \sigma_n)$ does have uncorrelated frequencies, but the fluctuation is correlated. This is the key difference compared to [74, 76] where not the fluctuations are treated as independent but the absolute frequencies.

Equation (6.12) can be used recursively for a known starting parameter P_1^\uparrow . The only missing ingredient is the calculation of $\mathcal{P}(\delta_{n-1} | \uparrow \uparrow')$ and $\mathcal{P}(\delta_{n-1})$. Both probabilities can be expressed with the three normal distributions shown in figure 6.2. The probability $\mathcal{P}(\delta_{n-1})$ to observe a frequency change in the interval $I = (\delta_{n-1} - \epsilon, \delta_{n-1} + \epsilon)$ is

$$\mathcal{P}(\delta_{n-1}) = \lim_{\epsilon \rightarrow 0} \int_I d\nu (1 - p_{\text{SE,AT}}) h_0 + P_{n-1}^\uparrow p_{\text{SE,AT}} h_- + (1 - P_{n-1}^\uparrow) p_{\text{SE,AT}} h_+ . \tag{6.13}$$

The h_0 term is the probability that no spin flip occurs, weighted with $1 - p_{\text{SE,AT}}$. The last two terms h_\pm take into account that a spin flip occurred based on the probability P_{n-1}^\uparrow that the spin state was up before. If, for example, it is known that the spin state was up $P_{n-1}^\uparrow = 1$, the spin state can only change to down with probability $p_{\text{SE,AT}}$, which is described by the distribution h_- . Similar to $\mathcal{P}(\delta_{n-1})$ the

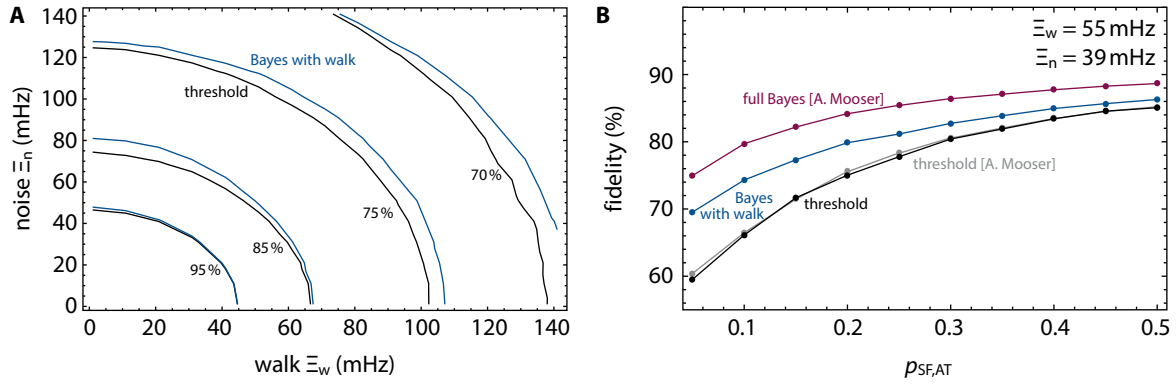


Fig. 6.5: (A) Fidelity comparison of the threshold and the Bayesian method for various noise parameters. The rippled behavior is due to limited simulation resolution. The Bayes method in blue exceeds the performance of the simple threshold approach. (B) Fidelity as a function of the spin-flip probability. The red and the gray line are taken from [76] and show the fidelity for the full Bayes approach and the threshold method. Blue and black are new simulations for this thesis. Full Bayes and Bayes with random walk are superior compared to the threshold method.

probability $\mathcal{P}(\delta_{n-1} | \uparrow\uparrow')$ to observe a frequency change δ_{n-1} , if both spin states before and after are known, can be defined as

$$\mathcal{P}(\delta_{n-1} | \uparrow\uparrow') = \lim_{\epsilon \rightarrow 0} \int_I dv h_0, \quad \mathcal{P}(\delta_{n-1} | \uparrow\downarrow') = \lim_{\epsilon \rightarrow 0} \int_I dv h_+ . \quad (6.14)$$

Although all limits converge to 0 due to the infinitesimally small interval the ratio has a finite value which can be calculated with L'Hôpital's rule [89]. For example, in the case of $\lim f(x) = \lim g(x) = 0$ the limes $\lim f(x)/g(x)$ can be calculated with L'Hôpital's rule $\lim f'(x)/g'(x)$. Together with (6.12) – (6.14) this leads to result

$$P_n^\uparrow = \frac{(1 - p_{\text{SF,AT}}) h_0 P_{n-1}^\uparrow + p_{\text{SF,AT}} h_+ (1 - P_{n-1}^\uparrow)}{(1 - p_{\text{SF,AT}}) h_0 + P_{n-1}^\uparrow p_{\text{SF,AT}} h_- + (1 - P_{n-1}^\uparrow) p_{\text{SF,AT}} h_+} , \quad (6.15)$$

and similarly, for the probability to be spin down at the n -th position

$$P_n^\downarrow = \frac{p_{\text{SF,AT}} h_- P_{n-1}^\uparrow + (1 - p_{\text{SF,AT}}) h_0 (1 - P_{n-1}^\uparrow)}{(1 - p_{\text{SF,AT}}) h_0 + P_{n-1}^\uparrow p_{\text{SF,AT}} h_- + (1 - P_{n-1}^\uparrow) p_{\text{SF,AT}} h_+} \quad (6.16)$$

which necessarily fulfill the relation $P_n^\uparrow + P_n^\downarrow = 1$.

With the algorithm at hand any series can now be analyzed to define the spin states. The first frequency measurement of the series contains no information about the spin state of the particle, because at least two measurements are required. This maximum uncertainty is expressed by setting $P_1^\uparrow = P_1^\downarrow = 0.5$. The second frequency measurement yields the first fluctuation data point δ_1 which can be used to calculate

$$P_1^\uparrow = \frac{(1 - p_{\text{SF,AT}}) h_0(\delta_1) 0.5 + p_{\text{SF,AT}} h_+(\delta_1) 0.5}{(1 - p_{\text{SF,AT}}) h_0(\delta_1) + 0.5 p_{\text{SF,AT}} h_-(\delta_1) + 0.5 p_{\text{SF,AT}} h_+(\delta_1)} . \quad (6.17)$$

and likewise for additional frequency measurements. This is repeated until the probability to be spin up at the end of the series P_N^\uparrow is known. To calculate P_1^\uparrow the fluctuation series is inverted $\{\delta_N - 1, \dots, \delta_1\}$ and the algorithm is applied again. Necessary input parameters of the algorithm are the spin-flip probability in the AT $p_{\text{SF,AT}}$, the effective background fluctuation for a given energy $\Xi_{\text{w,eff}}(E_+)$ and the size of a frequency jump due to a spin flip $\Delta\nu_{z,\text{SF}}$.

The algorithm is compared to the previously discussed threshold method and to the full Bayes model described in [76, 74] and shown in figure 6.5 for various noise parameters and as a function of the spin-flip probability in the analysis trap. In general, the performance of the Bayes method exceeds the threshold method due its more efficient use of available information. While the threshold method only takes into account a single frequency change the Bayes method continuously updates the probability and uses all available information of the whole series. It is important to note, that this advantage does not come from any information added by the prior and no theoretical assumptions about the measurement enter the evaluation.

Chapter 7

The g -Factor Measurement

This chapter discusses the measurement of the proton g factor at a fractional precision of 300 ppt. The measurement is the main part of this thesis and constitutes the most precise measurement of any nuclear moment to date. In the first part, the measurement scheme and experimental procedures are explained in detail. The next part covers the statistical analysis and introduces several crosschecks, such as Monte-Carlo simulations, that were performed to justify the analysis. After the discussion of all systematics the final result is used to set new improved constraints on CPT symmetry violation in the baryonic sector.

7.1 Measurement scheme

A detailed scheme of the g -factor measurement is shown in figure 7.1 as a flow chart. The measurement cycle, with index k , begins with a single proton stored in the precision trap (boxes in green). To initialize the proton spin state the particle's modified cyclotron mode is cooled to sub-thermal energies, referred to as *Cooling*, which ensures that the cyclotron energy is below the threshold $E_{\text{th},+}$ which is essential for sufficient high fidelity spin state detection. To efficiently cool the proton with energy $\langle E_+ \rangle = k_{\text{B}} T_+ = k_{\text{B}} \frac{\omega_{\pm}}{\omega_z} T_z \approx k_{\text{B}} 600 \text{ K}$ (as a result of the previous sideband coupling between cyclotron and axial mode in cycle $k - 1$) a cyclotron axial sideband coupling with feedback is carried out. The feedback reduces the axial energy and the proton typically ends up with $E_+ \approx k_{\text{B}} 150 \text{ K}$. Next, the cyclotron resonator is tuned to resonance with the modified cyclotron frequency and the particle thermalizes with the thermal bath of the resonator at $T_+ = 6 \text{ K}$. After 60 s, feedback is applied to the cyclotron resonator which decreases the temperature to about 3 K. The reason for this two step process is the cooling time of the resonator which becomes larger if negative feedback is applied. Thus, cooling the particle from high energies with feedback is less efficient. Next, the magnetron mode is cooled and the proton is transported to the AT (boxes in red) where the absolute energy can be measured in the magnetic bottle. A comparison of the axial frequency with a previ-

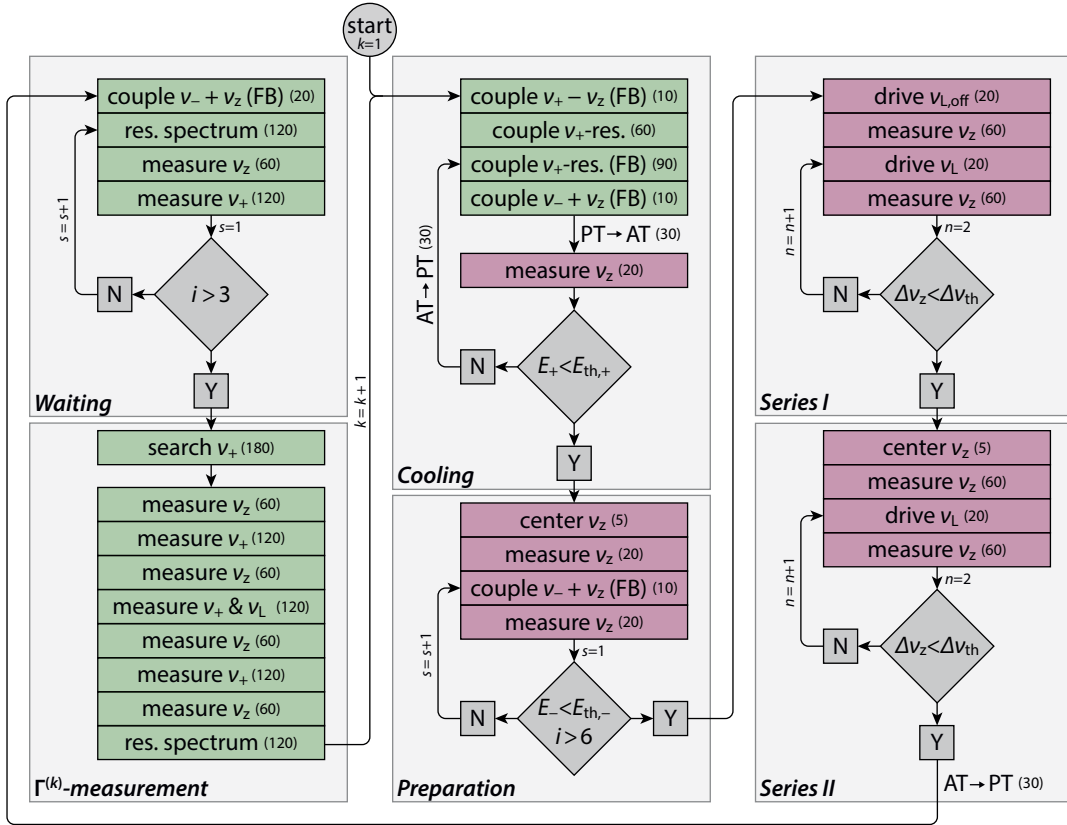


Fig. 7.1: Detailed measurement scheme as a flow diagram with cycle number k . Green/red boxes indicate the position of the proton in the PT/AT. Timings in seconds are shown in brackets. The first column typically requires 30 min, the Cooling about 20 min and the Preparation and Series another 40 min. This leads to a total cycle time of 90 min in average. Further details are explained in the text.

ously calibrated 0 K cut yields the temperature of the proton, compare section 3.2. If the energy is below the threshold energy, $E_+ < E_{th,+} = 0.6 k_B$, the spin state analysis is performed. Otherwise, the proton is transported back to the PT and thermalized once more by coupling it to the cyclotron resonator with feedback.

The *Preparation*-procedure in the AT starts by centering the particle with respect to the axial resonator by adjusting the AT ring voltage. To achieve a small magnetron energy magnetron sideband cooling with feedback is repeatedly applied followed by a measurement of the axial frequency. After acquiring 6 such frequencies, corresponding to 6 magnetron temperatures, the minimum frequency $\nu_{z,min}$ is used to define the threshold $\nu_z(E_{th,-}) = \nu_{z,min} + 1$ Hz. This method is a compromise between two limits. In the first limit, the particle is coupled only once which can result in a high magnetron energy due to the probabilistic nature of the thermalization process. In the second limit, the particle is coupled many times to record a Boltzmann distribution with well-defined 0 K cut. The measurement of 6 magnetron energies is thus a subset of a Boltzmann distribution but less time consuming. By shifting the cut by 1 Hz (this is an energy shift of $\Delta E_- = k_B 14$ mK) a small preparation time is

guaranteed. Otherwise it can occur that the axial frequency drifts upwards due to external changes (e.g. temperature drift) and the routine would never find a particle that fulfills $E_- < E_{\text{th},-}$. The preparation procedure cools the magnetron mode by $\Delta E_- = k_B 55(14)$ mK, on average. The highest energy reduction was 180 mK which improves the axial fluctuations by about 10 mHz.

The proton is now prepared with the magnetron and the modified cyclotron energy below the threshold energies which corresponds to an axial stability suitable to determine the spin state in *Series I*. Measurements with a temperature sensor close to the trap clearly indicate that the trap system is heated up by at least 50(5) mK during the application of the Larmor drive. To ensure that each axial frequency measurement is conducted with the same background temperature an off-resonant drive is applied to heat up the trap. Next, the axial frequency is measured alternating with resonant Larmor excitations until the threshold criterion for the axial series is fulfilled (see section 6.2). After the first axial series the particle is re-centered because a long series can easily consume more than an hour and during such a time window the walk nature of the motion leads to shifts of several Hz. The second axial series, *Series II*, is not necessary for the double trap method because the spin state was already defined by the first series. However, measuring two series provides an important measure for the fidelity of the double trap method. No spin flip is driven between Series I and Series II, thus, comparing the measured spin-flip probability between both with the ideal probability of $p_{\text{SF,AT}} = 0\%$ immediately allows to see whether problems are present in the routine. Especially in the beginning, when the resonance shape is not yet known, it is beneficial to have such a reference measurement.

After the spin state initialization, the particle is transported to the precision trap to perform the high-precision frequency measurements. Once the transport routine is finished the magnetron motion is coupled to the thermal bath of the axial resonator again to ensure that the energy of the magnetron mode is well-defined. In addition, the *Waiting* period consists of successive measurements of a reference axial resonance spectrum, ν_z and ν_+ , respectively, which are repeated three times. This waiting period of 15 min is necessary for the temperature of the apparatus to settle down from the heated state due to the already mentioned heating effect of the trap, which is induced by the high-power spin-flip drive. It should be noted that even after this waiting period the apparatus is not in equilibrium but is sufficiently stable for a sub-ppb measurement.

The cyclotron search is the first part of the $\Gamma^{(k)}$ -*measurement*. It accounts for magnetic field drifts and is a small routine in its own that autonomously finds the cyclotron frequency by probing the sideband frequency. Usually this search is not necessary and a successful double dip is established during the first attempt using the $k - 1$ coupling frequency of the previous cycle. To define the cyclotron and the Larmor frequency, and thus the ratio $\Gamma^{(k)} = 2\nu_c/\nu_{\text{L,exc}}$, first the sequence $\nu_z \rightarrow \nu_+ \rightarrow \nu_z$ is measured, followed by the measurement of ν_+ while the Larmor drive is applied, and finally another sequence $\nu_z \rightarrow \nu_+ \rightarrow \nu_z$. These numerous measurements allow to precisely track drifts in the axial and modified cyclotron frequency which can be accounted for in the systematics. The Larmor excitation is done at a frequency of $\nu_{\text{L,exc}} = \nu_{\text{L}} + \Delta\nu_{\text{L}}$ with randomized offset $\Delta\nu_{\text{L}}$ around the expected Larmor frequency ν_{L} . After the determination of all relevant frequencies another resonator reference spectrum is measured. The measurement of the modified cyclotron frequency via sideband coupling unavoidably increases the cyclotron energy and the particle needs to be re-cooled again which is the

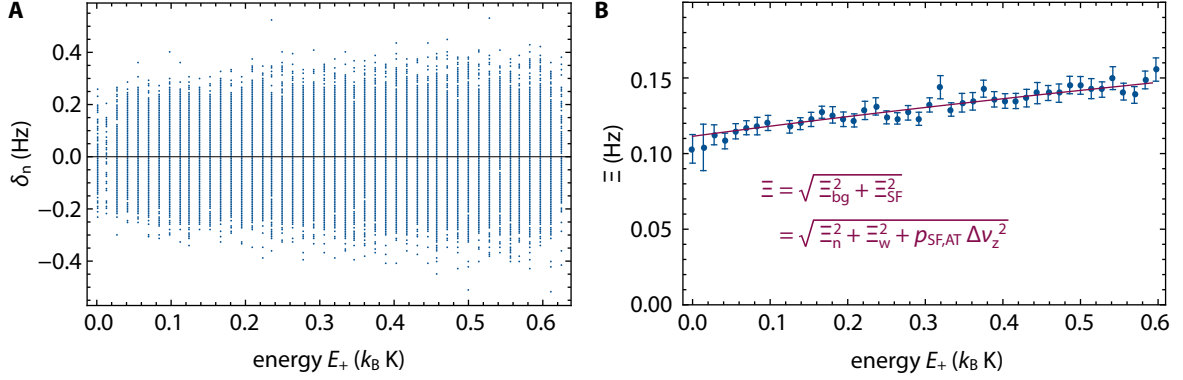


Fig. 7.2: (A) The points δ_n of all series are shown at their respective energies. The width of these points characterized by the standard deviation is a measure for the stability of the motion in the presence of spin flip and is shown in (B) by the blue points with error bars. The red line is a fit to the data as described in the text.

point where the cycle starts at its beginning once again.

The total cycle time of the g-factor routine is about 90 min. The initial particle cooling requires about 20 min and is followed by the preparation and the two axial series with in total 40 min. The frequency measurement in the PT then adds another 30 min, including the 15 min waiting period. The cycle time greatly varies due the probabilistic nature of the cooling procedure as well as due to the spin state analysis. For example, the shortest cycle lasted only 50 min while the longest cycle was 225 min.

7.2 Data analysis

7.2.1 Statistical g-factor

The data that was taken during the g-factor measurement consists of 1314 $\Gamma^{(k)}$ -ratios with initial and final spin state determination in the AT and was acquired during August 2016 and December 2016. Three individual protons with 420, 317 and 577 $\Gamma^{(k)}$'s were measured. To determine the g-factor resonance the likelihood function in equation (6.8)

$$\mathcal{L} = 2 \sum_k \log \left[\chi(\Gamma^{(k)}; g_0, w_0, A_0) p^{(k)} + (1 - \chi(\Gamma^{(k)}; g_0, w_0, A_0))(1 - p^{(k)}) \right] \quad (7.1)$$

is considered, where $\Gamma^{(k)}$ and $p^{(k)}$ are defined by the measurement data. It has been shown in chapter 6 that the probability for a spin flip in the precision trap is the result of two series of axial frequency measurements before and after the Larmor excitation in the PT. To derive $p^{(k)}$ based on equation (6.9) the adjacent series to each $\Gamma^{(k)}$ are considered

$$\dots \underbrace{\Gamma^{(k-1)} \rightarrow \mathcal{S}_1^{(k-1)} \rightarrow \mathcal{S}_2^{(k-1)}}_{\text{cycle } k-1} \mid \underbrace{\Gamma^{(k)} \rightarrow \mathcal{S}_1^{(k)} \rightarrow \mathcal{S}_2^{(k)}}_{\text{cycle } k} \mid \underbrace{\Gamma^{(k+1)} \rightarrow \mathcal{S}_1^{(k+1)} \rightarrow \mathcal{S}_2^{(k+1)}}_{\text{cycle } k+1} \dots \quad (7.2)$$

namely $S_2^{(k-1)} = S_{\text{ini}}^{(k)}$ and $S_1^{(k)} = S_{\text{fin}}^{(k)}$ to define the initial $\mathcal{P}(\uparrow_N | \{\delta_n\}_{\text{ini}}^{(k)}) = (P_n^{\uparrow})_{\text{ini}}^{(k)}$ and the final $\mathcal{P}(\uparrow_1 | \{\delta_n\}_{\text{fin}}^{(k)}) = (P_1^{\uparrow})_{\text{fin}}^{(k)}$ probability to be in the spin up state as in section 6.2.3. The Bayesian algorithm requires the axial frequency stability as a function of the particle energy as input parameter. This was evaluated in a global analysis over all axial series in all measured cycles. Each series contributes between 1 and $N - 1$ points for a known energy. After several hundred such series the whole energy range is covered and the data can be binned, see figure 7.2. In order to separate the background fluctuation Ξ_{bg} , as introduced in section 3.1, from the total fluctuation Ξ , that includes spin flips, the data is fit by

$$\Xi = \sqrt{\Xi_n^2 + \Xi_w^2 + p_{\text{SF,AT}} \Delta \nu_{z,\text{SF}}}, \quad \Xi_w^2 \sim T_+ \quad (7.3)$$

with free parameters Ξ_n , for the white noise contribution and Ξ_w for the walk contribution. The spin-flip probability is determined by a separate measurement, see section 3.4, and found to be $p_{\text{SF,AT}} = 0.366(16)$. The result of the fit are the correlated parameters $\Xi_n = 40.0(5.0)$ mHz and $\Xi_w = 124.0(5.3)$ mHz. This analysis assumes that the fluctuations were stable over time, which is supported by independent measurements of the fluctuations before and after the g-factor measurement.

$\Gamma^{(k)}$ is defined based on the frequency measurements in the precision trap. Each ratio $\Gamma^{(k)}$ is defined as

$$\Gamma^{(k)} = 2 \frac{\nu_c^{(k)}}{\nu_{\text{L,exc}}^{(k)}} \quad (7.4)$$

with measured cyclotron frequency $\nu_c^{(k)}$, and Larmor excitation $\nu_{\text{L,exc}}^{(k)} = \nu_{\text{L}} + \Delta \nu_{\text{L}}^{(k)}$. The result of the cyclotron frequency search is used to calculate the expected Larmor frequency which is then shifted by a random offset $\Delta \nu_{\text{L}}^{(k)}$ to scan the resonance. The knowledge of the resulting excitation frequency $\nu_{\text{L,exc}}^{(k)}$ is limited only by the external Rubidium FS725 frequency standard which is negligible for the measurement with an accuracy of 5×10^{-11} . The more challenging part is the determination of the free cyclotron frequency which is obtained through the invariance theorem. During the excitation with $\nu_{\text{L}}^{(k)}$, only the frequencies ν_1 and ν_r are measured. To avoid systematic shifts of the g factor induced by axial frequency drifts a careful study of the axial drift behavior is essential.

To prevent a systematic shift on g it must be ensured that the axial frequency during the excitation is interpolated correctly based on the axial frequency measurements conducted before and after the excitation. The main uncertainty are possible drifts of the proton's eigenmotions due to temperature drifts induced by the Larmor drive in the analysis trap. The effect of the excitation pulses on the temperature of the apparatus is shown in figure 7.3 A and was measured with a temperature sensor (*CERNOX CU-CX-1050*) on the 4 K stage of the experiment. Each peak is caused by an excitation pulse in the AT where the first peak is slightly higher due to an off-resonant drive. The custom filter setup, used to reduce external noise signals, led to a slightly higher power dissipation at the off-resonant drive frequency. After the last drive of the second series the temperature of the apparatus slowly settles down. The average temperature drop after the last excitation is shown in 7.3 B .

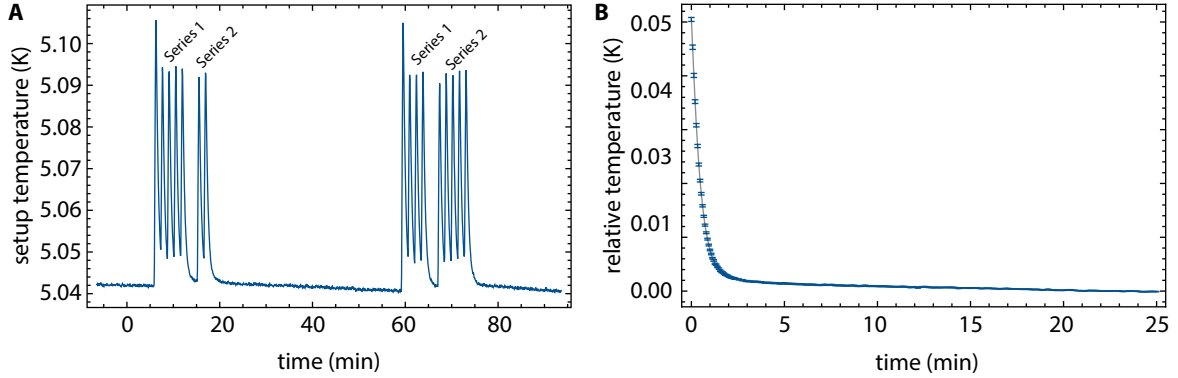


Fig. 7.3: (A) The Larmor drive in the analysis trap leads to significant heating of the setup. The figure shows the temperature of the inner setup measured with a temperature sensor on the 4 K stage of the experiment. Each peak corresponds to the application of a Larmor drive where the first peak is slightly higher during the off-resonant excitation due to the filter setup. (B) The temperature drop after the final spin-flip drive in the AT was averaged over several recorded cycles. $t = 0$ corresponds to the time when the particle is back from the AT.

Figure 7.4 shows the influence of this temperature change on the axial and the modified cyclotron motion. Even 20 min after transporting back to the PT an axial drift is still observable in the PT. The modified cyclotron motion after that time is consistent with a flat line but a drift cannot be excluded. The waiting time of 15 min was chosen to ensure that the frequency measurements are performed in a region where the drifts can be assumed to be linear. This is an important aspect because nonlinear drift contributions in the eigenmotions contributed to the major limitations of the previous g -factor measurement in 2014 [48].

Eventually, the free cyclotron frequency can be calculated by

$$\nu_c^2 = \nu_{+,6}^2 + \nu_{z,\text{eff}}^2 + \nu_-^2, \quad (7.5)$$

where the index of the cycle k is omitted for simplicity. The effective axial frequency $\nu_{z,\text{eff}}$ during the Larmor excitation in the PT (indicated by the red area in figure 7.4) is obtained from a linear fit (red line) to the data $\{\nu_{z,5}, \dots, \nu_{z,8}\}$ which is evaluated at the time t_{Larmor} (red dot) in the center of the Larmor excitation time window. Only the last four axial frequency measurements (shown in the inset) are used for the linear fit. Small residual nonlinear contributions lead to an uncertainty on g of $\Delta g < 1$ ppt. The modified cyclotron frequency is derived by $\nu_{+,6} = \nu_{\text{rf}} + \nu_{l,6} + \nu_{r,6} - \nu_{z,\text{eff}}$ where the two sidebands $\nu_{r/l,6}$ enter that were measured exactly during the Larmor excitation. The magnetron frequency is finally approximated by $\nu_- = \nu_{z,\text{eff}}^2 / (2\nu_{+,6})$. Further possible options to extract $\Gamma^{(k)}$ are discussed later on.

Given all these careful considerations the final resonance is shown in figure 7.5 A. The statistical result in parts per billion (ppb)

$$g = \left(\frac{\Gamma^{(k)}}{g_{\text{CODATA}}} - 1 \right) 10^9 \quad (7.6)$$

is referenced to the present CODATA [90] value $g_{\text{CODATA}} = 5.585\,694\,702(17)$. The combined analysis

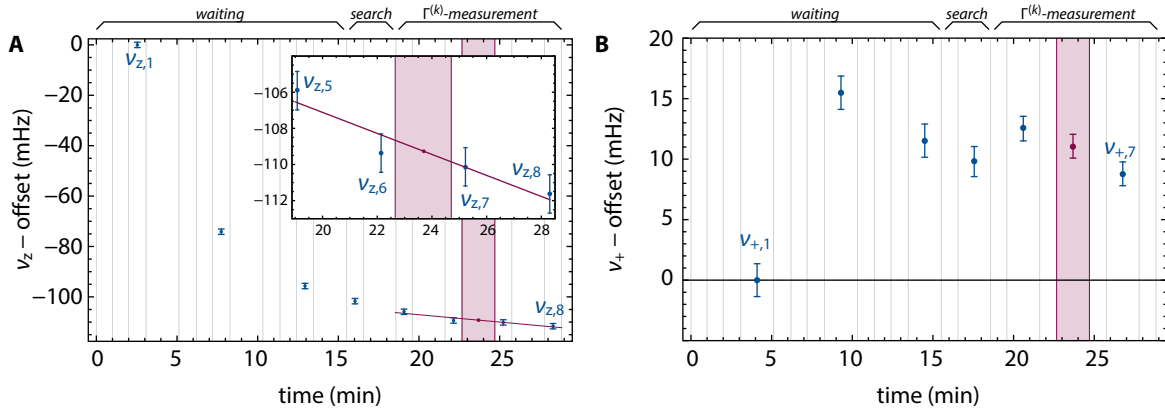


Fig. 7.4: Drift of the axial (A) and modified cyclotron frequency (B) in the PT averaged over all cycles. $t = 0$ corresponds to the time when the particle is back from the AT and the waiting time starts. The vertical lines show the time windows for the different steps during the waiting, search and measurement period. The red line is a linear fit to the last four axial measurements, zoomed on in the inset. The red point is the interpolated value of the axial frequency during the Larmor excitation, indicated by the red shaded area. Together with the modified cyclotron frequency in red the free cyclotron frequency is evaluated.

of all three protons leads to 1264 $\Gamma^{(k)}$ -ratios where all ratios with frequency fit errors in the initial dip spectra were excluded. The distribution is shown in figure 7.5 B, as a result of an uniform distributed randomized scanning convoluted with a normal distribution due to the frequency stability. Finally, the new g-factor result based on the likelihood estimate is

$$\left(\frac{g}{2}\right)_{\text{stat}} = \frac{\mu_{\text{P}}}{\mu_{\text{N}}} = 2.792\,847\,345\,00(75)$$

with a fractional precision of 268 ppt. The standard error mean (s.e.m.) is extracted by maximizing the likelihood function $\mathcal{L}(g_0, A_0, w_0)$ with respect to A_0 and w_0 for fixed values of $g_0 = g_{\text{stat}} - \Delta g$ that are shifted from the ideal value. The result is a nearly quadratic function with argument Δg . The values where the function drops by 1/2 from its maximum value are denoted $\Delta g_1 = -268.15$ ppt and $\Delta g_r = +268.52$ ppt and correspond to the 1σ error. Since the upper and lower error bounds are almost perfectly symmetric the total error is obtained by $\Delta g_{\text{stat}} = (\Delta g_r - \Delta g_1)/2 = 268$ ppt as stated before. In the same manner the errors for A_0 and w_0 can be calculated and are summarized in table 7.1.

To understand the resonance width independent measurements of the cyclotron frequency were performed. During the ω_+ measurement a Larmor drive was applied to ensure a similar situation compared to the actual measurement. The stability of the free cyclotron frequency $\sigma = 40.8(8)$ mHz leads to a theoretical width of 1.41(2) ppb which is in good agreement with the measured resonance width and is the dominant effect for the linewidth.

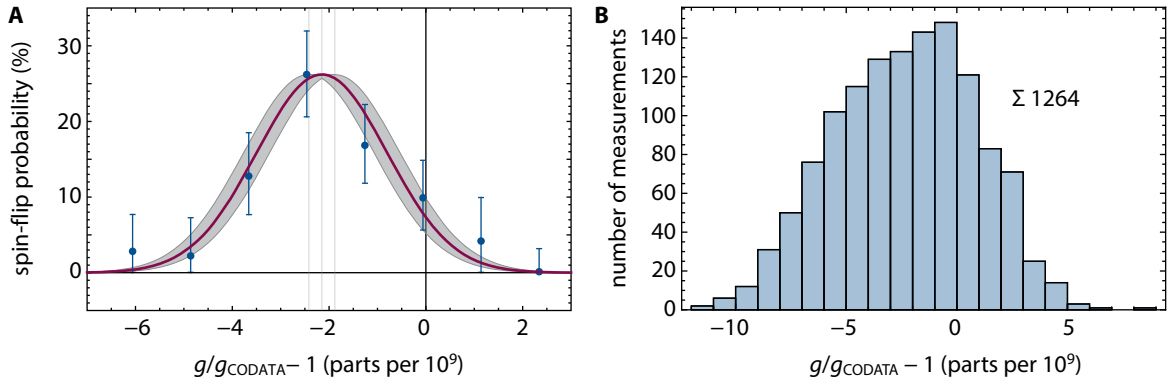


Fig. 7.5: (A) Final statistical g -factor resonance in red with s.e.m. error band on g indicated by the gray area and by the vertical lines. The data points in blue are a representation of the raw data. However, the binned data is for visualization only and is not used for the maximum likelihood estimate. (B) Distribution of performed measurements. The shape roughly corresponds to a uniform distribution convoluted with a normal distribution due to the finite cyclotron stability..

	value	Δ_l	Δ_r	$(\Delta_r - \Delta_l)/2$
g_0 (ppb)	-2.150	-0.268	0.269	0.268
σ_0 (ppb)	1.345	-0.193	0.229	0.211
A_0 (%)	26.21	-4.73	5.31	5.02

Table 7.1: Results of the maximum likelihood estimate relative to the CODATA value. $\Delta_{l/r}$ are the upper and lower boundaries of the s.e.m. The last column shows the average error on the parameter.

7.2.2 Statistical crosschecks

To verify that the used statistical analysis leads to the correct results several statistical crosschecks were performed. These crosschecks are based on Monte-Carlo simulations [91] of the measurement routine that were implemented in *Wolfram Mathematica*. The starting point is the full lineshape [79] with a width based on independent cyclotron frequency stability measurements. During the simulation the true g -factor is a known input parameter. A random number generator picks a $\Gamma^{(k)}$ for each cycle and spin flips are simulated based on the probability $p_{\text{SE,PT}}(\Gamma^{(k)})$ of the lineshape. For each cycle two axial frequency series are simulated based on known noise input parameters for a randomly selected Boltzmann distributed cyclotron energy. The resulting data is then analyzed in the same way as the original data described in section 6.2.3.

As a first consistency check the threshold method is used for comparison. The result relative to the CODATA value is $g_{\text{stat,threshold}} = -2.375(261)$ ppb which agrees with the Bayes approach. This is illustrated in figure 7.6 together with the variation of several other input parameters. Next, the Bayes method is tested for consistency, bias and robustness [92]. The tests were performed for the estimation of g_0 since this is the only critical parameter and e.g. a non-biased result on the width of

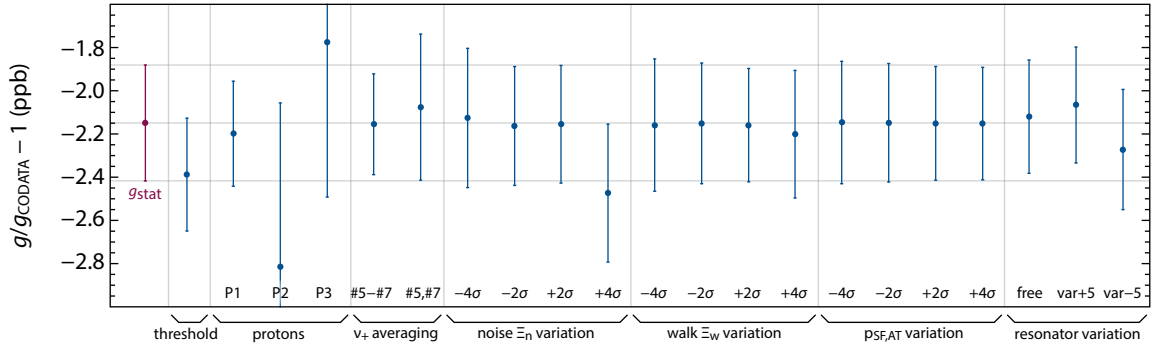


Fig. 7.6: The plot summarizes the results of the statistical analysis for various input parameters and model dependencies. The red data point indicates the finally chosen statistical value for g . P1–P3 show the results of each proton evaluated individually. Further details are discussed in the text.

the resonance has no significant impact.

Robustness describes the reliability of the method to produce the correct result under the assumption that false input parameters were used or false data with outliers was not excluded. To verify the robustness of the analysis the three correlated parameters $\bar{\Xi}_n$, $\bar{\Xi}_w$ and $p_{SF,AT}$ were varied within $\pm 4\sigma$ of their errors, see figure 7.6. The simulations not only show that the g -factor estimate is in perfect agreement with the original value but also that the initial input noise parameters are reproduced well. In addition, even 4σ shifts lead to consistent results.

Consistency means that for an increasing number of data points the result converges to the true value. If \hat{a} is the estimator for the sample than the estimator converges to the true value a_0 for a large number of measurements, $\lim_{n \rightarrow \infty} \hat{a} = a_0$. To test the method for consistency the whole double trap routine was simulated in a Monte-Carlo-simulation with 10^6 data points. The requirement of consistency is fulfilled with an upper bound of 6 ppt limited by the simulation. To reduce it even further a simulation with more data points is required, however, at the current experimental precision this is not necessary.

Bias, not to be confused with consistency, is verified by generating a large number of data sets with fixed sample size. Estimators are obtained for each of these data sets individually. To ensure an unbiased method the expectation value of the distribution of estimators must be equivalent to the true value. 75 000 resonances with 1000 data points each were generated so that a bias can be excluded with an upper bound 1.6 ppt.

The $N = 75\,000$ generated resonances can also be used to check whether the predicted error based on the maximum likelihood estimation result in the correct 68.3% error. To do so, the error on g_0 is individually calculated for each resonance and the expectation value for the distribution of all these errors is computed. This is compared to the width of the normal distributed N values of g_0 . The 1σ width yields the boundaries where 68% of all g_0 values are included. Based on the simulated data it cannot be excluded that the error is slightly overestimated with 71%. In conclusion, the calculated error is a conservative estimate and well suited for the statistical analysis.

Another simulation was performed to assure that cumulated data taking at an off-center position of the resonance does not influence the true estimated value on g_0 (all simulation above were simulated with symmetric data taking around the true value). To that end, the highest data acquisition was shifted by 2 ppb from the true value of g_0 . An effect can be excluded with an upper bound of 5 ppt.

Figure 7.6 shows another important crosscheck – the averaging of ν_+ . As pointed out earlier three measurements of ν_+ in the linear drift region were performed $\nu_{+,5}$, $\nu_{+,6}$ and $\nu_{+,7}$. For the final g-factor evaluation only measurement #6 was used but the resonance can also be evaluated by averaging all three measurements #5 – #7 or averaging #5 and #7. All results are in excellent agreement with each other and the averaging of all three even provides a smaller error due to more information. The reason, however, that only #6 was used for the final evaluation is the cleaner implication for the systematics. If Larmor drive ν_L and modified cyclotron frequency ν_+ are measured exactly simultaneously many systematic effects are greatly suppressed.

The variation of the resonator is a unique property that must be taken into account in the used fit routine for the frequency determination. Since this leads to a systematic error it is discussed in detail in section 7.3.1.

In summary, the techniques demonstrated here to analyze the data present a robust and accurate way to extract an estimate for the true value of the g-factor resonance. All relevant effects that would cause systematic deviations were excluded way beyond the experimental error.

7.3 Systematics

7.3.1 Systematic errors

Systematic corrections on $g = 2\nu_L/\nu_c$ arise due to shifts of the free cyclotron frequency ν_c or the Larmor frequency ν_L and can be calculated by linear error propagation

$$\frac{\Delta g}{g} = \frac{\Delta \nu_L}{\nu_L} - \frac{\Delta \nu_c}{\nu_c} . \quad (7.7)$$

These energy- and time-dependent shifts typically arise from potential or magnetic field imperfections characterized by C_4 and B_2 or higher orders C_n and B_n , as introduced in equation (2.28). In the next sections the individual contributions will be discussed and calculated.

Electrostatic shifts

In order to optimize the electrostatic potential and minimize systematic shifts, the tuning ratio was optimized for each proton with magnetron bursts as discussed in section 4.2 with an uncertainty $\delta TR < 1 \cdot 10^{-5}$.

The systematics based on the electrostatic shift are not accompanied by a systematic shift, only by a systematic uncertainty, because TR was optimized to $C_4 = 0$. To acquire the systematic uncertainty on g the sidebands used to determine ν_+ must be considered. In the case of non-vanishing C_4

all eigenfrequencies will be shifted by $\Delta\omega_+$, $\Delta\omega_z$ and $\Delta\omega_-$, the Larmor frequency, however, is unshifted. To understand how these shifts affect the measured frequencies, the sideband measurement, introduced in section 2.6, is considered:

$$\begin{aligned}\omega_{+, \text{measured}} &= \omega_l + \omega_r - \omega_z + \omega_{\text{rf}} \\ &= \left(\omega_z + \Delta\omega_z - \frac{\delta}{2} - \frac{\Omega_\delta}{2} \right) + \left(\omega_z + \Delta\omega_z - \frac{\delta}{2} + \frac{\Omega_\delta}{2} \right) \\ &\quad - (\omega_z + \Delta\omega_z) + (\omega_+ + \Delta\omega_+ - \omega_z - \Delta\omega_z + \delta) \\ &= \omega_+ + \Delta\omega_+ .\end{aligned}\tag{7.8}$$

This means that the measured modified cyclotron frequency is in fact the shifted frequency $\omega_+ + \Delta\omega_+$. The same argument can be made for the magnetron motion. The axial frequency is measured directly and naturally includes the shift $\Delta\omega_z$. The relative effect of all measured frequencies on the g-factor is described by

$$\frac{\Delta g}{g} = - \frac{\sqrt{(\omega_+ + \Delta\omega_+)^2 + (\omega_z + \Delta\omega_z)^2 + (\omega_- + \Delta\omega_-)^2} - \omega_c}{\omega_c}\tag{7.9}$$

with ω_c the unshifted free cyclotron frequency. All shifts are theoretically well known and written down in equation (2.28). The energies can be related to the temperature T_z of the axial detection system $\langle E_+ \rangle = k_B \frac{\omega_+}{\omega_z} T_z$, $\langle E_z \rangle = k_B T_z$ and $\langle E_- \rangle = -k_B \frac{\omega_-}{\omega_z} T_z$. Together with $C_4 = E_4 + D_4(TR_{\text{id}} + \Delta TR) = D_4 \Delta TR$ this leads, in the case of the modified cyclotron frequency for example, to

$$\frac{\Delta\omega_+}{\omega_+} = \frac{1}{qV_0} \frac{k_B D_4 T_z \Delta TR}{C_2^2} \left(\frac{3}{4} \left(\frac{\omega_z}{\omega_+} \right)^4 \frac{\omega_+}{\omega_z} - \frac{3}{2} \left(\frac{\omega_z}{\omega_+} \right)^2 + 3 \left(\frac{\omega_z}{\omega_+} \right)^2 \frac{\omega_-}{\omega_z} \right).\tag{7.10}$$

Since the product $D_4 T_z$ was directly measured (section 4.4), this shift, as well as the axial and the magnetron frequency shift, can be calculated. To account for the measurement uncertainties full correlation between $D_4 T_z$ and TR_{id} is assumed which is why the expression is evaluated at $D_4 T_z + \delta D_4 T_z$ and $\Delta TR = \delta TR$. The final systematic uncertainty due the trapping potential is $\delta g/g = 9$ ppt.

Magnetic field

Systematics due to the magnetic field scale with the two parameters $B_{1,\text{PT}}$ and $B_{2,\text{PT}}$. These are the linear and quadratic field components due to the magnetic bottle in the analysis trap. Corrections based on $B_{1,\text{PT}}$ arise if the cyclotron and Larmor frequency are measured at different energies, which cause different center points of their motion. Consequently, the shifted motional center points result in different magnetic fields during both measurements in a linear field gradient. During the g-factor measurement the sideband measurement for the free cyclotron measurement and the Larmor excitation were executed in parallel which ensures the same energy and same magnetic field. Thus, only systematic effects based on $B_{2,\text{PT}}$ must be taken into account.

The relative shift on g in the presence of a quadratic inhomogeneity is described by

$$\frac{\Delta g}{g} = \frac{\Delta\omega_L}{\omega_L} - \frac{\sqrt{(\omega_+ + \Delta\omega_+)^2 + (\omega_z + \Delta\omega_z)^2 + (\omega_- + \Delta\omega_-)^2} - \omega_c}{\omega_c}\tag{7.11}$$

with $\Delta\omega_{L/+/-}$ from equation (2.28). As usual the energies are replaced with the detection system temperature $T_z = 13.6(8.1)$ K and the respective frequency ratios. This leads to a systematic shift of $\Delta g/g = -8(4)$ ppt where the error is due to the error of the temperature measurement.

Relativistic shift

Due to the relativistic mass increase both the cyclotron and Larmor frequency are shifted. These shifts [51] lead to a relative shift on g

$$\frac{\Delta g}{g} = -\frac{1}{mc^2} \left(\frac{2}{9} \langle E_+ \rangle - \langle E_+ \rangle \right) \quad (7.12)$$

which contributes with 44(26) ppt. The other modes were not included since they have a negligible contribution.

Image charge

A particle in a Penning trap induces image charges on the electrode surfaces. These image charges lead to a back action on the particle due to a modified potential. Due to the cylindrical symmetry of the trap the modified potential will only affect the radial eigenfrequencies. This effect is calculated in [93]

$$\Delta\omega_{\pm} \approx \mp \frac{q^2}{4\pi\epsilon_0 m r_0^3 \omega_c} \quad (7.13)$$

with the trap radius r_0 for an infinite cylinder without any slits. The value of r_0 is obtained by calculating the radius from the room temperature value a with the integrated thermal expansion coefficient [94] $r_0 = \alpha_{\text{Cu}} a = 1.0033^{-1} \times 3.5 \text{ mm} = 3.488 \text{ mm}$. The measured value of $C_2 = 31\,127(20) \text{ m}^{-2}$ is used to estimate how well this radius is fulfilled. This C_2 is theoretically expected for a trap radius of $r_{\text{th}} = 3.469 \text{ mm}$. By conservatively estimating the error from the C_2 prediction the radius is $r_0 = 3.488(30) \text{ mm}$ and can be used to calculate the relative shift on g

$$\frac{\Delta g}{g} = -\frac{\sqrt{(\omega_+ + \Delta\omega_+)^2 + \omega_z^2} + (\omega_- + \Delta\omega_-)^2 - \omega_c}{\omega_c} = 98(3) \text{ ppt} . \quad (7.14)$$

The image charge shift is the major systematic shift for the final result.

Fit routine limitations

In section 4.6 the fitting algorithm to extract the motional frequencies was discussed in detail. It was pointed out, that a centered particle with respect to the resonator frequency is highly important as is the knowledge of the resonator frequency. The resonator frequency drifts during each cycle similar to the drift of the eigenfrequencies. This effect is shown in figure 7.7 A and was measured with four resonance spectra at different times of the cycle. Two of these measurements were averaged to estimate for resonator frequency of each cycle, compare figure 7.7 B. The data is sufficient to pin down the resonator frequency with a resolution of $< 1 \text{ Hz}$. Furthermore the total variation is confined within $\pm 2 \text{ Hz}$.

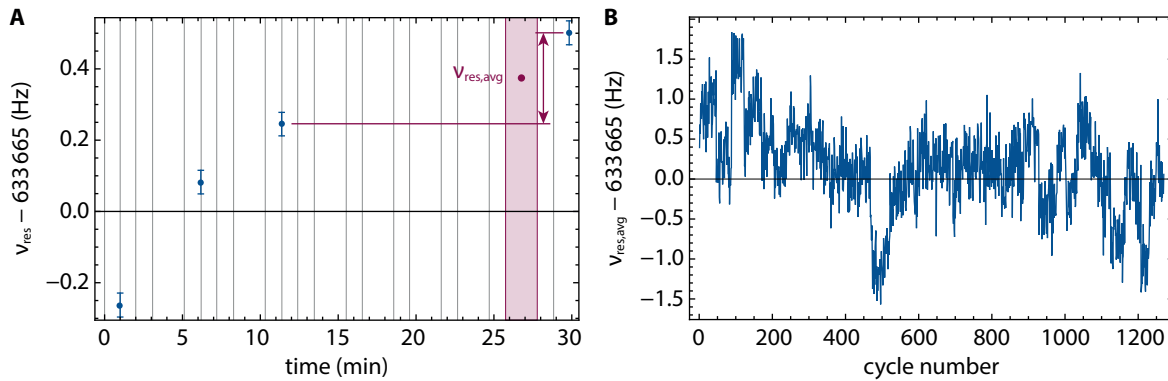


Fig. 7.7: (A) The resonator frequency was measured four times during each cycle. The blue points represent the average behavior over all cycles. A drift of the resonator frequency can be observed due to thermal effects similar to the eigenfrequencies. The measurements 3 and 4 of each cycle are used to estimate the resonator frequency with $v_{\text{res,avg}}$. (B) The plot shows the evolution of the estimated resonator frequency $v_{\text{res,avg}}$ as a function of the cycle number. The resonator frequency was stable to within ± 2 Hz.

With the resonator frequency of each cycle at hand this can be used as input parameter to the fit routine, where the resonator frequency is fixed to the independently measured value. To estimate the impact on the g -factor the result of a fixed input resonator frequency can be compared to the case where the resonator frequency is kept as a free parameter. Furthermore, the g -factor was also calculated for fixed resonator frequencies deliberately shifted by ± 5 Hz. The results are shown in figure 7.6 at the right hand side under resonator variation. The difference between the fixed and the free case is 29 ppt, an order of magnitude lower than the statistical uncertainty. From the manually shifted frequencies the effect on the g -factor is limited to 21 ppt Hz^{-1} .

This bound was also verified with an independent measurement of the free cyclotron frequency where the dips were centered with respect to the resonator frequency and subsequently detuned ± 5 Hz. The measured difference in the cyclotron frequency corresponds to a shift on g -factor of $17(10) \text{ ppt Hz}^{-1}$ which is in good agreement with the result obtained by the fit routine. Together with the result of the total resonator variation a systematic uncertainty of $\delta g/g = 80 \text{ ppt}$ is added to the final result.

Summary

The systematic corrections are summarized in table 7.2. A total shift of $133(123) \text{ ppt}$ must be corrected on the statistical g -factor. The error was conservatively estimated by the sum of all individual errors. This also accounts for correlations between errors and results that were not obtained through a statistical measurement.

name	shift $\Delta g/g$ (ppt)	error $\delta g/g$ (ppt)
electrostatic	0	9
B_2	8	4
relativistic	-44	26
image current	1	1
image charge	-98	3
fitting	0	80
Σ	-133	123

Table 7.2: Summary of systematic corrections that must be applied to the statistical g-factor result. The total error is obtained by summing up all individual errors to account for correlations and non statistical results.

7.3.2 Systematic crosschecks

This section discusses several crosscheck measurement that did not contribute to the final systematics of this g-factor measurement but can be of potential interest for future measurements.

Axial energy variation during double and single dip

It cannot be initially guaranteed that the same conditions are present for a single dip measurement and a double dip measurement since the rf-drive during the double dip can have an influence on the experimental conditions. For example, in the analysis trap the spin-flip drive has a significant effect on the temperature of the whole experimental setup due to its high-power dissipation.

Figure 7.8 A shows two averaged spectra of all single and double dipoles recorded during the g-factor measurement. A shift of $\Delta S/N_{\log} = 0.158(4)$ dB is observable on the background. However, the data is not sufficient to say whether the signal-to-noise ratio changed or the resonator spectrum as a whole increased due to an overall increase in the background noise level. Assuming that the signal-to-noise has changed the S/N difference can be related to an effective temperature change of the resonator

$$S/N_{\log} + \Delta S/N_{\log} = 10 \log_{10} \left[\frac{\left(\sqrt{4k_B(T_z + \Delta T_z)} R_{\text{eff}} \Delta \nu \kappa \right)^2 + u_n^2}{u_n^2} \right], \quad (7.15)$$

where $S/N_{\log} = 19.6(5)$ dB is the static signal-to-noise ratio. κ is the coupling factor of the axial detector and the effective input noise of the amplifier u_n is calculated from $\Delta S/N_{\log} = 0 = \Delta T_z$. This means that a S/N change of 0.158(4) dB can be related to a change in temperature of 500(20) mK.

Due to the thermal coupling of the axial mode to the axial resonator it can't be excluded that the axial energy is different between single and double dipoles. The axial frequency, however, does not depend on the axial energy since B_2 does not lead to such a dependency (equation (2.28)) and C_4 was optimized to zero. The effect of a non-zero C_4 is already included in the systematics with an error estimate far larger than the measured effect here.

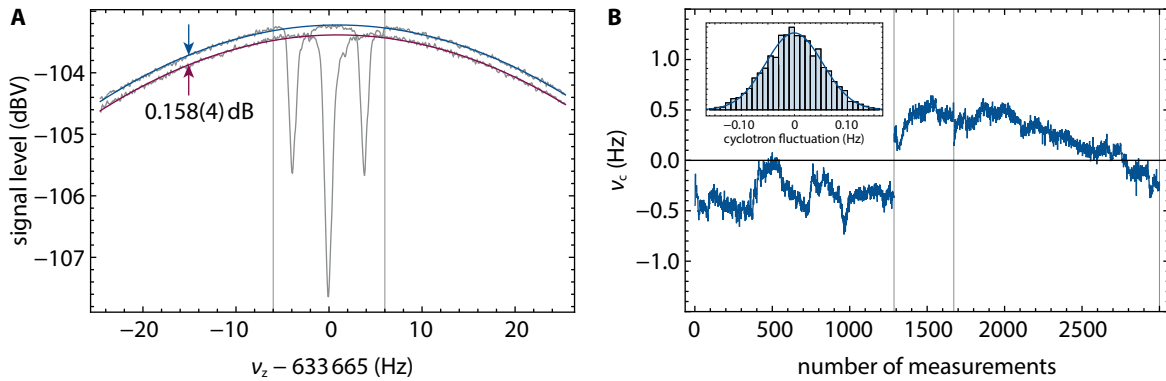


Fig. 7.8: (A) All axial and double dip spectra used for the g -factor resonance were averaged. The background is fit with a quadratic polynomial with the dip areas between the gray vertical lines excluded. The average difference between both backgrounds is 0.158(4) dB. (B) The cyclotron frequency was continuously measured by subsequent single and double dip measurements. The vertical lines show where the measurement routine was paused for filling. The double dips were alternately driven with amplitudes of -12 dBm (as in the g -factor measurement) and -24 dBm. The difference between both amplitudes is consistent with zero $-2(48)$ ppt. The small inset shows the overall distribution of the free cyclotron fluctuations $\nu_{c,i} - \nu_{c,i+1}$ with a standard deviation of 53(3) mHz.

Power splitting

During a double dip measurement an rf-drive is applied. *Power splitting* refers to the problem that different drive amplitudes might result in different measured frequencies and only the limit for small amplitudes converges to the true value. To test whether the drive amplitude of -12 dBm during the g -factor measurement had an influence on the measured frequency, the measurement sequence $\nu_z \rightarrow \nu_+(-12\text{dBm}) \rightarrow \nu_z \rightarrow \nu_+(-24\text{dBm})$ is conducted with two different drive amplitudes. This allows the continuous logging of the free cyclotron frequency ν_c at two different amplitudes. The result is shown in figure 7.8 B. The difference $-2(48)$ ppt between both amplitudes is consistent with zero.

Larmor dynamic

It must also be checked whether the application of the Larmor drive either has influence on the modified cyclotron frequency or the measurement of the axial frequency similar to the analysis trap. For that purpose a continuous axial series is recorded with an applied Larmor drive during every other spectrum. The difference between both measured axial frequencies is $-0.9(1.4)$ mHz. Applied to the g -factor this leads to a contribution of $-1.8(2.9)$ ppt and is negligible.

A similar measurement is conducted for the determination of ν_+ . During every other double dip the Larmor drive is applied. Once again the result is consistent with zero 3(62) ppt and even if a shift were observable this has no impact on the g -factor since the Larmor frequency is measured in parallel with ν_+ .

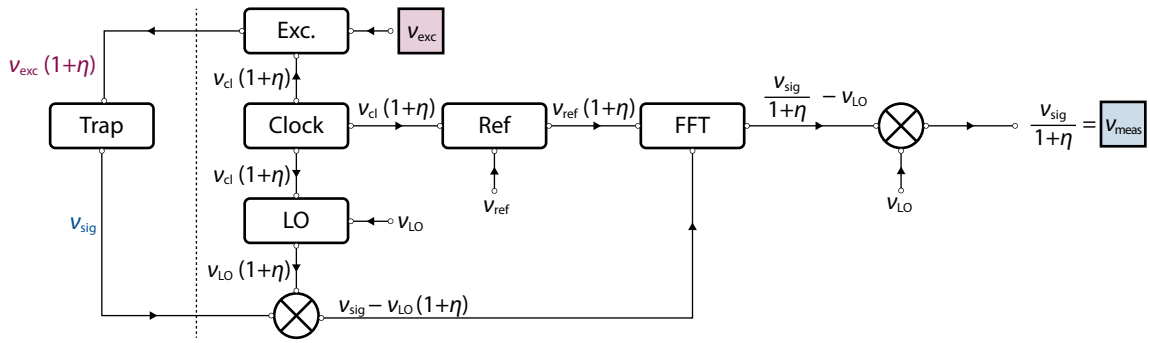


Fig. 7.9: All instruments in the experiment are referenced to a Rubidium frequency standard. Assuming that the frequency standard has a relative unknown error η the measured frequencies v_{meas} are changed. The same applies for any excitation signal that is applied to the trap.

Magnetron frequency

The magnetron frequency is not measured continuously throughout the measurement sequence but approximated through $\omega_- \approx \frac{\omega_z^2}{2\omega_+}$ which is not correct for a misaligned or elliptical trap. A comparison of the calculated and the directly measured magnetron frequency [51] via sideband coupling

$$\omega_{-,meas} \approx \omega_{-,calc} \left(1 - \frac{3}{2} \sin^2 \theta \right) \quad (7.16)$$

yields a misalignment of $\theta < 0.5^\circ$ which corresponds to < 3 ppt.

External reference

In order to provide a precise and accurate g-factor measurement all instruments are referenced to an external FS725 Rubidium 10 MHz frequency standard. The short term stability of the frequency standard is $< 2 \times 10^{-11}$ and presents no limitation for the setup. The standard is, however, affected by aging and the absolute output frequency of 10 MHz can change over time. Due to the ratio measurement between cyclotron and Larmor frequency this of no concern and any offset cancels in the ratio as shall be shown next.

Based on figure 7.9 a reference clock that oscillates at $v_{cl}(1+\eta)$ with $\eta \neq 0$ is assumed, where η is the relative deviation of the clock frequency. The detuned clock frequency affects all excitations applied to the trap as well as the frequency detection. For an excitation the frequency that is typed in the instrument v_{exc} deviates by a factor of $1+\eta$ from the signal that is seen by the particle in the trap. In case of the frequency detection the real particle frequency is denoted v_{sig} . In the experiment an SR780 Network Signal Analyzer to record all spectra is used. This analyzer has an input range between 0 and about 100 kHz. From the factory it does not support an external reference. Instead a homemade modification is used where the build-in crystal oscillator signal at $v_{ref} = 30.933$ MHz is replaced with a square signal of a frequency generator which itself is referenced to the clock. To

match the particle signal to the input range, the frequency is down-mixed with a local oscillator (LO). The resulting signal $\nu_{\text{sig}} - \nu_{\text{LO}}(1 + \eta)$ is read out with the analyzer. If $\eta > 0$ ($\eta < 0$) the internal analyzer clock is running too fast (slow) and the measured signal will be measured by a factor of $1 + \eta$ smaller (larger) than it actually is $\nu_{\text{sig}}/(1 + \eta) - \nu_{\text{LO}}$. In the final step the initial LO frequency is added to obtain the measured frequency

$$\nu_{\text{meas}} = \frac{\nu_{\text{sig}}}{1 + \eta} . \quad (7.17)$$

Applied to the the case of the axial frequency this result immediately yields

$$\nu_{z,\text{meas}} = \frac{\nu_z}{1 + \eta} . \quad (7.18)$$

In the case of the modified cyclotron frequency the sidebands are affected by the detuned clock as well,

$$\nu_{+,\text{meas}} = \frac{\nu_l}{1 + \eta} + \frac{\nu_r}{1 + \eta} - \frac{\nu_z}{1 + \eta} + \nu_{\text{rf}} , \quad (7.19)$$

while the true frequency is

$$\nu_{+} = \nu_l + \nu_r - \nu_z + \nu_{\text{rf}}(1 + \eta) , \quad (7.20)$$

where the rf-drive frequency was corrected according to the arguments made for excitations with a detuned clock. Combining both equations, this results in

$$\nu_{+,\text{meas}} = \frac{\nu_{+}}{1 + \eta} \quad (7.21)$$

and likewise for the magnetron frequency. Thus, the measured cyclotron frequency based on the invariance theorem scales the same as all individual frequencies

$$\nu_{c,\text{meas}} = \frac{\nu_c}{1 + \eta} . \quad (7.22)$$

Finally, the Larmor excitation is taken into account. To excite the particle in the trap with the frequency ν_L an excitation at $\nu_{\text{exc}} = \nu_L/(1 + \eta)$ is required. The ratio the particle “sees” is then ν_c/ν_L and is based on the cyclotron measurement $\nu_{c,\text{meas}}$ and the excitation frequency ν_{exc}

$$\frac{\nu_{c,\text{meas}}}{\nu_{\text{exc}}} = \frac{\nu_c}{1 + \eta} \frac{1 + \eta}{\nu_L} = \frac{\nu_c}{\nu_L} \quad (7.23)$$

in perfect accordance with the real ratio. Clock drifts η are thus completely irrelevant for a g-factor measurement

However, it must be ensured that the FFT measures a self-consistent input signal by calibrating the signal from the frequency generator that is used as external reference for the 30.933 MHz. The deviation of a 100 kHz test signal at a span of 195.3 mHz with an acquisition time ≈ 4 ks is zero with an error of 8.2 μ Hz. This corresponds to an upper limit for a shift on g of < 0.28 ppt and is completely negligible.

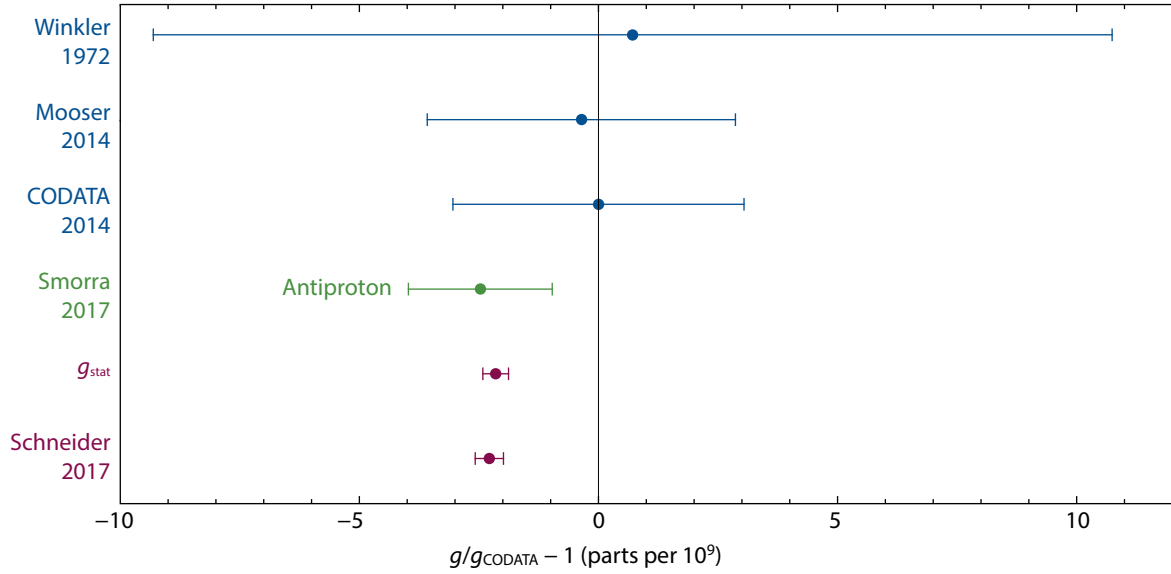


Fig. 7.10: Historic overview of proton g -factor measurements starting with an indirect measurement of Winkler *et al.* [37] from 1972. The recent measurement [50] presented in this thesis is shown in red. g_{stat} is the statistical result with no systematic corrections. The green data point represents the currently best antiproton g -factor measurement at CERN [49].

7.3.3 Final result

The final result of the g -factor measurement based on the statistical value g_{stat} and all systematic corrections is

$$\left(\frac{g}{2}\right)_{2017} = \frac{\mu_{\text{P}}}{\mu_{\text{N}}} = 2.792\,847\,344\,62(75)(34)$$

where the first parenthesis indicates the 68.3% statistical error and the second the systematic. The measurement has a total fractional precision of 295 ppt and improves the previous g -factor measurement [48] by a factor of more than 11. The new value is consistent with the current CODATA value [90], but 10 times more precise. Figure 7.10 illustrates historic g -factors in comparison to this measurement. The value is also consistent with the latest antiproton g -factor measurement [49]. The proton g -factor which has been determined in this thesis can thus be used for an improved test of CPT invariance in the baryon sector.

7.4 Improved CPT Test in the baryonic sector

The improved proton g -factor of this work allows for an improved CPT test in the vector sector by comparing protons and antiprotons. Together with the result of the antiproton [49] new constraints

can be set on parameters of the *Standard Model Extension* (SME) [21]. The SME is a framework which is used to study Lorentz and CPT violating terms within an effective field theory. This extension of the Standard Model is a test model that shows the sensitivity of measurable quantities with respect to CPT violation, but does not relate the introduced CPT odd bi-linear operators to any more fundamental physics mechanisms. The effective field theory is built with Lorentz-violating operators combined with coefficients that define their strength. These coefficients are constrained by numerous experiments that e.g. look for time dependent variations of fundamental constants or that compare properties of matter and antimatter systems [20].

Based on [49] the combined result of antiproton and proton g -factor (95% CL)

$$\left(\frac{g_P}{2} - \frac{g_{\bar{P}}}{2}\right) = 5(74) \times 10^{-10} \quad (7.24)$$

shows that CPT invariance is preserved at the current level of precision. In order to constrain CPT-odd b coefficients within the SME the theoretical description in [21] and the application for the proton/antiproton case [46] is used. The g -factor difference introduced above can be rewritten as

$$\left(\frac{g_P}{2} - \frac{g_{\bar{P}}}{2}\right) = \frac{2}{\omega_c^P \omega_c^{\bar{P}}} \left(\Sigma \omega_c^P \Delta \omega_a^P - \Delta \omega_c^P \Sigma \omega_a^P\right) \quad (7.25)$$

which uses the abbreviations

$$\Delta \omega_c^P = \frac{1}{2} \left(\omega_c^P - \omega_c^{\bar{P}}\right) \quad \Delta \omega_a^P = \frac{1}{2} \left(\delta \omega_a^P - \delta \omega_a^{\bar{P}}\right) \quad (7.26)$$

and

$$\Sigma \omega_c^P = \frac{1}{2} \left(\omega_c^P + \omega_c^{\bar{P}}\right) \quad \Sigma \omega_a^P = \frac{1}{2} \left(\delta \omega_a^P + \delta \omega_a^{\bar{P}}\right) . \quad (7.27)$$

These expressions use the cyclotron frequency of the proton ω_c^P and the antiproton $\omega_c^{\bar{P}}$. $\delta \omega_a^P$ and $\delta \omega_a^{\bar{P}}$ are the differences in the anomaly frequencies due to possible CPT violation, where the anomaly frequency is defined by $\omega_a = \omega_L - \omega_c$. It can be shown [21], that differences in $\Delta \omega_c^P$ are, to leading order, not caused by possible CPT-violation and any non-vanishing difference is due to different magnetic fields.

In order to make different experiments comparable the same coordinate system, the *sun-centered frame*, is used. The apparatus coordinates x^a are connected to the sun-centered coordinates X^J by

$$x^a(T_{\oplus}) = R^{aj} R^{jJ} (T_{\oplus}) X^J . \quad (7.28)$$

The 3×3 matrix R^{aj} relates the apparatus coordinates to the laboratory coordinates using three Euler rotations with α, β and γ . The 3×3 matrix R^{jJ} which transforms to the sun-centered frame is a function of the co-latitude χ and of the local sidereal time T_{\oplus} (for an explicit form refer to [21]). This transformation is used to transform single-index laboratory frame coefficients (\tilde{b}_p^3) as well as multi-index coefficients ($\tilde{b}_{F,p}^{33}$).

The two experiments operated by the BASE collaboration are located in Mainz and at CERN have a co-latitude of $\chi_M = 40^\circ$ and $\chi_C = 44^\circ$, respectively. The laboratory frame is defined with x along

coefficient	constraint old	constraint new
$ \tilde{b}_p^Z $	$< 1.8 \times 10^{-24} \text{ GeV}$	$< 6.9 \times 10^{-25} \text{ GeV}$
$ \tilde{b}_p^{XX} + \tilde{b}_p^{YY} $	$< 1.1 \times 10^{-8} \text{ GeV}^{-1}$	$< 3.9 \times 10^{-9} \text{ GeV}^{-1}$
$ \tilde{b}_p^{ZZ} $	$< 7.8 \times 10^{-9} \text{ GeV}^{-1}$	$< 3.3 \times 10^{-9} \text{ GeV}^{-1}$
$ \tilde{b}_p^{*Z} $	$< 3.5 \times 10^{-24} \text{ GeV}$	$< 1.3 \times 10^{-24} \text{ GeV}$
$ \tilde{b}_p^{*XX} + \tilde{b}_p^{*YY} $	$< 7.4 \times 10^{-9} \text{ GeV}^{-1}$	$< 2.8 \times 10^{-9} \text{ GeV}^{-1}$
$ \tilde{b}_p^{*ZZ} $	$< 2.7 \times 10^{-8} \text{ GeV}^{-1}$	$< 1.0 \times 10^{-8} \text{ GeV}^{-1}$

Table 7.3: Constraints at 95% based on the proton and antiproton magnetic moment measurement in 2017. The old constraints were limited by the precision of the previous proton measurement.

the North-South direction and y along West-East. Both experiments have a horizontal bore which is oriented with respect to the local x -axis with $\gamma_M = -162^\circ$ and $\gamma_C = 120^\circ$. Both magnets are operated at $B \approx 1.9 \text{ T}$ which makes them ideal candidates to be compared. The measurement time for both g -factor runs is long compared to the period of a sidereal day with 23 h 56 min and time variations of the measured quantities can be neglected. Using the experimental parameters and the transformation to the sun-centered frame this finally leads to the two relevant frequency shifts

$$\begin{aligned}
\Sigma\omega_a^p &= \left[\underbrace{\tilde{b}_p^x - \tilde{b}_{F,p}^{xx} B}_{\text{proton}} \right] + \left[\underbrace{\tilde{b}_p^{*z} - \tilde{b}_{F,p}^{*zz} B^*}_{\text{antiproton}} \right] \\
&= \left[\tilde{b}_p^Z \sin(\chi_M) \cos(\gamma_M) + \frac{1}{2} \left(\tilde{b}_{F,p}^{XX} + \tilde{b}_{F,p}^{YY} \right) B \left(\cos^2(\chi_M) \cos^2(\gamma_M) + \sin^2(\gamma_M) \right) \right. \\
&\quad \left. + \tilde{b}_{F,p}^{ZZ} \sin^2(\chi_M) \cos^2(\gamma_M) \right] + \left[\tilde{b}_{F,p}^{*ZZ} \sin^2(\chi_C) \cos^2(\gamma_C) \right. \\
&\quad \left. + \tilde{b}_p^{*Z} \sin(\chi_C) \cos(\gamma_C) + \frac{1}{2} \left(\tilde{b}_{F,p}^{*XX} + \tilde{b}_{F,p}^{*YY} \right) B^* \left(\cos^2(\chi_C) \cos^2(\gamma_C) + \sin^2(\gamma_C) \right) \right] \quad (7.29)
\end{aligned}$$

and likewise for $\Delta\omega_a^p$ with a negative sign between the two square brackets. The left hand side in equation (7.29) is measured experimentally and the right hand side can be expressed as a function of SME coefficients. Thus, the experimental uncertainty can be used to apply constraints to the coefficients. Note that constraining each coefficient individually assumes that at the same time all other coefficients vanish, which is a typical procedure for such an analysis. The result is shown in table 7.3 in a comparison to the previously best constraints [49].

The energy resolution in the b -coefficients can be compared to similar experiments. The measurement of the muon magnetic moment [28] sets constraints at the level of $< 10^{-23} \text{ GeV}$ to $< 10^{-24} \text{ GeV}$. Other experiments with electrons and positrons [27] applies constraints at a level of $< 7 \times 10^{-24} \text{ GeV}$ to $< 6 \times 10^{-25} \text{ GeV}$. The improved measurement of the proton magnetic moment in this work allowed the constraints to be improved by a factor of about 2.7. Provided the techniques utilized at Mainz are applied to the antiproton a CPT test with an energy resolution of $< 4 \times 10^{-25} \text{ GeV}$ in the baryonic sector will be possible.

Chapter 8

Antiproton-to-Proton Charge-to-Mass Ratio

This chapter summarizes the results of the antiproton-to-proton charge-to-mass ratio measurement published in *Nature* [95] by the BASE collaboration at CERN. The data taking was during the beam-time in 2014. The trap layout of this experiment as well as one detection system were developed over an extended time period [78]. The measurement is based on the comparison of cyclotron frequencies between proton and antiproton and thus presents another stringent and direct test of the fundamental CPT symmetry in the baryonic sector.

8.1 Experimental setup

The relevant trap section for the q/m -ratio measurement is illustrated in figure 8.1 and consists of two five-pole traps with a diameter of 9 mm. The measurement trap (MT) is used for the high-precision measurement of the free cyclotron frequency and the reservoir trap (RT) for the long-time storage of antiprotons [77]. The RT can provide antiprotons, independent of CERN's duty cycle, in case of particle loss.

The antiprotons are acquired by an on-axis antiproton beam at an energy of 5.3 MeV provided by the CERN *Antiproton Decelerator* (AD) [96]. Each "shot" contains about 3×10^7 antiprotons which enter the pinched-off trap chamber through a degrader structure made of copper meshes, aluminium and stainless steel foil. As a consequence, the antiprotons are slowed down with an energy distribution peaking at around 200 – 300 keV. The downstream high-voltage (HV2) electrode is used to capture antiprotons with energies below 1 keV. The upstream HV electrode is subsequently ramped up, triggered by the injection pulse to capture the on HV2 reflected antiprotons. Prior to the injection electrons are loaded to the MT by an electron gun. These allow an efficient cooling of the antiproton's axial mode by Coulomb interaction and subsequent radiative cyclotron cooling of the light particles.

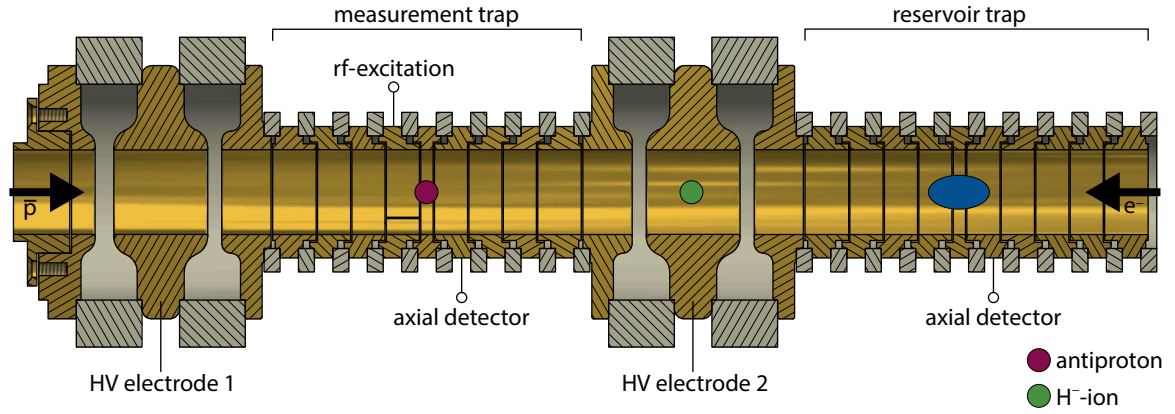


Fig. 8.1: The BASE Penning-trap system for the charge-to-mass ratio comparison measurement contains the measurement and the reservoir trap. The first is used for the high-precision measurement of ω_c while the latter is an antiproton reservoir in case of particle loss. The antiproton beam enters from the left and is captured between the two HV electrodes.

Once a cold cloud of antiprotons, typically several 100, is stored in the MT the particles are shuttled to the reservoir trap where they can be stored for months. The RT was recently used to give an improved constraint on the directly measured antiproton lifetime [97].

Both traps are equipped with axial detectors to measure the axial frequency. The measurement trap has a segmented correction electrode to allow for quadrupole excitation. Using the technique of sideband coupling, section 2.6, the frequencies ω_{\pm} are measured and yield the free cyclotron frequency ω_c by the invariance theorem [52].

To compare the proton q/m ratio to that of the antiproton both free cyclotron frequencies must be measured in quick succession to ensure that the magnetic field is the same and cancels in the ratio

$$R_{\bar{p}p} = \frac{\omega_{c,\bar{p}}}{\omega_{c,p}} = \frac{(q/m)_{\bar{p}}}{(q/m)_p} . \quad (8.1)$$

However, it proves advantageous to use an H^- ion instead of a bare proton because this allows to store both negatively charged species in almost exactly the same trap configuration without the necessity to switch the polarity. Any systematic positional shift due to a switch in polarity is greatly suppressed with the choice of an H^- ion. Furthermore, an H^- ion presents no limitation at the current level of precision because its mass is very well known

$$m_{H^-} = m_p \left(1 + 2 \frac{m_e}{m_p} + \frac{\alpha_{\text{pol},H^-} B_0^2}{m_p} - \frac{E_{\text{bin}}}{m_p} - \frac{E_{\text{aff}}}{m_p} \right) \quad (8.2)$$

with the electron mass m_e [56], the polarizability shift $\alpha_{\text{pol},H^-} B_0^2$ [98], the binding energy E_{bin} [99] and the electron affinity of hydrogen E_{aff} [100]. The new theoretical ratio in case CPT is conserved is

$$R_{\bar{p}H^-} = \frac{\omega_{c,\bar{p}}}{\omega_{c,H^-}} = \frac{(q/m)_{\bar{p}}}{(q/m)_{H^-}} = 1.001\,089\,218\,754(2) \quad (8.3)$$

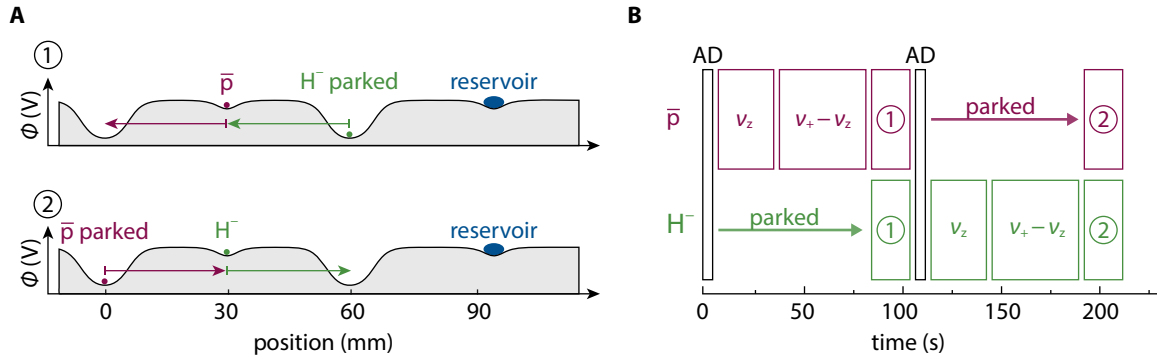


Fig. 8.2: (A) ① and ② show the two different potential configurations in the trap setup. During ① the antiproton is stored in the measurement trap, while the H^- ion is parked in one of the HV electrodes. After the transport of both particles H^- is measured ② while \bar{p} is parked. The reservoir is unaffected by the routine. (B) Each ω_c measurement is started by the AD trigger. The free cyclotron frequency is then determined by measuring a single and a double dip spectrum. Afterward, the particles are transported according to the potential configuration in (A).

and was limited at the time of the measurement by the accuracy of the proton mass [101]. Currently the proton mass is known by a factor of three more precise [57].

To measure $R_{\bar{p}H^-}$ the scheme illustrated in figure 8.2 is used. A measurement of the antiproton free cyclotron frequency starts with the AD trigger for the injection of antiprotons from the proton synchrotron into the AD target area. $\omega_{c\bar{p}}$ is then measured by the determination of ν_z with a single dip and $\nu_{r/1}$ with a double dip which allows the calculation of ν_+ . The magnetron frequency is obtained by $\nu_- = \nu_z^2 / (2\nu_+)$. During the measurement of the antiproton the H^- ion is stored in one of the HV electrodes. Next, the antiproton is transported to the other HV electrode while the H^- is transported to the measurement trap. Again starting with the AD trigger ω_{cH^-} is measured the same way as before. A single ratio measurement can thus be obtained within typical 220 – 240 s. This is about a factor of 60 times faster than earlier experiments for the charge-to-mass ratio [102].

The reason to trigger the measurement with respect to the AD cycle time is the background magnetic field. The deceleration process to slow antiprotons from 3.6 GeV to 5.3 MeV requires several magnetic field changes which are seen by the experiment at a level of 300 nT, which corresponds to relative cyclotron frequency variation at the level of 10^{-7} . An untriggered measurement would thus be limited by a fluctuating background field where the magnetic field of \bar{p} and H^- vary. The triggered measurement ensures that the ω_c measurements are conducted at a similar magnetic field, which is independently monitored by magnetic field sensors.

8.2 Results

During a time period of 35 days a number of 6 521 frequency ratios were measured. To account for small magnetic field drifts the free cyclotron frequencies are interpolated between subsequent

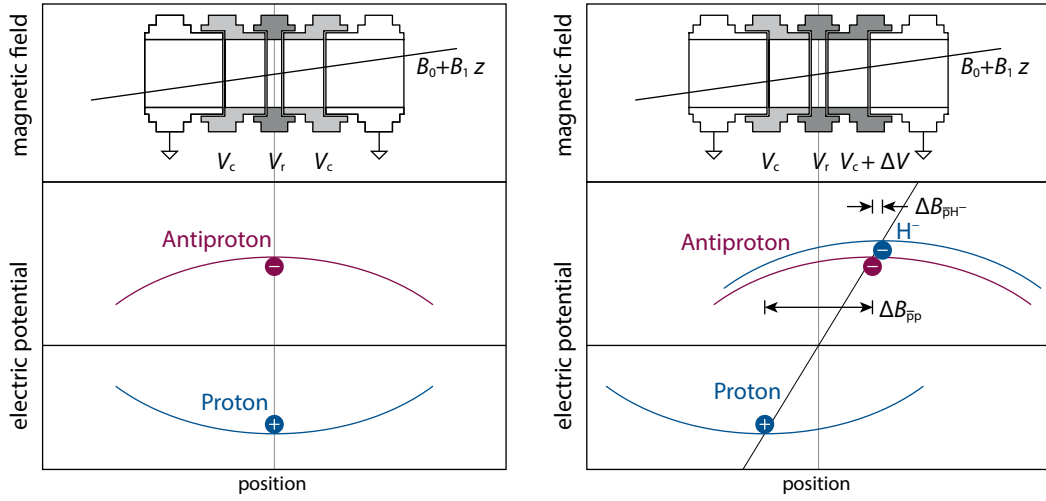


Fig. 8.3: The left side shows the ideal case in the presence of no trap asymmetries. Switching the polarity has no effect on the position of the particles and both ω_c are measured at the same magnetic field. The right side shows the case with a voltage offset ΔV on one correction electrode. A polarity switch leads to different axial positions of \bar{p} and p , which causes magnetic field difference $\Delta B_{\bar{p}p}$. The H^- drastically reduces this effect $\Delta B_{\bar{p}H^-} \ll \Delta B_{\bar{p}p} \neq 0$, because no polarity switch is required. However, offsets are not negligible and must still be characterized carefully.

measurements of the same species. Based on the normal distributed data set an antiproton-to- H^- ratio of

$$R_{\bar{p}H^-, \text{exp}} = 1.001\,089\,218\,872(64) \quad (8.4)$$

is extracted. As a consistency check also the ratios for identical particles can be derived with $R_{\text{id,exp}} - 1 = -3(79) \times 10^{-12}$, which is consistent with zero and independently verifies the experimental sequence.

The main systematic contribution arises from small asymmetries in the trap layout such as machining imperfections, misalignments or potential offsets in combination with a residual gradient $B_1 = 7.58(42) \text{ mT m}^{-1}$. To center \bar{p} and the H^- ion on the axial resonator slightly different ring voltages are required due to the different mass

$$v_z = \frac{1}{2\pi} \sqrt{\frac{2qC_2 V_r}{m_{\bar{p}}}} \approx \frac{1}{2\pi} \sqrt{\frac{2qC_2 (V_r + \Delta V)}{m_{H^-}}} \quad (8.5)$$

for a voltage adjustment of $\Delta V = 5 \text{ mV}$. In the case of small asymmetries, as shown in figure 8.3, the \bar{p} and the H^- ion will have slightly different axial positions. This, on the other hand, leads to different magnetic fields seen by the two species in the case of a non-vanishing magnetic field gradient as it is present in the setup. All asymmetries were determined by a careful characterization of the trapping potential offsets (a discussion in great detail can be found in the supplementary material of [95]) and the ratio was corrected by $-114(26) \text{ ppt}$.

Additionally, the necessary adjustment of the ring voltage ΔV leads to a slight detuning of the ideal tuning ratio TR , which causes $C_4 \neq 0$. The shift of the eigenfrequencies, see section 2.4, is accounted for with a correction of $-3(1)$ ppt.

The final result of the \bar{p} -to- H^- ratio after applying the corrections is

$$R_{\bar{p}H^-, \text{fin}} = 1.001\,089\,218\,755(64)(26) . \quad (8.6)$$

This result is equivalent to the antiproton-to-proton charge to mass ratio comparison of

$$R_{\bar{p}p, \text{fin}} - 1 = \frac{(q/m)_{\bar{p}}}{(q/m)_p} - 1 = 1(64)(26) \times 10^{-12} \quad (8.7)$$

in perfect agreement with CPT symmetry at a precision of 69 ppt. The first error is the statistical uncertainty while the second is due to systematics. The result can be interpreted in the framework of the standard model extension (SME) [103] which uses the figure of merit

$$r^{H^-} = (1 - R_{\bar{p}H^-, \text{fin}}) \frac{h\nu_{c,H^-}}{m_{H^-} c^2} \quad (8.8)$$

with the Plank constant h and the speed of light c . The presented result allows to set a new limit $r^{H^-} < 9 \times 10^{-27}$ which exceeds the previous limit [102] by a factor of four. The data can also be analyzed as a function of the sidereal time $t_{\oplus} = 86164.1\text{ s}$ to check the variation of fundamental constants as a function of the earth's rotation. Based on the data such a variation can be excluded with an upper limit of 0.72 ppb on the ratio $R_{\bar{p}H^-, \text{fin}}$.

Chapter 9

Outlook

This chapter briefly introduces the new measurement setup to implement the concept of sympathetic laser cooling which will significantly improve the overall cycle time. The new trap design was developed as part of this thesis and is explained in detail. In the second part of this chapter several additional future improvements to reach a higher precision are discussed.

9.1 Laser cooling

9.1.1 Motivation

The value of the g -factor presented in this thesis is limited by statistics and in order to improve the current value an optimization of the cycle time is essential. Reviewing the time budget, initially presented in figure 7.1, shows that the first column (Waiting and $\Gamma^{(k)}$ -measurement) typically requires 30 min. The particle preparation is performed in about 20 min and the spin state detection (Series 1 & 2) in 40 min.

The first block is mainly composed of the waiting period and the frequency measurement together with the Larmor excitation. A single spin-flip drive in the AT already heats the trap such that the waiting period becomes necessary to avoid nonlinear drifts during the frequency measurement and a reduction of this effect is challenging. The timing of the second and the third block are closely related to each other. The lower the temperature cut during the preparation the longer the preparation lasts until the cut requirement is met. On the other hand a lower temperature allows for a higher fidelity in the analysis trap, compare figure 9.1 A. A higher fidelity has the advantage that the axial series is potentially shorter and it requires less time until a significant change in the axial frequency related to a spin flip is observed. In addition, the data points with higher fidelity have a larger impact on the total result. Thus, any improvement on the cooling either by a faster preparation or a lower temperature immediately improves on the cycle time. The cycle time was one of the major improvements of the current work due to the implantation of a new superconducting cyclotron

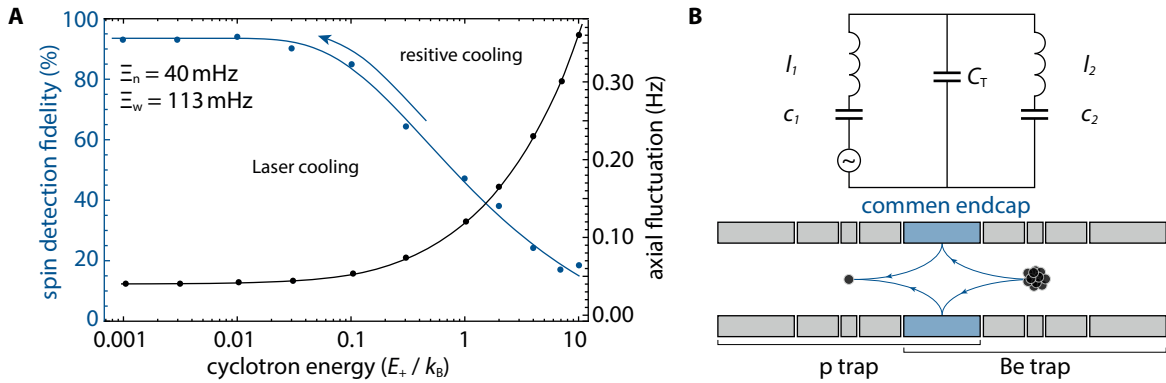


Fig. 9.1: (A) The figure shows the reachable spin-state detection fidelity as a function of the modified cyclotron energy. Note that the fidelity was rescaled to the range $[0\%,100\%]$. The technique of laser cooling should allow the preparation of energies below $0.1 K k_B$ on a minute scale. (B) Lumped circuit model of a proton and a Beryllium cloud connected by a common endcap. The particles are replaced by series tuned circuits. C_T is the parasitic trap capacitance of the common endcap.

resonator with smaller time constant and lower temperature. It should be noted that the time which is required for the spin state detection can immediately be halved by performing only one axial series. The second series serves no direct purpose for the g -factor resonance and is only a control mechanism to check whether the routine and the background noise behave as expected. This is, nonetheless, a very helpful feature but once the measurement routine runs well about 20 min per cycle can be easily gained by skipping the second series.

Summarizing the discussion above shows that the cycle time can possibly be reduced to 60 – 70 min by removing the second series and implementing an even improved cyclotron detector. However, a technique that allows a quasi-deterministic cooling of the proton within about 5 min to the low mK range, which allows spin-state detection in about 5 min, would be preferred. This would not only lead to a cycle time of 40 min, which already is a substantial improvement, but also to much higher fidelities and thus less required total data points for the same resonance. An attractive option to reach this goal is the technique of sympathetically cooling the proton by a cloud of laser-cooled beryllium ions. The mK beryllium cloud acts a thermal bath which the proton is coupled to. Ultimately, this should allow quasi-deterministic cooling of the proton.

9.1.2 Working principle

The original idea of coupling a laser-cooled cloud of ions to another particle by a *common endcap* was introduced early by Heinzen and Wineland [104]. The scheme is shown in figure 9.1 B in a lumped circuit representation. The proton and the Beryllium ions are both modelled as series tuned circuits connected by a common endcap represented in blue. The image charge of the laser-cooled Beryllium interacts with the common endcap and represents a thermal bath which is seen by the proton. This coupling leads to an energy exchange between both reservoirs. The advantage of this coupling scheme, compared to having both ion species in the same trap, is the spatial separation with

(mm)	PT	ST	CT/BT	AT
a	4.5	2.5	2.0	1.8
l_r	1.3099	0.6656	0.5046	0.4402
l_c	3.5300	1.9007	1.4937	1.3309
l_e	9.0000	3.7870	7.9480	4.4780
D_c	10.0	5.7	4.6	4.2
D_e	25.6	14.1	10.9	9.7
D_{c+e}	7.2	4.1	3.2	2.9
TR_{id}	0.8810	0.8807	0.8806	0.8804
C_2 (m ⁻²)	18 510	59 900	93 500	115 360
D_4 (m ⁻⁴)	1.28×10^9	1.34×10^{10}	3.27×10^{10}	4.98×10^{10}

Table 9.1: Typical trap parameters for ring electrode (r), correction electrode (c) and endcap (e) of precision trap (PT), source trap (ST), coupling trap(CT), Beryllium trap (BT) and analysis trap (AT). D is the effective electrode distance and a the radius of the trap.

no need to isolate the proton after the cooling.

To derive the energy exchange time the circuit model is assumed. The connection to the particle properties was already introduced in section 2.5. In [104] the exchange time was calculated

$$\tau_{\text{ex}} = \frac{\pi\omega_z D_1 D_2}{\sqrt{N_1 N_2}} C_T \frac{\sqrt{m_1 m_2}}{|q_1 q_2|} \quad (9.1)$$

with the assumption that both species are tuned to the same axial frequency ω_z . The effective electrode distance D_i is determined by the geometrical properties of the trap. By choosing a symmetric trap configuration with the same geometry for both species the effective electrode distance is $D_1 = D_2 = D_{\text{eff}}$. Furthermore, $N_1 = 1$ since only a single proton is used. To reach short exchange times the three relevant parameters to optimize are the number of beryllium ions, the self-capacitance of the common endcap and the effective electrode distance.

9.1.3 Coupling trap design

The trap design is based on the requirements in section 2.2, orthogonality and compensation. The main challenge in the trap design is the minimization of the effective electrode distance and of the self-capacitance to reach a short coupling time. All new trap parameters are summarized in table 9.1. The coupling trap (CT) contains the proton and the beryllium trap (BT) the beryllium cloud. A discussion of the other new traps will be presented in the following section.

A small radius, similar to the AT, is chosen for BT/CT due to the direct impact on the effective electrode distance, which decreases for smaller radii. For a fixed radius of $a = 2$ mm the effective electrode distance of the common endcap is evaluated with equation (2.21) to be 10.9 mm. To achieve a smaller electrode distance the common endcap is used together with the two neighboring elec-

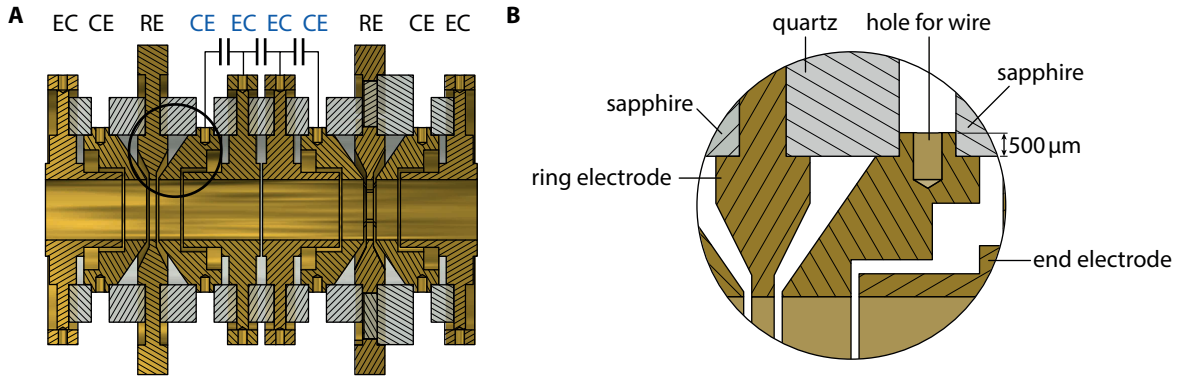


Fig. 9.2: (A) Schematic of the trap layout for BT and CT with endcaps (EC), correction electrodes (CE) and ring electrode (RE). The common endcap is a combination of four electrodes (CE+EC+EC+CE) that are connected capacitively. (B) Simplified zoomed view of the critical region that shows the major contribution to the total capacitance between ring electrode and correction electrode.

trodes to increase the signal pick-up. The electrodes are capacitively coupled and the total electrode distance decreases to 3.2 mm, a factor of three improvement.

The trap is designed in such a way that the capacitance of these three electrodes with respect to the rest of the setup becomes small, shown in the schematic 9.2 A. The original idea to have one common endcap was modified by having two separate endcaps because for a small radius-to-length ratio the electrode becomes a drift tube and stable transport is not possible. The two endcaps (EC) as well as the two correction electrodes (CE) are capacitively coupled to short them AC-wise and keep different DC potentials. The capacitance of CE+EC+EC+CE versus the rest of the setup can be simulated by a finite-element-method (FEM) simulation using the program *COMSOL Multiphysics*. The simulation confirms that the main contribution for the capacitance arises between the correction electrodes and the ring electrodes. The geometry optimization is based on the simple model of a parallel-plate capacitor

$$C = \epsilon_0 \epsilon_r \frac{A}{d} . \quad (9.2)$$

The capacitance can be minimized by reducing the area A seen between both electrodes (ring & correction electrode), by increasing the distance d or by reducing the amount of dielectric material with relative permittivity ϵ_r . To reduce the relative permittivity the sapphire (Al_2O_3) rings between ring and correction electrode were replaced with quartz (SiO_2) rings. This corresponds to a reduction of 2.5 from $\epsilon_r = 11.3$ for sapphire to $\epsilon_r = 4.43$ of quartz. Figure 9.2 B highlights the geometrical steps to minimize the capacitance of the common endcap assembly C_T . As a first step, the area seen by the ring electrode was minimized by reducing the overlap between ring electrode and quartz ring to 500 μm. A further reduction is not meaningful for the mechanical stability. The quartz ring was chosen with the thickness of 2.4 mm which increases the distance between ring and correction electrode. A further increase is constrained by the inner length of ring and correction electrode.

In total the simulated capacitance of the whole assembly is 8.8 pF with a sapphire ring for the

spacing between ring and correction electrode. If quartz is used instead the simulation yields 5.6 pF, an improvement by 25%. The capacitance was also obtained directly by connecting a tuned circuit and measuring the shift in the resonance frequency, which is a function of the connected capacitance. The result is 5.5(5) pF which is in good agreement with the simulation. Compared to other standard electrodes with typically 10 – 15 pF this design is a substantial improvement with impact for the exchange time by up to a factor of 2 faster cooling.

To improve the trap capacitance even further the electrodes itself could be produced with sapphire and only the inner trap layer is gold-plated. This would drastically reduce the capacitance but is difficult to manufacture as well as very expensive. Another alternative to improve the design discussed before, is the removal of material from the ring and correction electrode by milling holes along the trap axis. While technically possible by wire erosion the missing material can lead to a distortion such as elliptical electrodes.

Based on equation (9.1) and the designed trap the typical timescale for the cooling procedure can be derived [105]. For a cloud of about 100 Beryllium ions, the common endcap configuration of CE+EC+EC+CE, and an axial frequency of about 600 – 700 kHz coupling times below 1 min are feasible even if additional stray capacitances by wires with several pF are taken into account.

9.1.4 Experimental setup

The trap chamber setup [105] for the next-generation experiment to measure the proton g factor is shown in figure 9.3. The setup includes five traps, four of which were designed as part of this thesis. On the right hand side coupling trap (CT) and beryllium trap (BT) are located for the coupling of the proton to the beryllium cloud. Next to it is the new precision trap (PT) with a larger radius of 4.5 mm which allows a better compensated electric field. The AT is the same as in the previous run followed by the new source trap (ST) which is used to load protons.

To load protons the electron beam emitted from the field emission point (electron gun) is reflected by a negative voltage on e.g. the AT ring electrode. Subsequently, the electrons undergo multiple reflections and their magnetron radius increases in the presence of trap imperfections. Eventually, the electron beam hits the surface of the electron gun and protons can be loaded to the ST.

The Beryllium ions are produced with an ablation laser at 532 nm which sputters Beryllium of the Be target. The atoms are then ionized by electrons emitted from the electron gun. The cooling laser in the UV at 313 nm addresses the $2S_{1/2} \rightarrow 2P_{3/2}$ transition and directly cools the axial motion. The other modes are cooled indirectly due to Coulomb interaction and trap imperfections. A six-split electrode in the BT allows for the detection of fluorescence through the slits by dedicated silicon photomultipliers.

The cooling laser is guided through a fiber to the new second pinbase on the right hand side. A dedicated fiber mount allows the positioning with respect to all spatial coordinates as well as an angular adjustment. The mount also provides space for lenses and apertures. The lasers are guided through indium sealed sapphire windows into the cryogenically sealed trap chamber. The electrical pinbase on the left hand side is equipped with an additional sapphire window feedthrough. The

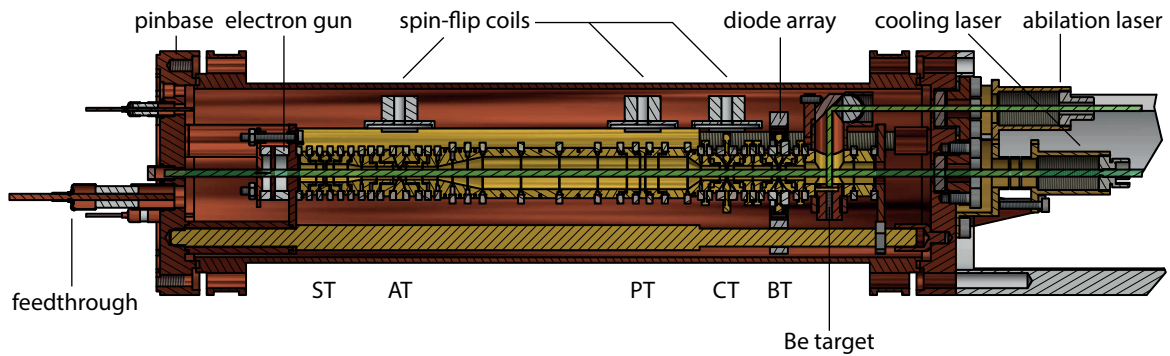


Fig. 9.3: New trap layout for laser cooling. The electrical pinbase on the left contains electrical feedthroughs for DC, detection and excitation lines. The five traps are mounted in the center of the trap chamber. The new optical pinbase on the right guides two lasers into the chamber through sapphire windows.

electron gun was modified such that the laser can pass through the whole chamber on axis and leaves through the window on the opposite side. A diode behind the window allows continuous tracking of the laser power and position, especially during cooldown.

All parts have been manufactured and assembled. First initial tests, such as beryllium loading, were successfully performed with the new setup. The implementation of laser cooled beryllium ions to cool a single isolated proton is the next big step towards an improved proton g -factor measurement.

9.2 Additional improvements towards < 300 ppt

This section covers additional considerations in order to reach a higher precision below the 300 ppt level. Partially these ideas are already implemented in the new setup for laser cooling.

- **Statistics**

The current measurement is limited by statistics which can be improved e.g. by performing only one axial series in the analysis trap. Moreover, the scheme of laser cooling, once successfully implemented, will speed up the cycle time drastically due to an improved particle preparation time and a higher spin-state detection fidelity.

- **Drive amplitude**

The g -factor resonance in the current run reaches a spin-flip probability of about 26% at its maximum which is well below saturation. An optimized Larmor excitation drive strength will allow a better signal-to-noise ratio without saturating the resonance. A higher S/N allows a higher precision with the same amount of data which speeds up the total measurement.

- **Phase method**

The phase method allows two different significant improvements for the g -factor experiment.

The first improvement is the up to 33% faster readout of the proton spin state in the analysis trap. This technique was demonstrated in this thesis in chapter 5. Once implemented in a robust manner, the phase method in the AT also enables a higher temperature cut which will improve the cycle time by another 15%.

The second even more important improvement is the direct measurement of the modified cyclotron frequency via the phase method. The current cyclotron frequency measurement is limited by the stability in the axial mode due the technique of sideband coupling. During the measurement of the modified cyclotron frequency any fluctuation in ν_z directly adds to the measurement of ν_+ . This can be avoided by measuring ν_+ by the *Pulse-and-Phase* (PnP) [65] or *Pulse-and-Amplify* (PnA) [87] method. Similar to the phase method in the analysis trap an initial phase is imprinted on the modified cyclotron mode. After a specific evolution time the phase information is transferred to the axial mode and read out. Performing such a phase readout for various evolution times allows the determination of ν_+ at the level of 10^{-11} [57].

Ultimately, the PnP or PnA technique becomes inevitable for a second reason. The current method of fitting dip spectra becomes more and more sensitive to undesired effects such as thermal broadening of the dip spectra or asymmetries on the resonator. The simplified dip-model which is used at the moment has reached a critical point where an optimization and a more accurate model is required. Such a model needs, however, additional input parameters such as the detection system temperature or the resonator center. Both of these information are not necessarily constant over time and continuous logging is time consuming and far less efficient than the implantation of the phase method.

- **PT optimization**

The major systematic correction at the moment is the effect of the image charge. Even though the error is comparably small, it is appealing to reduce this systematic shift. The image charge scales with the trap radius a^{-3} and a larger trap radius significantly lowers this shift. In addition, a larger trap is less sensitive to manufacturing imperfections leading to a better compensation. The compensation can be further improved by implementing a seven-pole trap recently used in the measurement of the proton mass [57]. Such a trap is used to compensate higher orders in the potential with $C_8 = C_{10} = 0$. As a consequence, the particle can be excited to much higher radii without shifting the eigenfrequencies, which is, for example, beneficial for the phase method.

- **Level and pressure stabilization**

Currently, the Helium pressure is stabilized due to its correlation to the particle's frequencies. During the last run measurements indicated that also the pressure in the nitrogen vessel has a relevant influence on the stability of the axial frequency. The behavior requires further characterization but due to the straight-forward implantation with an additional PID-controller it should be implemented to the system.

As a consequence of the horizontal mounting of the experimental setup in the magnet bore the

trap position is very sensitive on the weight that rests on the table with the cryostat. Especially, different levels in the nitrogen or helium tank have a direct impact on the position of the trap inside the magnet bore, which effectively causes a different magnetic field. Even though this long-term drift (2-3 days), while the cryo-liquids evaporate, was no limitation in the current setup it might be worthwhile to optimize it in the future.

In summary, the implementation of the phase method will allow for a direct detection of the modified cyclotron frequency and should have high priority. An order of magnitude improved measurement at the level of $< 10^{-11}$ seems feasible with this modification. However, such a measurement would be time consuming which is why the realization of laser cooling is very appealing to drastically improve the particle preparation time and reach much higher spin readout fidelities.

Chapter 10

Summary and conclusion

In this work the magnetic moment of the proton in units of the nuclear magneton was measured with a fractional precision of 3×10^{-10} which is a factor of 11 more precise than the previous measurement in 2014 [48].

$$\left(\frac{g}{2}\right)_{2017} = \frac{\mu_{\text{P}}}{\mu_{\text{N}}} = 2.792\,847\,344\,62(75) \quad (34)$$

This improvement became possible by implementing several significant upgrades on the setup. An optimized trap geometry allowed to get rid of the previous limitation caused by a residual magnetic field inhomogeneity in the precision trap. A new superconducting cyclotron resonator was developed to obtain a 3 times faster particle preparation which led to a 2 times faster experimental cycle time. The successful implantation of a self-shielding coil enabled a significant reduction of external magnetic field disturbances. New cryogenic ultra low-noise amplifiers were used to improve the axial detection systems. Finally, the drive amplitude was optimized over several months to eliminate line width broadening and the simultaneous measurement of ω_c and ω_L reduced systematic shifts.

The measurement is limited by statistics and by the stability of the axial frequency. A further improvement will become possible by a direct measurement of the modified cyclotron frequency which makes it independent of the axial stability. Furthermore, a new experimental approach is on-going and aims for the sympathetic cooling of a single isolated proton by a laser-cooled cloud of beryllium ions. If successfully implemented, this method will not only drastically speed up the particle preparation procedure but also increase the spin state readout to much higher fidelities.

The expertise made at the current setup in Mainz will as well be used by the CERN experiment for the antiproton and within the collaboration a continuous exchange of techniques takes place. E.g. the superconducting cyclotron resonators is used by both experiments at the moment as well as the self-shielding coil.

By comparing this result to the most recent antiproton g -factor measurement [49] new limits on possible CPT violating effects can be derived in the framework of the Standard Model Extension. At the current level of precision no CPT violation can be observed and an improved measurement of the antiproton magnetic moment is required. Together with the techniques achieved in Mainz such an improvement is in reach.

Besides the achievements in the g -factor regime the BASE collaboration at CERN measured the antiproton-to-proton charge-to-mass ratio with

$$\frac{(q/m)_{\bar{p}}}{(q/m)_p} - 1 = 1(69) \times 10^{-12} \quad (10.1)$$

which shows that CPT symmetry is conserved at the 69 ppt level and limited by statistics.. This is an improvement by a factor of four compared to the previous best value [102]. The leading systematic shift is due to small trap asymmetries together with a residual magnetic field gradient.

Penning traps have proven powerful tools to investigate fundamental properties at low-energies with very high precision. Technological advances continue to push back the boundaries and an end of this development is yet to come.

Bibliography

- [1] J. C. Maxwell, *A dynamical theory of the electromagnetic field*, Philos. Trans. Roy. Soc. London **155** (1865), 459 – 512.
- [2] E. Fermi, *Versuch einer Theorie der β -Strahlen*, Z. Phys. **88** (1934), no. 3, 161 – 177.
- [3] S. L. Glashow, *Partial-symmetries of weak interactions*, Nucl. Phys. **22** (1961), no. 4, 579 – 588.
- [4] S. Weinberg, *A model of leptons*, Phys. Rev. Lett. **19** (1967), no. 21, 1264 – 1266.
- [5] A. Salam, *Weak and electromagnetic interactions*, Conf. Proc. **C680519** (1968), 367 – 377.
- [6] F. Abe, et al., *Observation of top quark production in $\bar{p}p$ collisions with the collider detector at Fermilab*, Phys. Rev. Lett. **74** (1995), no. 14, 2626 – 2631.
- [7] S. Abachi, et al., *Search for high mass top quark production in $p\bar{p}$ collisions at $\sqrt{s} = 1.8$ TeV*, Phys. Rev. Lett. **74** (1995), no. 13, 2422 – 2426.
- [8] G. Aad, et al., *Observation of a new particle in the search for the Standard Model Higgs boson with the ATLAS detector at the LHC*, Phys. Lett. B **716** (2012), no. 1, 1 – 29.
- [9] S. Chatrchyan, et al., *Observation of a new boson at a mass of 125 GeV with the CMS experiment at the LHC*, Phys. Lett. B **716** (2012), no. 1, 30 – 61.
- [10] F. J. Hasert, et al., *Search for elastic muon-neutrino electron scattering*, Phys. Lett. B **46** (1973), no. 1, 121 – 124.
- [11] F. J. Hasert, et al., *Observation of neutrino-like interactions without muon or electron in the Gargamelle neutrino experiment*, Phys. Lett. B **46** (1973), no. 1, 138 – 140.
- [12] G. Arnison, et al., *Experimental observation of lepton pairs of invariant mass around 95 GeV/c² at the CERN SPS collider*, Phys. Lett. B **126** (1983), no. 5, 398 – 410.
- [13] Planck Collaboration, *Planck 2015 results*, A&A **594** (2016).
- [14] G. Lüders, *On the equivalence of invariance under time reversal and under particle-anti-particle conjugation for relativistic field theories*, Kong. Dan. Vid. Sel. Mat. Fys. Med. **28** (1954), 1 – 17.
- [15] W. Pauli, *Exclusion principle, Lorentz group and reflection of space-time and charge*, Niels Bohr and the Development of Physics (1955), 30 – 51.

- [16] A. D. Sakharov, *Violation of CP invariance, C asymmetry, and baryon asymmetry of the universe*, JETP Lett. **5** (1967), 24 – 27.
- [17] L. Canetti, M. Drewes, and M. Shaposhnikov, *Matter and antimatter in the universe*, New J. Phys. **14** (2012), no. 9, 095012.
- [18] J. Beringer, et al., *Review of particle physics*, Phys. Rev. D **86** (2012), no. 1, 010001.
- [19] O. Bertolami, D. Colladay, V. A. Kostelecký, and R. Potting, *CPT violation and baryogenesis*, Phys. Lett. B **395** (1997), no. 3, 178 – 183.
- [20] V. A. Kostelecký and N. Russell, *Data tables for Lorentz and CPT violation*, Rev. Mod. Phys. **83** (2011), no. 1, 11 – 31.
- [21] Y. Ding and V. A. Kostelecký, *Lorentz-violating spinor electrodynamics and Penning traps*, Phys. Rev. D **94** (2016), no. 5, 056008.
- [22] B. N. Taylor, W. H. Parker, and D. N. Langenberg, *Determination of e/h , using macroscopic quantum phase coherence in superconductors: Implications for quantum electrodynamics and the fundamental physical constants*, Rev. Mod. Phys. **41** (1969), no. 3, 375 – 496.
- [23] E. R. Cohen and B. N. Taylor, *The 1973 least-squares adjustment of the fundamental constants*, J. Phys. Chem. Ref. Data **2** (1973), no. 4, 663 – 734.
- [24] M. Ahmadi, et al., *Observation of the 1S-2S transition in trapped antihydrogen*, Nature **541** (2016), no. 7638, 506 – 510.
- [25] B. Schwingerheuer, et al., *CPT tests in the neutral kaon system*, Phys. Rev. Lett. **74** (1995), no. 22, 4376 – 4379.
- [26] R. S. Van Dyck Jr., P. B. Schwinberg, and H. G. Dehmelt, *New high-precision comparison of electron and positron g -factors*, Phys. Rev. Lett. **59** (1987), no. 1, 26 – 29.
- [27] R. K. Mittleman, I. I. Ioannou, H. G. Dehmelt, and N. Russell, *Bound on CPT and Lorentz symmetry with a trapped electron*, Phys. Rev. Lett. **83** (1999), no. 11, 2116 – 2119.
- [28] G. W. Bennett et al., *Final report of the E821 muon anomalous magnetic moment measurement at BNL*, Phys. Rev. D **73** (2006), no. 7, 072003.
- [29] C. Smorra, et al., *BASE - The Baryon Antibaryon Symmetry Experiment*, Eur. Phys. J. Spec. Top. **224** (2015), no. 16, 3055 – 3108.
- [30] R. Frisch and O. Stern, *Über die magnetische Ablenkung von Wasserstoffmolekülen und das magnetische Moment des Protons. I*, Z. Phys. **85** (1933), no. 1, 4 – 16.
- [31] P. A. M. Dirac, *The quantum theory of the electron*, Proceedings of the Royal Society of London A: Mathematical, Physical and Engineering Sciences **117** (1928), no. 778, 610 – 624.

- [32] I. I. Rabi, J. M. B. Kellogg, and J. R. Zacharias, *The magnetic moment of the proton*, Phys. Rev. **46** (1934), no. 3, 157 – 163.
- [33] I. I. Rabi, J. R. Zacharias, S. Millman, and P. Kusch, *A new method of measuring nuclear magnetic moment*, Phys. Rev. **53** (1938), no. 4, 318 – 318.
- [34] J. M. B. Kellogg, I. I. Rabi, N. F. Ramsey, and J. R. Zacharias, *The magnetic moments of the proton and the deuteron. The radiofrequency spectrum of H₂ in various magnetic fields*, Phys. Rev. **56** (1939), no. 8, 728 – 743.
- [35] F. Bloch, *Nuclear induction*, Phys. Rev. **70** (1946), no. 7 - 8, 460 – 474.
- [36] F. Bloch and C. D. Jeffries, *A direct determination of the magnetic moment of the proton in nuclear magnetons*, Phys. Rev. **80** (1950), no. 2, 305 – 306.
- [37] P. F. Winkler, D. Kleppner, T. Myint, and F. G. Walther, *Magnetic moment of the proton in Bohr magnetons*, Phys. Rev. A **5** (1972), no. 1, 83 – 114.
- [38] J. D. Fox, et al., *Measurement of the magnetic moment of the antiproton*, Phys. Rev. Lett. **29** (1972), no. 3, 193 – 195.
- [39] B. L. Roberts, et al., *New value for the magnetic moment of the antiproton*, Phys. Rev. Lett. **33** (1974), no. 19, 1181 – 1182.
- [40] E. Hu, et al., *Mass and magnetic moment of the antiproton by the exotic atom method*, Nucl. Phys. A **254** (1975), no. 2, 403 – 412.
- [41] A. Kreissl, et al., *Remeasurement of the magnetic moment of the antiproton*, Z. Phys. C Particles and Fields **37** (1988), no. 4, 557 – 561.
- [42] T. Pask, et al., *Antiproton magnetic moment determined from the HFS of $\bar{p}\text{He}^+$* , Phys. Lett. B **678** (2009), no. 1, 55 – 59.
- [43] J. DiSciaccia, et al., *One-particle measurement of the antiproton magnetic moment*, Phys. Rev. Lett. **110** (2013), no. 13, 130801.
- [44] J. DiSciaccia and G. Gabrielse, *Direct measurement of the proton magnetic moment*, Phys. Rev. Lett. **108** (2012), no. 15, 153001.
- [45] C. C. Rodegheri, et al., *An experiment for the direct determination of the g-factor of a single proton in a Penning trap*, New J. Phys. **14** (2012), no. 6, 063011.
- [46] H. Nagahama, et al., *Sixfold improved single particle measurement of the magnetic moment of the antiproton*, Nat. Commun. **8** (2017), 14084.
- [47] H. Häffner, et al., *Double Penning trap technique for precise g factor determinations in highly charged ions*, Eur. Phys. J. D - Atomic, Molecular, Optical and Plasma Physics **22** (2003), no. 2, 163 – 182.

- [48] A. Mooser, et al., *Direct high-precision measurement of the magnetic moment of the proton*, Nature **509** (2014), no. 7502, 596 – 599.
- [49] C. Smorra, et al., *A parts-per-billion measurement of the antiproton magnetic moment*, Nature **550** (2017), no. 7676, 371 – 374.
- [50] G. Schneider, et al., *Double-trap measurement of the proton magnetic moment at 0.3 parts per billion precision*, Science **358** (2017), no. 6366, 1081 – 1084.
- [51] L. S. Brown and G. Gabrielse, *Geonium theory: Physics of a single electron or ion in a Penning trap*, Rev. Mod. Phys. **58** (1986), no. 1, 233 – 311.
- [52] L. S. Brown and G. Gabrielse, *Precision spectroscopy of a charged particle in an imperfect Penning trap*, Phys. Rev. A **25** (1982), no. 4, 2423 – 2425.
- [53] G. Gabrielse, L. Haarsma, and S. L. Rolston, *Open-endcap Penning traps for high precision experiments*, Int. J. Mass Spectrom. Ion Processes **88** (1989), no. 2 - 3, 319 – 332.
- [54] J. D. Jackson, *Classical electrodynamics*, 3. ed., Wiley, New York, 1999.
- [55] Z. Andelkovic, et al., *Laser cooling of externally produced Mg ions in a Penning trap for sympathetic cooling of highly charged ions*, Phys. Rev. A **87** (2013), no. 3, 033423.
- [56] S. Sturm, et al., *High-precision measurement of the atomic mass of the electron*, Nature **506** (2014), no. 7489, 467 – 470.
- [57] F. Heiße, et al., *High-precision measurement of the proton's atomic mass*, Phys. Rev. Lett. **119** (2017), no. 3, 033001.
- [58] S. Ulmer, *First observation of spin flips with a single proton stored in a cryogenic Penning trap*, Ph.D. thesis, Universität Heidelberg, Germany, 2011.
- [59] G. Duffing, *Erzwungene Schwingungen bei veränderlicher Eigenfrequenz und ihre technische Bedeutung*, no. 41 - 42, R, Vieweg & Sohn, 1918.
- [60] J. Ketter, T. Eronen, M. Höcker, S. Streubel, and K. Blaum, *First-order perturbative calculation of the frequency-shifts caused by static cylindrically-symmetric electric and magnetic imperfections of a Penning trap*, Int. J. Mass Spectrom. **358** (2014), 1 – 16.
- [61] D. J. Wineland and H. G. Dehmelt, *Principles of the stored ion calorimeter*, J. Appl. Phys. **46** (1975), no. 2, 919 – 930.
- [62] X. Feng, M. Charlton, M. Holzscheiter, R. A. Lewis, and Y. Yamazaki, *Tank circuit model applied to particles in a Penning trap*, J. Appl. Phys. **79** (1996), no. 1, 8 – 13.
- [63] H. Nyquist, *Thermal agitation of electric charge in conductors*, Phys. Rev. **32** (1928), no. 1, 110 – 113.

- [64] H. Nagahama, et al., *Highly sensitive superconducting circuits at 700 kHz with tunable quality factors for image-current detection of single trapped antiprotons*, Rev. Sci. Instrum. **87** (2016), no. 11, 113305.
- [65] E. A. Cornell, R. M. Weisskoff, K. R. Boyce, and D. E. Pritchard, *Mode coupling in a Penning trap: π pulses and a classical avoided crossing*, Phys. Rev. A **41** (1990), no. 1, 312 – 315.
- [66] H. G. Dehmelt, N. Warren, and S. Jon, *Self-excited mono-ion oscillator*, Proc. Natl. Acad. Sci. **83** (1986), no. 16, 5761 – 5763.
- [67] B. D’Urso, B. Odom, and G. Gabrielse, *Feedback cooling of a one-electron oscillator*, Phys. Rev. Lett. **90** (2003), no. 4, 043001.
- [68] B. D’Urso, *Cooling and self-excitation of a one-electron oscillator*, Ph.D. thesis, Harvard University, 2003.
- [69] H. G. Dehmelt and P. Ekstrom, *Proposed $g - 2/\delta v_z$ experiment on single stored electron or positron*, Bull. Am. Phys. Soc **18** (1973), no. 4, 727 – 728.
- [70] W. Gerlach and O. Stern, *Der experimentelle Nachweis der Richtungsquantelung im Magnetfeld*, Z. Phys. **9** (1922), no. 1, 349 – 352.
- [71] H. Häffner, et al., *High-accuracy measurement of the magnetic moment anomaly of the electron bound in hydrogenlike carbon*, Phys. Rev. Lett. **85** (2000), no. 25, 5308 – 5311.
- [72] J. Verdú, et al., *The magnetic moment anomaly of the electron bound in hydrogen-like oxygen $^{16}\text{O}^{7+}$* , J. Phys. B: At. Mol. Opt. Phys. **36** (2003), no. 3, 655 – 663.
- [73] S. Ulmer, et al., *Observation of spin flips with a single trapped proton*, Phys. Rev. Lett. **106** (2011), no. 25, 253001.
- [74] A. Mooser, et al., *Resolution of single spin flips of a single proton*, Phys. Rev. Lett. **110** (2013), no. 14, 140405.
- [75] A. Mooser, et al., *Demonstration of the double Penning trap technique with a single proton*, Phys. Lett. B **723** (2013), 78 – 81.
- [76] A. Mooser, *Der g-Faktor des Protons*, Ph.D. thesis, Universität Mainz, Germany, 2013.
- [77] C. Smorra, et al., *A reservoir trap for antiprotons*, Int. J. Mass Spectrom. **389** (2015), 10 – 13.
- [78] G. Schneider, *Development of a Penning trap system for the high precision measurement of the antiproton’s magnetic moment*, Master’s thesis, Johannes Gutenberg-Universität Mainz, 2014.
- [79] L. S. Brown, *Geonium lineshape*, Ann. Phys. **159** (1985), no. 1, 62 – 98.
- [80] S. Ulmer, et al., *A cryogenic detection system at 28.9MHz for the non-destructive observation of a single proton at low particle energy*, Nucl. Instrum. Methods Phys. Res., Sect. A **705** (2013), 55 – 60.

- [81] H. Alfvén, *Cosmical electrodynamics*, Oxford, 1950.
- [82] G. Gabrielse and J. Tan, *Self-shielding superconducting solenoid systems*, J. Appl. Phys. **63** (1988), no. 10, 5143 – 5148.
- [83] S. Stahl, et al., *Phase-sensitive measurement of trapped particle motions*, J. Phys. B: At., Mol. Opt. Phys. **38** (2005), no. 3, 297.
- [84] F. T. Köhler, *Bound-electron g-factor measurements for the determination of the electron mass and isotope shifts in highly charged ions*, Ph.D. thesis, Universität Heidelberg, Germany, 2015.
- [85] S. Sturm, *The g-factor of the electron bound in $^{28}\text{Si}^{13+}$* , Ph.D. thesis, Universität Mainz, Germany, 2011.
- [86] E. A. Cornell, et al., *Single-ion cyclotron resonance measurement of $M(\text{CO}^+)/M(\text{N}_2^+)$* , Phys. Rev. Lett. **63** (1989), no. 16, 1674 – 1677.
- [87] S. Sturm, A. Wagner, B. Schabinger, and K. Blaum, *Phase-sensitive cyclotron frequency measurements at ultralow energies*, Phys. Rev. Lett. **107** (2011), no. 14, 143003.
- [88] C. Smorra, et al., *Observation of individual spin quantum transitions of a single antiproton*, Phys. Lett. B **769** (2017), 1 – 6.
- [89] G. F. A. de L'Hospital, *Analyse des infiniment petits, pour l'intelligence des lignes courbes*, A Paris, de l'Imprimerie royale. M.DC.XCVI, 1696.
- [90] P. J. Mohr, D. B. Newell, and B. N. Taylor, *CODATA recommended values of the fundamental physical constants: 2014*, Rev. Mod. Phys. **88** (2016), no. 3, 035009.
- [91] N. Metropolis and S. Ulam, *The Monte Carlo method*, J. Am. Stat. Assoc. **44** (1949), no. 247, 335 – 341.
- [92] V. Blobel and E. Lohrmann, *Statistische und numerische Methoden der Datenanalyse*, 1 ed., Vieweg+Teubner Verlag, 1998.
- [93] H. Häffner, *Präzisionsmessung des magnetischen Moments des Elektrons in wasserstoffähnlichem Kohlenstoff*, Ph.D. thesis, Universität Mainz, Germany, 2000.
- [94] NIST, *Material Properties of OFHC Copper*, http://cryogenics.nist.gov/MPropsMAY/OFHC%20Copper/OFHC_Copper_rev1.htm, October 2017.
- [95] S. Ulmer, et al., *High-precision comparison of the antiproton-to-proton charge-to-mass ratio*, Nature **524** (2015), no. 7564, 196 – 199.
- [96] M. Hori and J. Walz, *Physics at CERN's antiproton decelerator*, Prog. Part. Nucl. Phys. **72** (2013), 206 – 253.

- [97] S. Sellner, et al., *Improved limit on the directly measured antiproton lifetime*, New J. Phys. **19** (2017), no. 8, 083023.
- [98] J. K. Thompson, S. Rainville, and D. E. Pritchard, *Cyclotron frequency shifts arising from polarization forces*, Nature **430** (2004), no. 6995, 58 – 61.
- [99] C. G. Parthey, et al., *Improved measurement of the hydrogen 1S-2S transition frequency*, Phys. Rev. Lett. **107** (2011), no. 20, 203001.
- [100] A. K. Bhatia and R. J. Drachman, *Polarizability of helium and the negative hydrogen ion*, J. Phys. B: At., Mol. Opt. Phys. **27** (1994), no. 7, 1299.
- [101] R. S. Van Dyck Jr., D. L. Farnham, S. L. Zafonte, and P. B. Schwinberg, *High precision Penning trap mass spectroscopy and a new measurement of the proton's atomic mass*, AIP Conference Proceedings **457** (1999), no. 1, 101 – 110.
- [102] G. Gabrielse, et al., *Precision mass spectroscopy of the antiproton and proton using simultaneously trapped particles*, Phys. Rev. Lett. **82** (1999), no. 16, 3198 – 3201.
- [103] R. Bluhm, V. A. Kostelecký, and N. Russell, *CPT and Lorentz tests in Penning traps*, Phys. Rev. D **57** (1998), no. 7, 3932 – 3943.
- [104] D. J. Heinzen and D. J. Wineland, *Quantum-limited cooling and detection of radio-frequency oscillations by laser-cooled ions*, Phys. Rev. A **42** (1990), no. 5, 2977 – 2994.
- [105] M. Bohman, et al., *Sympathetic cooling of protons and antiprotons with a common endcap Penning trap*, accepted 18 October 2017.

Appendix A: Experimental values

Note, that some of the presented values, such as the frequencies or voltages, are not constant over time and the values stated here are a “snapshot”.

A.1 Analysis trap

A.1.1 Overview

- $V_r = -1.0335 \text{ V}$ — ring voltage for 0 K
- $TR_{id} = 0.489881 \cdot V_r + 1.34041$ — ideal tuning ratio as function of ring voltage
- $p_{SF,AT} = 0.366(16)$ — spin-flip probability during g -factor measurement
- $\Xi_n = 40.0(5.0)$ — white noise contribution during g -factor measurement
- $\Xi_w = 124.0(5.3)$ — walk contribution during g -factor measurement
- $B_{0,AT} = 1.17952(10) \text{ T}$ — absolute magnetic field
- $B_{2,AT} = 298\,000(5000) \text{ T m}^{-2}$ — strength of magnetic bottle
- $\Delta v_{z,SF} = 172(3) \text{ mHz}$ — axial frequency change due to induced spin flip
- $\Delta v_{z,+} = 62 \text{ mHz}$ — axial frequency change due to cyclotron quantum jump
- $\Delta v_{z,-} = 52 \text{ } \mu\text{Hz}$ — axial frequency change due to magnetron quantum jump
- $\Delta v_z(T) = 71.4 \text{ Hz K}^{-1} \Delta T$ — axial frequency change per change of 1 K
- $\Delta v_z(TR) = -15.4(7) \text{ Hz mUnit}^{-1}$ — axial frequency change per milliunit of TR
- $\Delta v_z(V_r) = 397\,000 \text{ Hz } \Delta V_r^{-1}$ — axial frequency change per ring voltage
- $C_{2,AT} = 109\,090(50) \text{ m}^{-2}$ — measured trap parameter
- $D_{4,AT} = 4.98 \times 10^{10} \text{ m}^{-4}$ — theoretical trap parameter

A.1.2 Axial resonator

- $D_z = 10 \text{ mm}$ — effective electrode distance axial
- $Q_z = 21\,700$ — quality factor axial resonator
- $L_z = 1.91 \text{ mH}$ — inductance of axial resonator
- $S/N = 29.6(4) \text{ dB}$ — signal-to-noise ratio

- $\kappa_{\text{PT}} = 0.2$ — coupling factor
- $T_z = 18.1(6)$ K — temperature of the axial detection system

A.2 Precision trap

A.2.1 Overview

- $V_r = -2.65682$ V — ring voltage
- $TR_{\text{id}} = 0.885262$ — ideal tuning ratio
- $B_{0,\text{PT}} = 1.900(1)$ T — absolute magnetic field
- $B_{1,\text{PT}} = 66.8(1)$ mT m⁻¹ — linear magnetic field
- $B_{2,\text{PT}} = 0.1(1)$ T m⁻² — quadratic magnetic field
- $\Delta\nu_z = 21.0(2)$ Hz mUnit⁻¹ — axial frequency change per milliunit of TR
- $C_{2,\text{AT}} = 31127(20)$ m⁻² — measured trap parameter
- $D_{4,\text{PT}} = 3.50 \times 10^9$ m⁻⁴ — theoretical trap parameter
- $V_0 = -2.65681$ V — ring voltage
- $D_4 T_z = 4.75(2.82) \cdot 10^{10}$ m⁻⁴ K
- $B_2 T_z = 1.306(38)$ T m⁻² K
- $a = 3.5$ mm — ideal trap radius
- $r_0 = 3.488(30)$ mm — estimated trap radius at 4 K

A.2.2 Axial resonator

- $D_z = 21.5$ mm — effective electrode distance
- $Q_z = 6400$ — quality factor
- $L_z = 2.65$ mH — inductance
- $S/N = 19.6(5)$ dB — signal-to-noise ratio
- $\kappa_{\text{PT}} = 0.1$ — coupling factor
- $T_z = 13.6(8.1)$ K — temperature

A.2.3 Cyclotron resonator

- $D_+ = 15.6$ mm — effective electrode distance
- $Q_+ = 1400$ — quality factor
- $L_+ = 1.7$ μ H — inductance
- $S/N = 14.7(9)$ dB — signal-to-noise ratio
- $\kappa_+ = 0.6$ — coupling factor
- $T_+ = 9.6(5)$ K — temperature

A.3 g -factor related measurement parameters

A.3.1 Precision trap

- $t_{\text{avg},+} = 120$ s — double dip averaging time
- $t_{\text{avg},z} = 60$ s — single dip averaging time
- $E_{\text{exc,SF}} = -28$ dBm — Larmor excitation strength
- $\Delta\nu_{\text{FFT}} = 50$ Hz — FFT span
- $\nu_c = 28\,968\,064$ Hz — free cyclotron frequency during g -factor routine
- $\nu_+ = 28\,961\,132$ Hz — modified cyclotron frequency during g -factor routine
- $\nu_z = 633\,664$ Hz — axial frequency during g -factor routine
- $\nu_- = 6\,933$ Hz — magnetron frequency during g -factor routine
- $\nu_{\text{rabi}} = 7.83$ Hz — Rabi frequency during g -factor routine for cyclotron sideband

A.3.2 Analysis trap

- $t_{\text{avg},z} = 60$ s — single dip averaging time
- $E_{\text{exc,SF}} = -5$ dBm — Larmor excitation strength
- $t_{\text{exc,SF}} = 20$ s — Larmor excitation length
- $\Delta\nu_{\text{FFT}} = 100$ Hz — FFT span
- $A_{\text{TH}} = 0.1$ mHz — threshold parameter ($A_{\text{TH}} \cdot T_+ + B_{\text{TH}}$)
- $B_{\text{TH}} = 0.19$ mHz — threshold parameter ($A_{\text{TH}} \cdot T_+ + B_{\text{TH}}$)

A.3.3 Miscellaneous

- $p_{\text{stab}} = 1030$ mbar — pressure stabilization setpoint
- $T_{\text{stab}} = 29^\circ\text{C}$ — temperature stabilization setpoint
- FFT settings: Time record increment 12.5%, RMS averaging, Type linear

Appendix B: Connection diagram

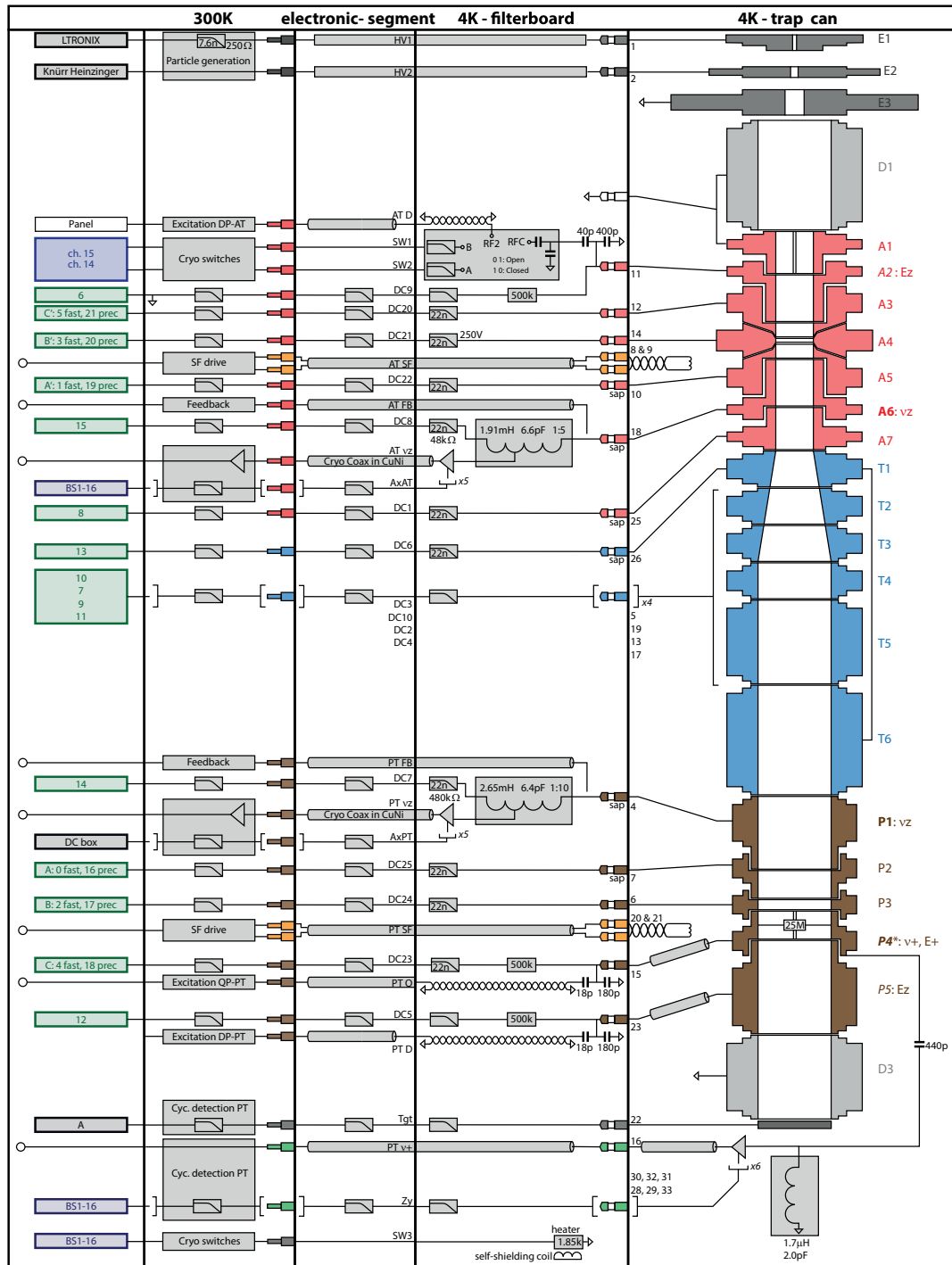


Fig. B.1: Schematic connection diagram of the whole experiment